A Systematic Integration of Empirical and Computational Studies to Biophysically Describe Recombinant Nicotinate Mononucleotide Adenylyltransferase (NaMNAT) From *Klebsiella pneumoniae* and *Enterococcus faecium*

by

Olamide Adetomi Jeje

(2219632)

A dissertation

Submitted in fulfilment of the requirements for the degree of

Master of Science

in

Molecular and Cell Biology

in the Faculty of Science, University of the Witwatersrand, Johannesburg, South Africa

Supervisor: Dr Ikechukwu A. Achilonu

August 2021.

DECLARATION

I declare that this dissertation is my own, unaided work. It is being submitted for the Degree of Master of Science at the University of the Witwatersrand, Johannesburg. It has not been submitted before for any degree or examination at any other University.

Olamide A. Jeje

___12th___day of ___August___2021.

ABSTRACT

Background: The continuous threat of drug-resistant *Klebsiella pneumoniae* and *Enterococcus faecium* justifies identifying novel targets and developing effective antibacterial agents against these multi-drug-resistant pathogens. Given the vital role of NAD^+ in bacteria survival, nicotinate mononucleotide adenylyltransferase (NaMNAT) represents an attractive target for the design of novel antibiotics. NaMNAT activity is conserved in almost all living things, and the respective enzymes exhibit various structural and catalytic properties that reflect their species and specificity. They employ divalent cations for co-substrate binding and catalysis as metal-activated enzymes and have shown preferences for different divalent cations. In this study, NaMNAT from *K. pneumoniae (Kp*NaMNAT*)* and *E. faecium* (*Ef*NaMNAT) were biophysically described and compared using a combination of experimental and computational approaches. **Methods**: Overexpression of the enzymes was achieved with pET vector in *Escherichia coli* and was purified using a one-step nickel ion-immobilised metal affinity chromatography (IMAC). The activity of the enzymes was assayed via a dual enzyme catalysed reaction involving alcohol dehydrogenase at varying pH in the absence and presence of divalent cations. Far-UV circular dichroism, extrinsic fluorescence spectroscopy, and analytical SE-HPLC were employed to assay the secondary content, tertiary, and quaternary structures. The stability of the enzymes was analysed via SYPRO Orange-based thermal shift assay in the absence and presence of varying divalent cations and ATP. Homology modelling, molecular docking, and molecular dynamic simulation were employed to complement the empirical studies. **Results:** The pET vector expression system and IMAC purification were efficient at overexpressing soluble enzymes and purifying the enzymes to homogeneity. Activity studies revealed both proteins to exhibit different catalytic properties. *Kp*NaMNAT utilised NMN as substrate while demonstrating broad pH optimum of 6.5–9.5 and preference for Mg^{2+}. Whereas *Ef*NaMNAT showed minimal activity with NMN and a preference for Zn^{2+}. Structural analysis showed both enzymes to be predominately α-helical, with *Kp*NaMNAT existing mainly as a monomer while *Ef*NaMNAT exists as a homodimer. *Kp*NaMNAT exhibits a more hydrophobic binding compare to *Ef*NaMNAT; however, the binding of ligands to this pocket did not induce conformational change in *Kp*NaMNAT compared to *Ef*NaMNAT. Thermal stability assay confirmed *Ef*NaMNAT to be more stable than *Kp*NaMNAT, and this stability is enhanced upon ligand binding. However, ligand binding did not impact the stability of *Kp*NaMNAT; nonetheless, Zn^{2+} and Cu^{2+} alter the conformation of *Kp*NaMNAT. Induced-fit ligand docking indicated that ATP, NMN, and NAD^+ bind at the same site on *Kp*NaMNAT, and a 100 ns simulation revealed the ligands to be stabilised by H-bonds, water-bridges, electrostatic, and van der Waals interactions. The binding of the ligands does not severely perturb the global structure of *Kp*NaMNAT. Overall, ATP is the most dynamic of all the three ligands, and Mg^{2+} influences its dynamism. **Conclusion**: The differences demonstrated in the structure and function of these two enzymes provide insights into the distinctive features of NaMNAT from Gram-negative *K. pneumoniae* and Gram-positive *E. faecium* and a basis for structure-function comparison between the two classes of bacteria. This study is beneficial for the novel application of these enzymes and as a molecular basis for further evaluation of the enzymes for the rational design of inhibitors with therapeutic potential.

To God Almighty, the giver of life, health, strength, inspiration, and wisdom.

ACKNOWLEDGEMENTS

Throughout this research, I have received a great deal of support and assistance.

Firstly, I express gratitude to my supervisor, Dr Ikechuckwu Achilonu, for his extensive personal and professional guidance throughout this research. His invaluable expertise and constructive criticism were a massive motivation and catalyst to successful completion of this dissertation. I can only say a big thank you for your patience, understanding, encouragement, availability and finally, for believing in me.

My unreserved acknowledgement to everyone in the Protein Structure-Function Research Unit (PSFRU), especially Professor Yasien Sayed, the unit head and director, Professor H.W. Dirr, the founder of PSFRU, and Dr Sylvia Fanucchi, for providing the platform and for making the unit a conducive place for learning and research. A special thank you to Blessing Oyiogu and Tasvi Daya for their advice at the initial stage of my research. Also, Dr Monare, your professional guidance during my quest to interpret some of my results was amazingly helpful. Worthy of mention is Dr Roland Worth for his time and assistance in reviewing my dissertation. MRC research grant and Wits Hardship Fund, thank you for the financial support.

Finally, my sincere appreciation to my family, your love and support is inspiring. A special thank you to my wonderful parents for your prayers and words of encouragement. I could not have completed this dissertation without the support of the most amazing man in my life, my husband, who supported my career goals and provided both financial and emotional support to pursue these goals. Thank you for believing in me. To my amazing children, Folayemi and Motolani, thank you for your patience and understanding. You provide unending inspiration.
Most importantly, my eternal gratitude to God almighty for making the journey towards a Master's degree a success.

TABLE OF CONTENTS

LIST OF FIGURES

LIST OF TABLES

LIST OF ABBREVIATIONS

ADH	Alcohol dehydrogenase
ANS	8-anilino-1-naphthalenesulfonic acid
ATP	Adenosine triphosphate
CID	Compound ID
EC	Enzyme class
*Ec*NMNAT	*Escherichia coli* NMNAT
*Ef*NaMNAT	*Enterococcus faecium* NaMNAT
HAIs	Health-care-associated infections
hNMNAT	Human NMNAT
IFD	Induced-fit docking
IMAC	Immobilized Metal Affinity Chromatography
IPTG	Isopropyl β-D-1-thiogalactopyranoside
kDa	Kilodalton
*Kp*NaMNAT	*Klebsiella pneumoniae NaMNAT*
mant-ATP	2′/3′-O-(N-Methyl-anthraniloyl)-adenosine-5′-triphosphate
MDR	Multi-drug resistant
NaAD	Nicotinate adenine dinucleotide
NAD^+	Nicotinamide adenine dinucleotide
NadD	Nicotinate Mononucleotide Adenylyltransferase gene
NADS	NAD synthetase
NadE	NAD synthetase gene
NaMN	Nicotinate mononucleotide
NaMNAT	Nicotinate mononucleotide adenylyltransferase
NamPRT	Nicotinamide phosphoribosyltransferase
NAPRTase	Nicotinate phosphoribosyltransferase
NMN	Nicotinamide mononucleotide
NMNAT	Nicotinamide mononucleotide adenylyltransferase
NPT	Number of molecules/atoms in assembly Pressure and Temperature
NRK	Nicotinamide riboside kinase
NVE:	Number of molecules/atoms in assembly Volume and Energy
NVT	Number of molecules/atoms in assembly Volume and Temperature

OD	Optical density
OPLS	Optimized Potentials for Liquid Simulations
PDB	Protein Data Bank
PRPP	5-phosphoribosyl-1-pyrophosphate
QAPRTase	Quinolinic acid phosphoribosyltransferase
Rg	Radius of gyration
RMSD	Root means square deviation
RMSF	Root means square fluctuation
SASA	Solvent accessible surface area
SDS-PAGE	Sodium dodecyl sulphate polyacrylamide gel electrophoresis
SE- HPLC	Size exclusion high-pressure liquid chromatography
T_m	Melting temperature
$\Delta\Phi$	Quantum yield

The IUPAC-IUBMB one and three letters code for amino acids are used.

Chapter 1

INTRODUCTION

1.1 Problem Statement

The spike in the rate of nosocomial infection caused by multi-drug resistant (MDR) bacteria is strikingly alarming and remains a major global concern to health care systems. Nosocomial infections, also termed health-care-associated infections (HAIs), are contracted during hospitalisation, and it includes new infections diagnosed within 48 h after hospitalisation, 72 h of discharge, and or 30 days post-operation (Dave *et al.*, 2005; Rothe *et al.*, 2013; Nair *et al.*, 2018). These infections are opportunistic, accounting for about 50% of all treated cases of infections in the hospitals. The impact of HAIs ranges from minor to terminal in patients admitted to intensive care units (ICU), premature neonates (Coffin and Zaoutis, 2011), patients with history of chronic diseases, and adults above the age of 70 years due to their immunodeficiencies (Rice, 2008; Santajit and Indrawattana, 2016). While significant progress has been made preventing transmission, the burden of this infection on patients of all age groups and public healthcare systems on any given day is higher in developing countries compared to Europe and USA (Allegranzi *et al.*, 2011; Lowman, 2016). Notably, between 5 to 10% of patients admitted into the ICU in developed countries acquire a hospital-associated infection, while the rate is over 21% in developing countries such as South Africa (Dave *et al.*, 2005; Edwardson and Cairns, 2019) due to limited resources. The severity of nosocomial infections in Africa is as shown in Figure 1.1 (Elizabeth *et al.*, 2019).

The "ESKAPE" pathogens have been linked to the leading cause of nosocomial infections. This group of pathogens consists of both Gram-positive and Gram-negative species, comprising *Enterococcus faecium, Staphylococcus aureus, Klebsiella pneumoniae, Acinetobacter baumannii, Pseudomonas aeruginosa, and Enterobacter* spp. (Rice, 2008). These pathogens are especially problematic, accounting for about 40% of infections in ICU (Hidron *et al.*, 2008). They are characterised by the ability to escape the biocidal action of antibacterial drugs effectively. Hence, they are difficult to eliminate (Rice, 2010; Pendleton *et al.*, 2013; Santajit and Indrawattana, 2016) and are notable contributors of morbidity, prolonged hospitalisation, death, and doubts in orthodox medicine (Boucher *et al.*, 2009). The latter stems from the fact that over the years, these pathogens have continued to express increasing antibiotic resistance, and this has been evident in *K. pneumoniae* resistance to extended-

spectrum cephalosporin and carbapenem, *E. faecium* resistance to vancomycin (VRE), *P. aeruginosa* resistance to fluoroquinolone and carbapenem, *S. aureus* resistance to methicillin (MRSA), *Enterobacteriaceae* resistance to fluoroquinolone and carbapenem, and *A. baumannii* resistance to carbapenem (System, 2004; Chambers, 2005; Moland *et al.*, 2006; Deshpande *et al.*, 2007; Lewis *et al.*, 2007; Lockhart *et al.*, 2007; Hidron *et al.*, 2008).

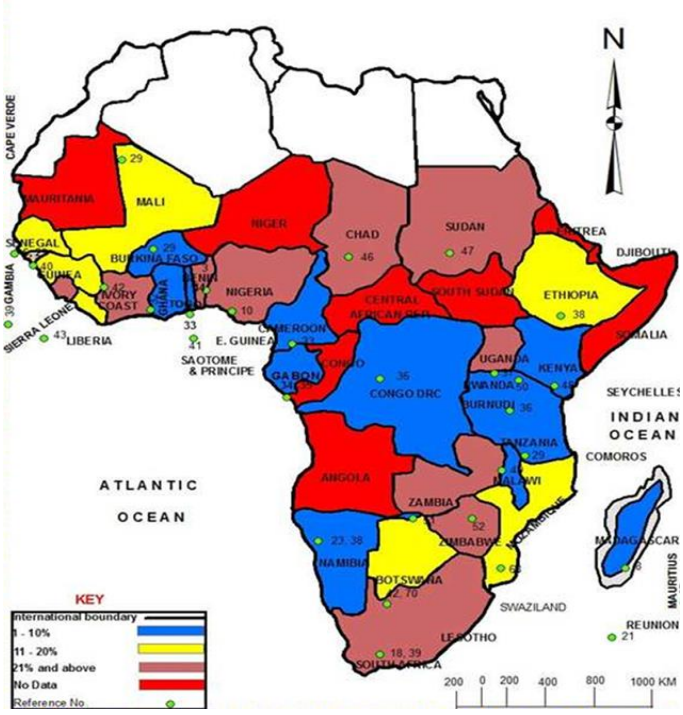

Figure 1.1. Map showing the regional distribution of nosocomial infections in Sub Saharan countries.
The prevalence rates of the infections vary across African countries, with South Africa having over 21% nosocomial infection rate (Elizabeth *et al.*, 2019)

Though the World Health Organisation is making efforts, unsanitary healthcare settings and multidrug resistance have continued to aid the rapid spread of these pathogens.

1.1.1 *Klebsiella pneumoniae*

The species *K. pneumoniae* is a Gram-negative bacillus linked to the Enterobacteriaceae family. They are found as saprophytes, colonising the gastrointestinal tract, skin, and nasopharynx in humans. However, the entrance of the bacterium into the respiratory tract or bloodstream via medical devices such as ventilators and catheters result in many infections arising, which shows resistance to antibiotics. The structural features such as capsules, fimbriae, lipopolysaccharide layer, and adhesins, as well as their ability to efficiently colonise coupled with their resistance to antibiotics, have contributed to their pathogenicity and

aided the persistence and rapid spread of *K. pneumoniae* in health care settings (Tzouvelekis *et al.*, 2012).

K. pneumoniae account for a significant proportion of nosocomial infections, including urinary tract infections (6–17%), pneumoniae (7–14%), bloodstream infections (4–17%), wound or surgical site infections (2–4%), and septicemias (4–15%) (Podschun and Ullmann, 1998). Furthermore, about 7–14% of nosocomial infections in ICU and 3–20% Neonatal septicemia are caused by *K. pneumoniae.* The most common site of *Klebsiella* infection is the urinary tract, with higher incidence recorded in patients with neuropathic bladders or diabetes mellitus (Lye *et al.*, 1992; Bennett *et al.*, 1995).

By nature, *K. pneumoniae* produces limited chromosomal penicillinases hence is susceptible to most classes of antibiotics. However, its famous ability to acquire MDR plasmids among different members of the *Enterobacteriaceae* has led to new strains of *K. pneumoniae* that contain MDR plasmids (Podschun and Ullmann, 1998). Over the years, several strains of *K. pneumoniae* have accumulated a wide range of β-lactamase enzymes, capable of inactivating or altering the structure of β-lactam antibiotics including penicillin, carbapenems, monobactams and cephalosporins (Santajit and Indrawattana, 2016). Furthermore, MDR plasmids such as plasmids encoding resistance to extended-spectrum β-lactamases (ESBLs), aminoglycosides as well as resistance to different antibiotics other than β -lactams have also been accumulated by *K. pneumoniae* strains. This continued acquisition of genetic materials in addition to the rapid increase of chromosomal mutations has also conferred their resistance to fluoroquinolones (Podschun and Ullmann, 1998). Until recent decades carbapenems were used as the last resort against Gram-negative infections showing resistance to other antibiotics; however, because of the rapid spread of *K. pneumoniae* strains possessing MDR "carbapenemases" (Tzouvelekis *et al.*, 2012), increasing incidences of carbapenem-resistant *K. pneumoniae* (CRKP) have emerged. These isolates resulted in resistance to antibiotics, including imipenem, amoxicillin/clavulanate, meropenem, piperacillin/tazobactam, aztreonam, ceftazidime, and ceftriaxone (Santajit and Indrawattana, 2016). Moreover, the upsurge of New Delhi Metallo-β-lactamase-1 (NDM-1) enzymes in *K. pneumoniae* (Rice, 2010) has amplified the amount of *K. pneumoniae* strains resistant to carbapenem. Hence, posing a threat to more β-lactams, aminoglycosides, and fluoroquinolones antibiotics (Kumarasamy *et al.*, 2010). Figure 1.2 shows the global impact of *K. pneumoniae* carbapenemase (KPC), OXA-48 group carbapenemases and NDM (Vasoo *et al.*, 2015).

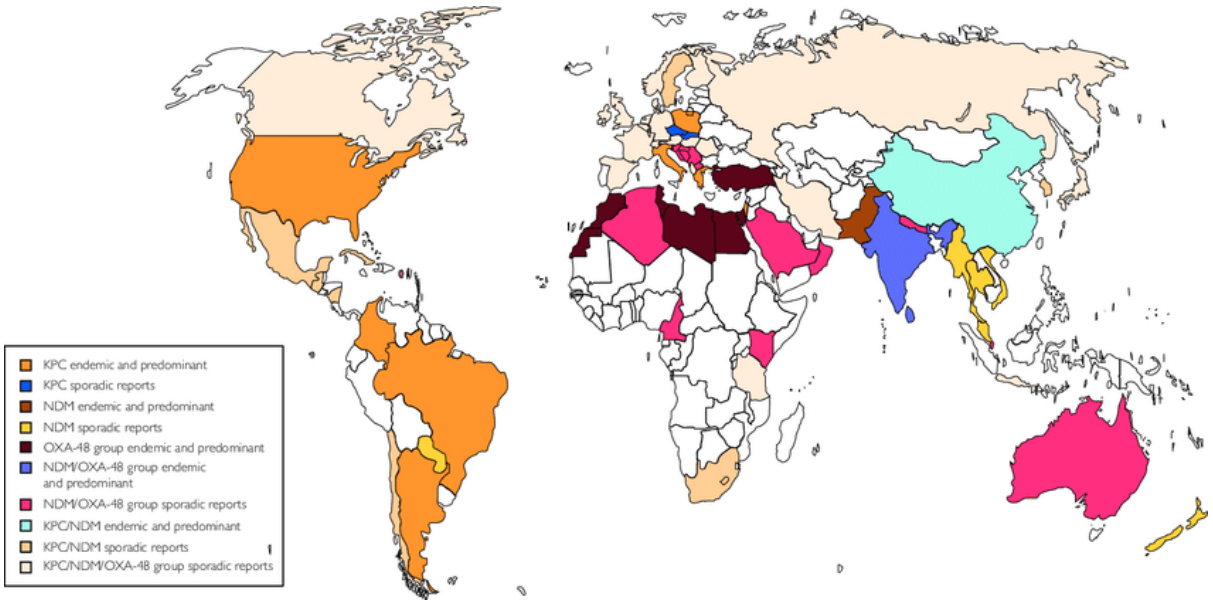

Figure 1.2. Map showing the distribution of OXA-48 group carbapenemases, *K. pneumoniae* carbapenemase (KPC), and New Delhi Metallo-β-lactamase (NDM) across the globe.
KPC and NDM have been reported for South Africa (Vasoo *et al.*, 2015).

1.1.2 *Enterococcus faecium*

Until recent decades, Gram-positive *E. faecium* was classified as a low virulent pathogen (Oprea *et al.*, 2004) living as microflora in humans. (Robert C. Moellering, 1992). However, this commensal role has evolved over the years to be pathogenic in humans due to excessive and improper administration of antibiotics, resulting in the development of strains resistant to such antibiotics. Furthermore, colonisation, extra-chromosome and mobile genetic elements, extracellular proteins biofilm formation, components cell wall, and adherence factors have also been identified as contributing factors to the ability of *E. faecium* to survive and cause infection in a host (Treitman *et al.*, 2005; Gao *et al.*, 2018). Even though *E. faecium* are not naturally virulent as some other bacterial pathogens, the ability to acquire and exchange antibiotic resistance determinants, in addition to its innate resistance to many antibiotics selectively, provides *E. faecium* an added advantage in environments with heavy antibiotic usage such as hospitals, thereby allowing them to out-grow other species that would ordinarily keep them in check.

Several nosocomial infections have been associated with *E. faecium*, including urinary tract infections, bloodstream infections, and endocarditis, with surgical wound infection accounting for its highest count (Oprea *et al.*, 2004; Daniel *et al.*, 2015). *E. faecium* accounts for the second most prominent nosocomial-causing pathogen in ICU patients after *Staphylococcus aureus*. It is ranked as the third major cause of urinary tract infection and

bloodstream infection (Elward *et al.*, 2001; Daniel *et al.*, 2015; Edwardson and Cairns, 2019). The antimicrobial properties demonstrated by *E. faecium* is characterised by the possession of plasmid-encoded resistance gene that allows them to transfer genetic information within themselves and between different species via horizontal gene transfer (Oprea *et al.*, 2004). This characteristic, therefore, makes *Enterococci* infections persistent, as evident in different studies where *E. faecium* displayed more than 90% resistance to ampicillin and ciprofloxacin, 80% resistance to vancomycin (Treitman *et al.*, 2005; Hidron *et al.*, 2008), 67% resistance to Teicoplanin, 37% resistance to gentamicin (HL), and 65% resistance to rifampin (Leavis *et al.*, 2003; Leavis *et al.*, 2006; Deshpande *et al.*, 2007). Figure 1.3 illustrates vancomycin-resistant *E. faecium* distribution globally, with the highest incidence reported in developing countries (Jabbari Shiadeh *et al.*, 2019).

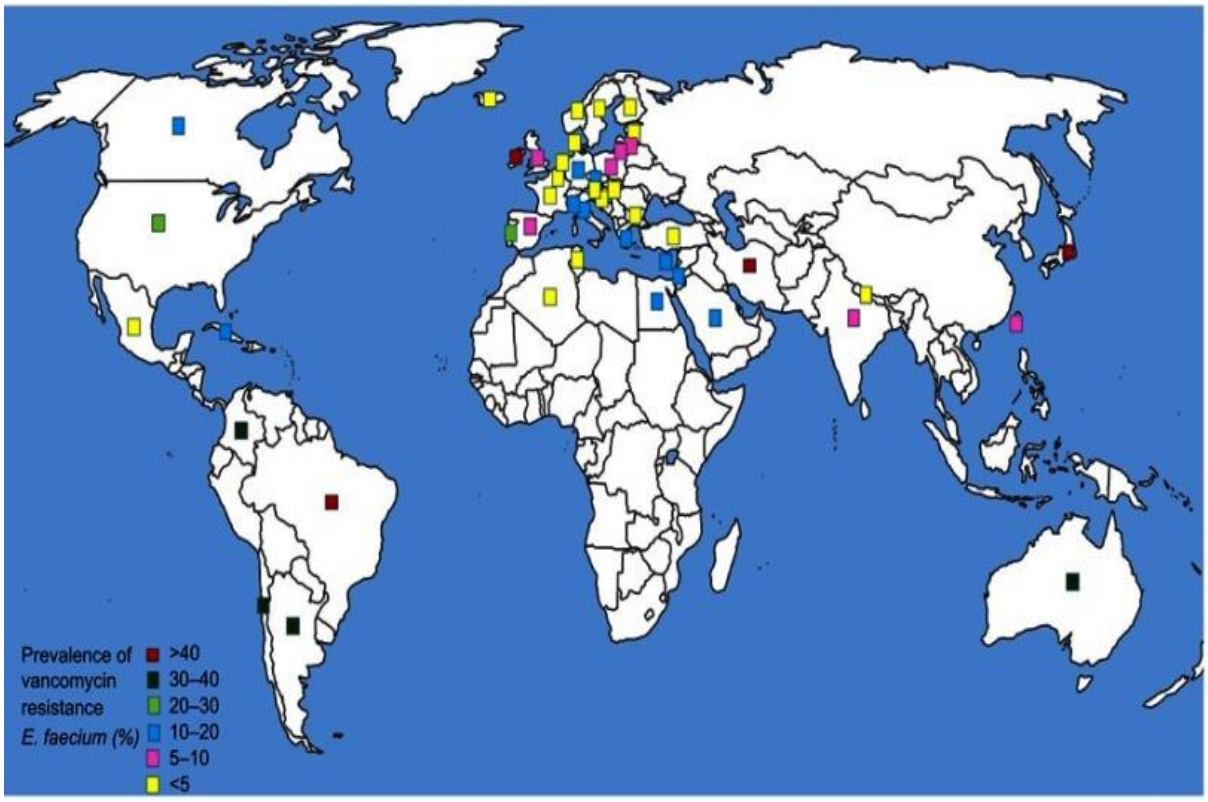

Figure 1.3. Map illustrating the spread of vancomycin-resistant *E. faecium* in bloodstream infections across the globe.
As against other developing countries around the Eastern Mediterranean region with high levels of vancomycin resistance, in African countries, the highest resistance was observed with ampicillin (Jabbari Shiadeh et al., 2019).

1.2 Rationale

Despite many innovative therapies that have been developed to combat multi-resistant *K. pneumoniae* and *E. faecium*, including the use of combination therapy, improvement on β-lactamase inhibitors, new antibiotics, nanoparticles, phage therapy, and antimicrobial peptides (Mandal *et al.*, 2014), *K. pneumoniae* and *E. faecium* insurgence persist (De Angelis *et al.*, 2018); thus signifying the urgency in identifying novel alternative targets and effective antibacterial agents. Furthermore, seeing that most of the prevailing antibiotics utilise DNA synthesis and cellular functions like interfering with proteins involved in the synthesis of cell wall as targets, it is paramount that more alternative targets are identified.

In relation to this, targeting the biosynthesis of nicotinamide adenine dinucleotide (NAD^+) appears to be a valid pathway to explore for new therapeutics for infections caused by *K. pneumoniae* and *E. faecium* (Gerdes *et al.*, 2002; Osterman and Begley, 2007; Sorci *et al.*, 2009), given the increasingly vital roles of NAD^+ and its derivatives in cellular and biological processes. Its function ranges from DNA repair (Wilkinson *et al.*, 2001), energy metabolism, redox reactions (Brekasis and Paget, 2003) to protein modification and gene regulation (Ziegler, 2000). These, therefore, highlights the need to sustain NAD^+ homeostasis, given that most bacteria species are unable to take up NAD^+ from their environment, and an alteration in the regulation of NAD^+ synthesis or degradation would likely impair the metabolic state of the cell (Rodionova *et al.*, 2014) and ultimately result in death.

The enzymes involved in the downstream formation of NAD^+ are potential targets for drug discovery. However, this study focuses on nicotinate mononucleotide adenylyltransferase (NaMNAT), given that the reaction catalysed by NaMNAT constitutes the crucial step leading to the formation of pyridine dinucleotides. Since there is no other known route leading to pyridine dinucleotides formation, the role of NaMNAT activity in NAD^+ synthesis is unequivocally indispensable. Furthermore, compared to other enzymes driving the downstream formation of NAD^+, bacteria NaMNAT exhibits the least sequence identity and structural similarity to its human homology (section 2.2.4) (Gerdes *et al.*, 2002; Zhou *et al.*, 2002); thus, making it a more suitable antibacterial target for design of specific inhibitors. Besides, studies on structure-based inhibitor development using a protein knockdown approach to induce deprivation of NaMNAT demonstrated antibacterial activity (Sorci *et al.*, 2009; Rodionova *et al.*, 2014). These findings validate NaMNAT to be an attractive target.

Though NaMNAT activity is widely conserved in almost all species, the respective enzymes exhibit different structural and catalytic properties that reflect their species and

specificity (Lau *et al.*, 2009). A preliminary study on the phylogeny of NaMNAT, as shown in Figure 1.4, reveal an evolutionary divergence of NaMNAT among bacteria, despite all being prokaryotes. Sequence alignment of multiple bacteria NaMNAT also confirms evolutionary variation (Appendix B S1)

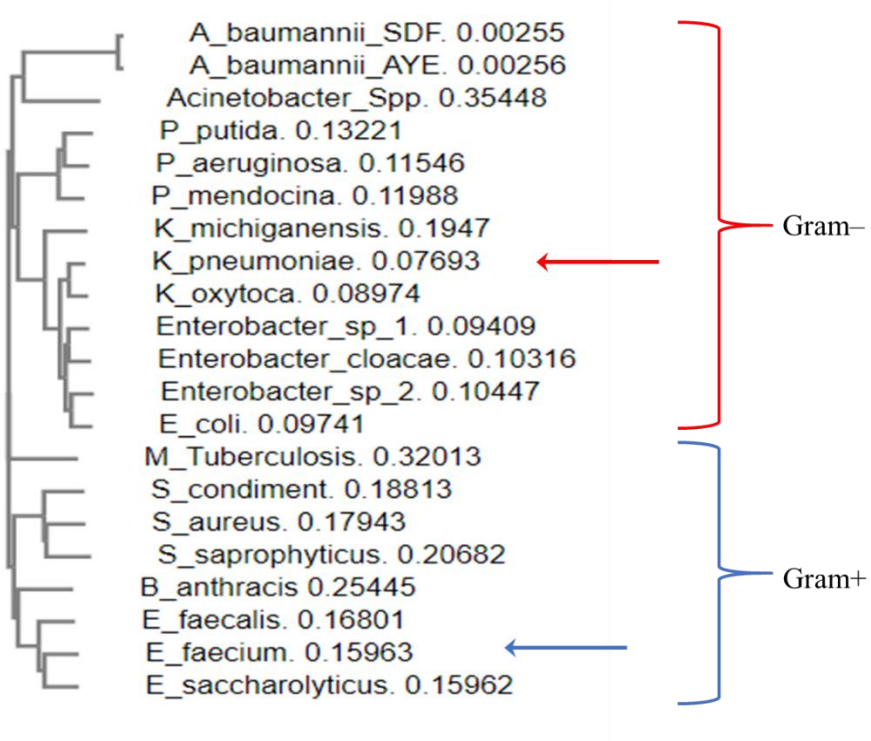

Figure 1.4. Phylogram of NaMNAT from different bacteria showing it's evolutionary divergence among Gram-positive and Gram-negative bacteria.
Numbers indicate in the figure represents distances between sequences. The closer the numbers are, the more matching the sequences. Analysis was carried out using Clustal Omega multiple sequence alignment tool.

Comparing the sequence alignment between *Kp*NaMNAT and *Ef*NaMNAT (Figure 1.5) shows a divergence in their sequence similarity. These differences demonstrated by the enzymes in their sequence similarities may contribute to their distinctive biophysical properties, structure and possible function.

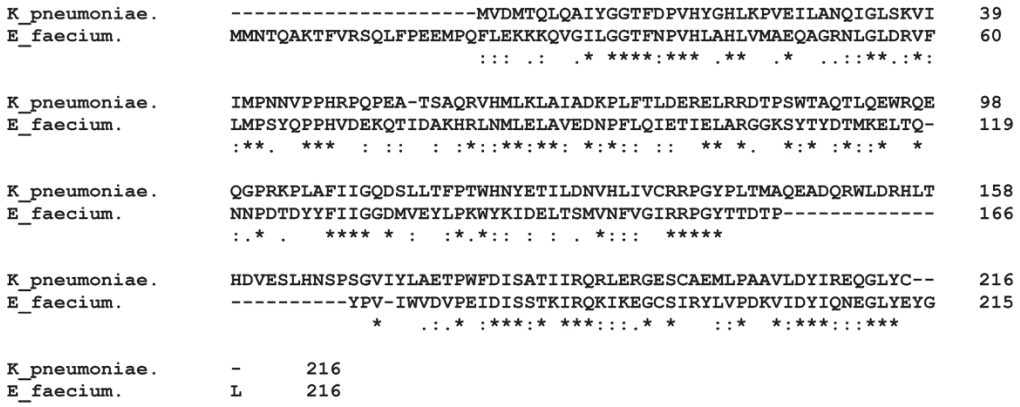

Figure 1.5. Sequence alignment between *Kp*NaMNAT and *Ef*NaMNAT.
This shows the divergence in their sequence similarity. The positions with conserved residues are indicated as (*), while residues with strongly similar properties or conserved mutation are indicated as (:), and semi-conserved residues with weak similar properties represented as ".". The empty space denotes non-conserved residues. This image was generated from EMBOSS Stretcher pairwise alignment tool.

All NaMNAT characterised thus far are metal-activated enzyme, that employs divalent cations for co-substrate binding and catalysis. Many studies have established NaMNAT isozyme to have a distinctive preference for varied divalent metal ions (Emanuelli *et al.*, 1999; Raffaelli *et al.*, 2002; Sorci *et al.*, 2007). This variation of metal ion specificity may impact variation in structure, consequently contributing to the enzyme's distinctive function and substrate utilisation.

Therefore, it is paramount to understand the biophysical structure of the individual enzymes, their functions as well as catalytic mechanism and dynamics, both in the presence and absence of cations in order to successfully design molecular compounds that can selectively inhibit the activity of NaMNAT enzyme in *K. pneumoniae* and *E. faecium*.

1.3 Aim and Objectives

The aim of this study is to describe the biophysical characteristics of recombinant *K. pneumoniae* NaMNAT (*Kp*NaMNAT) and *E. faecium* NaMNAT (*EfNaMNAT*) using empirical studies and computational modelling.

Until now, very limited information has been established on NaMNAT (EC 2.7.1.18) from *K. pneumoniae* and *E. faecium.* Hence, this study intends to describe the distinctive structural and functional features of NaMNAT from a Gram-negative *Klebsiella pneumoniae* and a Gram-positive *Enterococcus faecium* as well as observe their variances. This study will also

assess the impact of varying bivalent metal ions on the activity and conformation of the enzymes at different pH, considering that NaMNAT is a metal activated enzyme with preferences for different divalent cations.

To achieve this aim, the following four folded objectives were set.

- To express the recombinant *Kp*NaMNAT and *Ef*NaMNAT in *E. coli* T7 expression system using pET-11a and pET-28a vector construct and purify the expressed proteins through immobilised metal affinity chromatography.
- To determine the activity of the enzymes using a dual enzyme-catalysed reaction that will enable quantification of activity based on NADH production.
- To determine the secondary structure contents, the tertiary and quaternary structures of the recombinant *Kp*NaMNAT and *Ef*NaMNAT utilising far-UV (ultraviolet) circular dichroism spectroscopy, fluorescence spectroscopy, thermal shift assay, and size-exclusion high-performance liquid chromatography, respectively.
- To computationally analyse the interactions between the proteins and the ligands, as well as the impact of Mg^{2+} on the dynamics of the protein and ligands via molecular modelling, induced-fit docking, and molecular dynamic simulation.

Chapter 2

LITERATURE REVIEW

2.1 Nicotinamide Adenine Dinucleotide (NAD^+) Metabolism

2.1.1 NAD^+/NADH and its biological roles

Nicotinamide adenine dinucleotide (NAD^+) is a ubiquitous metabolite in both prokaryotic and eukaryotic cells, given its direct effect on nearly all metabolic pathways. The indispensability of NAD revolves around its existence as an oxidising (NAD^+) and reducing agent (NADH), transferring electrons and driving hundreds of biochemical reactions and metabolic pathways. Beyond functioning in redox reactions as a coenzyme, NAD^+ is utilised as a co-substrate by non-redox NAD^+-hydrolysing enzymes such as bacterial DNA ligases for repairs of DNA (Wilkinson *et al.*, 2001), protein lysine, and histone deacetylase of the CobB and Sir2 family (sirtuins) (Imai *et al.*, 2000) to remove the acetyl group from lysine residues on protein. Also, poly ADP- ribose polymerases (PARPs) and ADP ribosyltransferases (ARTs) use NAD^+ as a donor of ADP-ribose moieties for protein modification and generation of long poly (ADP-ribose) (PAR) chains for regulation of gene respectively (Ziegler, 2000) (Figure 2.1**)**. Furthermore, NAD^+ is used as a precursor to cyclic ADP- ribose for calcium homeostasis (Lee, 1997), as a substrate in the synthesis of cobalamin (Berger *et al.*, 2004) as well as in the activation of diphtheria (Murphy, 2011) and cholera toxins (Dolan *et al.*, 2000).

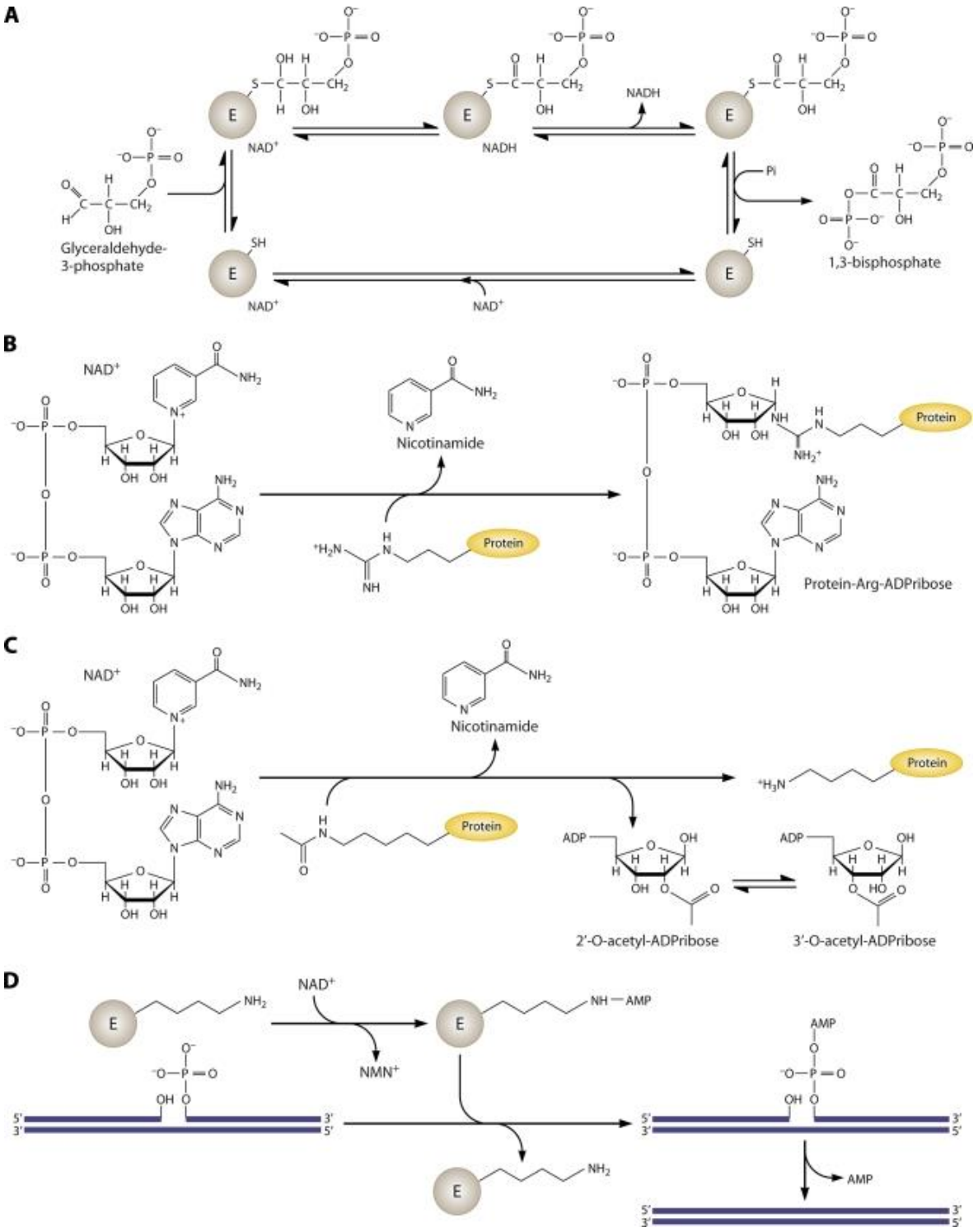

Figure 2.1. Biochemical reactions demonstrating the biological roles of NAD$^+$.
(A) NAD$^+$ functioning as a coenzyme in the conversion of glyceraldehyde 3-phosphate to 1,3-bisphosphate by glyceraldehyde phosphate dehydrogenase with its reduction to NADH. (B) Depicts NAD$^+$ as a substrate for ADP-ribose transferases, donating ADP-ribose with the formation of nicotinamide. (C) Reaction involving NAD$^+$-dependent Sirtuins (Sir2). Sir2 transfers ADP-ribose to acetyl groups by cleaving to NAD$^+$, forming 2′- and 3′-acetylated ADP-ribose and nicotinamide. (D) Bacterial DNA ligases use NAD$^+$ for the adenylation of the ligase active to form an adenylated nicked substrate (Gazzaniga et al., 2009).

2.1.2 Redox metabolic pathways involving NAD^+ in bacteria

NAD^+ as a cofactor in redox metabolism readily adjust with no net consumption between the reduced (NADH) and the oxidised (NAD^+) forms, transferring hydride across the cell and acting as hydride acceptors and donors for energy metabolism. Its reduction to $NADP^+$ allows for its participation in reductive biosynthesis and maintenance of redox activity ($NADP^+$/NADPH). Many dehydrogenases utilise NAD^+ and its derivatives as major electron acceptors or donors, and virtually every metabolic pathway requires these molecules (Brekasis and Paget, 2003; Sauve, 2008). Figure 2.2 shows some of the crucial metabolic pathways that heavily depend on the utilisation of NAD(H).

In the glycolytic pathway and Kreb cycle, NAD^+ participates in energy generation by transferring reducing equivalents in the form of NADH. The β-oxidation pathway and glyoxylate cycle also utilises NAD^+ as a hydride acceptor to complete their oxidative pathway. The conversion of pyruvate to lactate via a fermentation process utilises NADH as a hydride donor. The Electron-transport chain utilises NADH generated through series of oxidation-reduction electron transfers to release free energy use to produce ATP (Figure 2.2). Furthermore, the formation of pyruvate from malate and the pentose phosphate pathway utilises $NADP^+$ to transfer reducing equivalents in the form of NADPH which can be used as a reducing agent in the synthesis of cholesterol, fatty acids, nucleic acid, and nucleotides. Given that synthesis efficiency and energy generation are limited by the generation of NAD(P), the maintenance of this redox couple is imperative to avoid the entire collapse of the central metabolic system, especially since the pathways are linked.

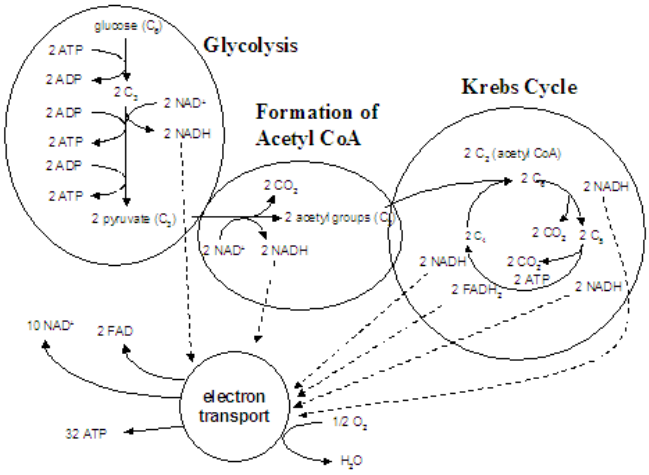

Figure 2.2. A schematic representation of linked metabolic pathways involving the redox activity of NAD^+/NADH to generate energy.
(Brekasis and Paget, 2003; Sauve, 2008).

2.1.3 NAD^+ synthesis in bacteria

In bacteria, the biosynthesis of NAD^+ is accomplished by two (2) biochemical pathways, the de novo synthesis and the pyridine ring salvage pathway (Figure 2.3). The *de novo* synthesis of NAD^+ uses amino acids as precursors. Most bacteria synthesise NAD^+ anaerobically using aspartate and dihydroxyacetone phosphate as a precursor (Liu *et al.*, 1982) to synthesise quinolinic acid in a two-step enzymatic reaction, while a few others synthesise NAD^+ aerobically from tryptophan via a 5 step enzymatic reaction to form quinolinic acid. The quinolinic acid formed from either tryptophan or aspartate precursor is Phosphoribosylated and decarboxylated by the enzyme quinolinic acid phosphoribosyltransferase (encoded as NadC), giving rise to nicotinate mononucleotide (NaMN). The NaMN formed is further adenylated by the enzyme NaMNAT (NadD) using ATP as a cofactor to form nicotinate adenine dinucleotide (NaAD). The resulting NaAD is then amidated to NAD^+ in the presence of ammonia and ATP in a reaction catalysed by NAD^+ synthetase (NadE) (Begley *et al.*, 2001; Kurnasov *et al.*, 2003).

Breakdown products from NAD^+ turnover containing pyridine bases like nicotinate (Na) and nicotinamide (Nm) are recycled through the pyridine ring salvage pathway to resynthesise NAD^+. The most common salvage pathway in bacteria is the two enzymatic steps (PncA-PncB salvage route) that involve the deamination of nicotinamide to nicotinate by nicotinamidase (PncA) and the linking of nicotinate to 5-phosphoribosyl-1-pyrophosphate (PRPP) by the enzyme nicotinate phosphoribosyltransferase (PncB) to form NaMN. The NaMN formed converges at the *de novo* pathway where it is adenylated and deamidated by NaMNAT and NAD synthase to form NaAD and NAD^+, respectively. Alternatively, nicotinamide is salvaged through NMN to synthesise NAD^+ by the enzyme nicotinamide phosphoribosyltransferase and NaMNAT, respectively (Figure 2.3). A few bacteria like *Haemophilus influenzae* which are NAD^+ auxotrophs, use different salvage pathways involving nicotinamide intermediate (ribosyl nicotinamide) to synthesise NAD^+. This is achieved through the PnuC-NadR nicotinamide riboside salvage pathway involving a two-step conversion of ribosyl nicotinamide to NAD^+ via phosphorylation by the enzyme nicotinamide riboside kinase (NmR kinase) and adenylation by NMNAT (NadR) respectively (Kurnasov *et al.*, 2002).

In summary, NaMN generated from the de novo pathway, as well as NaMN and NMN products generated from the salvage pathway, converge at the reaction catalysed by the enzyme NaMNAT to form their respective dinucleotides (NaAD and NAD^+) (Magni *et al.*, 1999). Meaning NaMNAT can catalyse both NaMN and NMN.

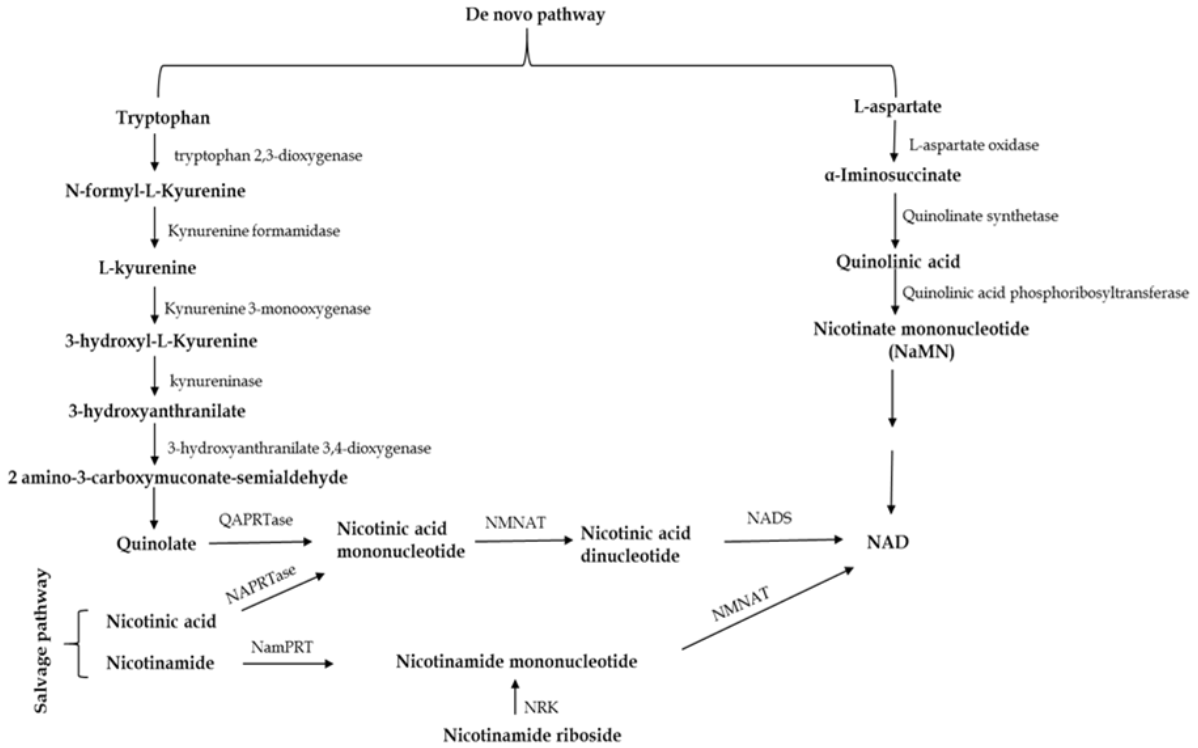

Figure 2.3. Schematic representation of the de novo and salvage synthesis of NAD^+ in bacteria and humans.
L-aspartate is the precursor amino acid utilised by bacteria anaerobically to synthesise NAD^+, while a few other bacteria and humans utilise tryptophan aerobically. NaMN generated from the *de novo* pathways employ NMNAT (Nicotinamide mononucleotide adenylyltransferase) to form $NaAD^+$ which is further deamidated to form NAD^+. Nicotinic acid, nicotinamide, and their corresponding ribosides resulting from NAD^+ breakdown and exogenous sources are salvaged to resynthesise NAD^+ via NaMN and NMN linked to the reaction catalysed by NMNAT to form NaAD and NAD^+ respectively (Jayaram *et al.*, 2011). QAPRTase (quinolinic acid phosphoribosyltransferase), NADS (NAD synthetase), NRK (nicotinamide riboside kinase), NamPRT (nicotinamide phosphoribosyltransferase), and NAPRTase (nicotinate phosphoribosyltransferase).

2.1.4 NAD^+ synthesis in human

In humans, NAD^+ is also synthesised via the de novo and pyridine salvage pathways. Like the de novo aerobic NAD^+ synthesise in bacteria (Figure 2.3), tryptophan serves as the precursor amino acid. The sequential steps leading to the formation of NAD^+ are also the same for humans.

The NAD^+ salvage pathway in humans serves as the chief source of NAD^+. Nicotinate and nicotinamide generated from exogenous sources and NAD^+-utilising enzyme turnover are coupled directly to PRPP by NAPRTase and NamPRT to form NaMN and NMN, respectively. NMNAT further adenylates the generated mononucleotides to form NaAD and NAD^+. The NaAD formed is ultimately converted to NAD^+ by NAD^+ synthase. Additionally, exogenous

nicotinamide ribosides are salvage to synthesise NAD^+ via phosphorylation and adenylation reactions catalysed by NRK and NMNAT, respectively (Bieganowski and Brenner, 2004).

Interestingly, the successive biosynthetic steps to the formation of NAD^+ from quinolinic acid are well sustained in bacteria and humans. These reactions are catalysed by analogous enzyme sets, although with some notable disparities (Katoh and Hashimoto, 2004). Amongst the enzymes that drive the downstream conversion of quinolinate to NAD^+, NaMNAT represents a potential antibacterial target because of its lowest sequence identity and more distant structure to its human homology (Zhou *et al.*, 2002)

2.2 Nicotinate Mononucleotide Adenylyltransferase (NaMNAT) the key Enzyme in NAD^+ Synthesis

2.2.1 The enzyme NaMNAT

Nicotinate mononucleotide adenylyltransferase (NaMNAT) is a crucial enzyme involved in the *de novo* and salvage synthesis of NAD^+, responsible for the adenylation step leading to the formation of pyridine dinucleotides. Since all pathways converge at the reaction catalysed by NaMNAT, and there is no other route leading to pyridine dinucleotides formation, the synthesis of NAD^+ is considered the physiological activity of NaMNAT. NaMNAT belongs to the superfamily of nucleotidyltransferase α/β phosphodiesterase (EC 2.7.7), characterised by a highly preserved "H/TXGH" signature motif and the presence of a Rossmann fold (Izard and Geerlof, 1999; D'Angelo *et al.*, 2000). Most NaMNAT can catalyse the adenylation of both NMN and NaMN (Figure 2.4), but at a different degree of specificity and depending on the substrate preference, it is either termed NMNAT (EC 2.7.7.1) or NaMNAT (EC 2.7.7.18). This dual substrate enzyme catalyses the adenylation of both NMN and NaMN by transferring the adenyl group from ATP to NMN and NaMN, forming nicotinamide adenine dinucleotide (NAD^+) and nicotinate adenine dinucleotide (NaAD) respectively with the release of inorganic pyrophosphate. This reaction involves a nucleophilic attack on the ATP α-phosphoryl group by the mononucleotide substrate (Lowe and Tansley, 1983).

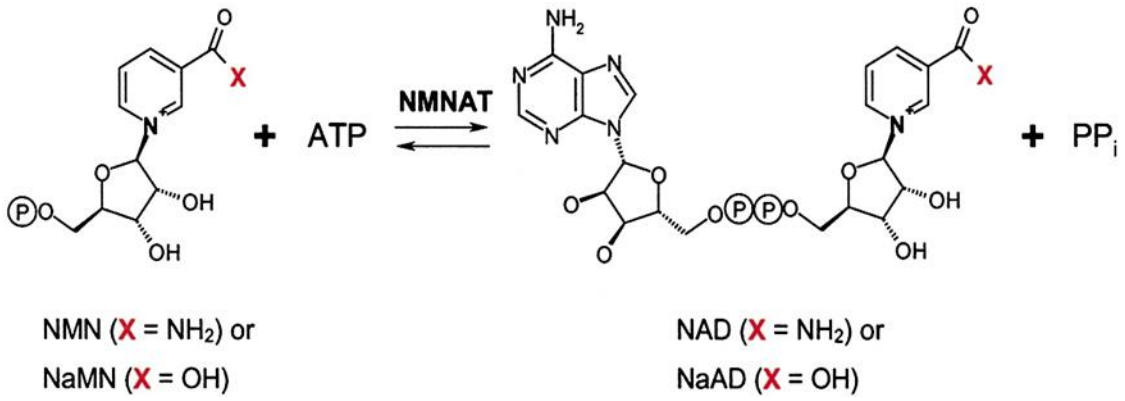

Figure 2.4. The reaction catalysed by nicotinate/nicotinamide mononucleotide adenylyltransferase.
The diagram depicts the dual substrate catalysed reaction of NMNAT enzyme resulting in NAD^+ or NaAD synthesis (Zhang *et al.*, 2002).

2.2.2 Physicochemical properties of Na/NMNAT

Na/NMNATs exhibit optimum pH between 6.0 and 9.0 and are metal activated enzymes requiring the presence of divalent metal ions for substrate binding and catalysis of adenylyl transfer reaction. Specific preference for varied divalent metal ions other than magnesium ion has been established amongst Na/NMNAT isozymes (Emanuelli *et al.*, 1999; Raffaelli *et al.*, 1999; Raffaelli *et al.*, 2002; Di Stefano *et al.*, 2010). Furthermore, Na/NMNATs are globular proteins comprising about 160-400 amino acids, with subunit mass ranging between 20 and 50 kDa. Most characterised Na/NMNATs exist as homo-oligomers of 2-6 identical subunits (Lau *et al.*, 2009). Though NaMNAT activity is widely conserved, the enzyme and isoforms exhibit different structural and catalytic properties that reflect their species, specificity, and other functions acquired (Lau *et al.*, 2009).

2.2.3 A typical bacterial NaMNAT

The bacterial (NadD) NaMNAT (EC 2.7.1.18) is conserved in almost all bacteria and demonstrates a higher preference for NaMN over NMN (Magni *et al.*, 1999). The substrate specificity of NadD bacteria NaMNATs for NaMN is mediated by the carboxylate group of the substrate, which interacts with an anion binding pocket formed by the main-chain amide groups of a threonine and histidine. Furthermore, the comparison of the quaternary structures shows high similarities and trends. For instance, Gram-positive bacteria NaMNAT as seen in *S. aureus (sa*NaMNAT*)* (Han *et al.*, 2006), B. *subtilis (bs*NaMNAT*)* (Olland *et al.*, 2002), and *B. anthracis* (*ba*NaMNAT) (Lu *et al.*, 2008) are distinguishable by structure dimerisation and common substrate preference for NaMN. Similarly, the Gram-negative bacteria share a typical distinctive monomeric structure and preference for NaMN substrate as observed in

P. aeruginosa (*pa*NaMNAT) (Yoon *et al.*, 2005), *E. coli* (*Ec*NaMNAT-NadD) (Mehl *et al.*, 2000; Zhang *et al.*, 2002) and *baumannii* NaMNAT (Sorci *et al.*, 2010).

To date, limited information is available for both *Kp*NaMNAT and *Ef*NaMNAT neither is there any solved crystal structure of the NaMNAT proteins. However, considering the first bacterial NaMNAT discovered, *Ec*NaMNAT (Uniprot ID: P0A752), which shares about 85% sequence similarity with *Kp*NaMNAT (Uniprot ID: B5XZR5) and 50% with *Ef*NaMNAT (Uniprot ID: A0A133MWI0), its secondary structure is made of a seven-stranded parallel central β-sheet fringed by many helices (Figure 2.7). The 25 kDa *Ec*NaMNAT function as a monomeric unit and its crystal structure, as determined by Zhang *et al*., revealed that the enzyme exhibits structural flexibility at several regions around the active site, which mediates the binding of substrate and release of product. *Ec*NaMNAT specifically recognises the NaMN substrate through the nicotinate carboxyl group, which interacts with a positive helix dipole and the numerous protein main chain amides (Zhang *et al.*, 2002; Yoon *et al.*, 2005).

2.2.4 Overview of *Kp*NaMNAT and *Ef*NaMNAT structure.

*Kp*NaMNAT comprises 216 amino acids with a predicted molecular weight of ~24.8 kDa and a theoretical isoelectric point (pI) of 5.82. Because *Kp*NaMNAT contains two cysteine residues, its extinction coefficient measured in water at 280 nm is 38055 M^{-1} cm^{-1}, assuming all pairs of cysteine residues form cystine and 37930 M^{-1} cm^{-1} assuming all cysteine residues are reduced (ProtParam ExPASY). On the other hand, *Ef*NaMNAT comprises 213 amino acids, with a predicted molecular weight of ~24.6 kDa and a theoretical pI of 5.17. Its molar extinction coefficient measured in water at 280 nm is 30370 M^{-1} cm^{-1} (ProtParam ExPASY).

Based on the predicted homology model generated using *Ec*NaMNAT (PDB ID:1k4k), which shares ~76% sequence identity with *Kp*NaMNAT, *Kp*NaMNAT exists as a monomeric structure. While *Ef*NaMNAT exists as homo-dimer (Figure 2.5), as revealed from its homology model generated using *Bacillus anthracis* (*Ba*NaMNAT- PDB ID:2QTN), which shares ~46% sequence identity (Swissmodel.expasy.org). The secondary structures of both proteins are conserved and characterised by the presence of a Rossman fold.

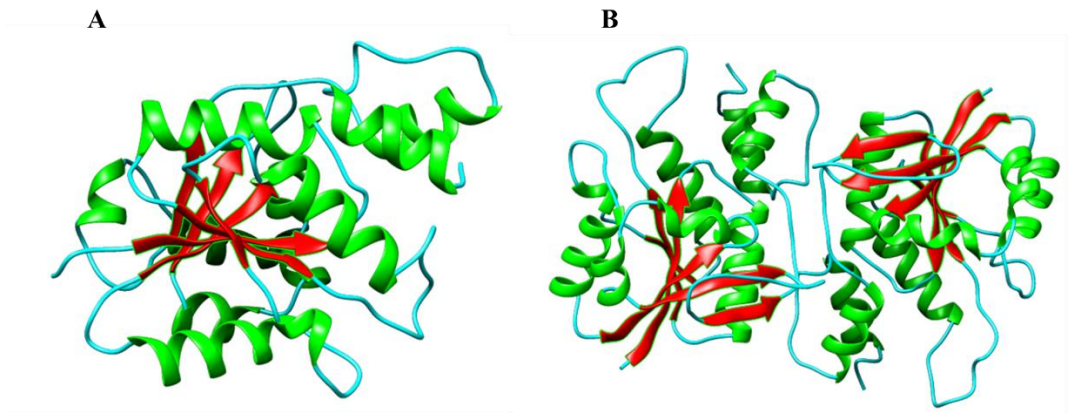

Figure 2.5. Predicted structure of (A) *Kp*NaMNAT and (B) *Ef*NaMNAT.
*Kp*NaMNAT model was built using 1k4k.4.A template while *Ef*NaMNAT was built using 2qtn.1.A model, through SwissModel. The α-helices are represented in green, β-strands in red, and the unordered coils in Cyan.

Sequence alignment analysis between *Kp*NaMNAT and *Ef*NaMNAT revealed ~47% sequence similarity using EMBOSS Stretcher pairwise alignment tool (Figure 2.6). Residues like Trp120 and Asp112 in *Kp*NaMNAT, which corresponds to Trp138, and Asp130 in *Ef*NaMNAT are conserved and contribute to conformational changes upon NAD^+ binding (Zhang *et al*., 2002). One of the two cysteine residues of *Kp*NaMNAT, Cys135, is located within the active site next to Arg136 and Arg137, involved in substrate binding and catalysis. These arginine residues correspond to Arg154 and Arg155 in *Ef*NaMNAT, which interacts with the phosphate group of the nucleotide ligand (Olland *et al.*, 2002; Zhang *et al.*, 2002). Furthermore, His48 of *Kp*NaMNAT corresponding to His66 in *Ef*NaMNAT is involved in the binding of mononucleotide substrate. It aids in the stacking of the pyridine ring via π-cation interactions and creates a negative charge pocket for exocyclic carboxylate interactions (Wang *et al*., 2017).

Aside from the conserved residues, several alterations or substitutions in the amino acid residues of *Kp*NaMNAT and *Ef*NaMNAT are observed that may change substrate binding or catalytic activity. The highly conserved "H/TXGH" signature motif sequence required for recognition and binding of substrates (Izard and Geerlof, 1999) in *Kp*NaMNAT is identified as "HYGH" and located close to the N-terminus between residues 19 and 22. In *Ef*NaMNAT, the glycine of the motif is replaced with alanine hence, identified as "HLAH" (Figure 2.6). The "HLAH" signature motif is located between residues 37 and 40.

```
K_pneumoniae.       ---------------------MVDMTQLQAIYGGTFDPVHYGHLKPVEILANQIGLSKVI    39
E_faecium.          MMNTQAKTFVRSQLFPEEMPQFLEKKKQVGILGGTFNPVHLAHLVMAEQAGRNLGLDRVF    60
                                        ::: .:  .* ****:***  .**  .*  ..::**.:*:

K_pneumoniae.       IMPNNVPPHRPQPEA-TSAQRVHMLKLAIADKPLFTLDERELRRDTPSWTAQTLQEWRQE    98
E_faecium.          LMPSYQPPHVDEKQTIDAKHRLNMLELAVEDNPFLQIETIELARGGKSYTYDTMKELTQ-    119
                    :**.  ***  : ::  : :*::**:**: *:*:: ::  ** *.  *:* :*::*  *

K_pneumoniae.       QGPRKPLAFIIGQDSLLTFPTWHNYETILDNVHLIVCRRPGYPLTMAQEADQRWLDRHLT    158
E_faecium.          NNPDTDYYFIIGGDMVEYLPKWYKIDELTSMVNFVGIRRPGYTTDTP-------------    166
                    :.* .   **** * :  :*.*:: : : . *:::  *****

K_pneumoniae.       HDVESLHNSPSGVIYLAETPWFDISATIIRQRLERGESCAEMLPAAVLDYIREQGLYC--    216
E_faecium.          ----------YPV-IWVDVPEIDISSTKIRQKIKEGCSIRYLVPDKVIDYIQNEGLYEYG    215
                               *   .:.* :***:* ***:::.* *   ::*  *:***:::***

K_pneumoniae.       -      216
E_faecium.          L      216
```

Figure 2.6. Sequence alignment between *Kp*NaMNAT and *Ef*NaMNAT.
The image was generated from EMBOSS Stretcher pairwise alignment tool. The highly conserved "H/TXGH" signature motif sequence for the proteins is indicated in the red box.

2.2.5 Comparison between bacterial and human NMNAT

Although bacteria and human Na/NMNAT are affiliated to the same nucleotidyltransferase superfamily, they share less than 20% sequence identity. Several biochemical studies as related to NMNAT discloses that both bacteria and human Na/NMNAT are two unique subfamilies, exhibiting differences in sequence conservation patterns, mononucleotide substrate specificity, oligomeric states, biochemical as well as enzymatic properties (Figure 2.7) (Magni *et al.*, 1999; Raffaelli *et al.*, 1999).

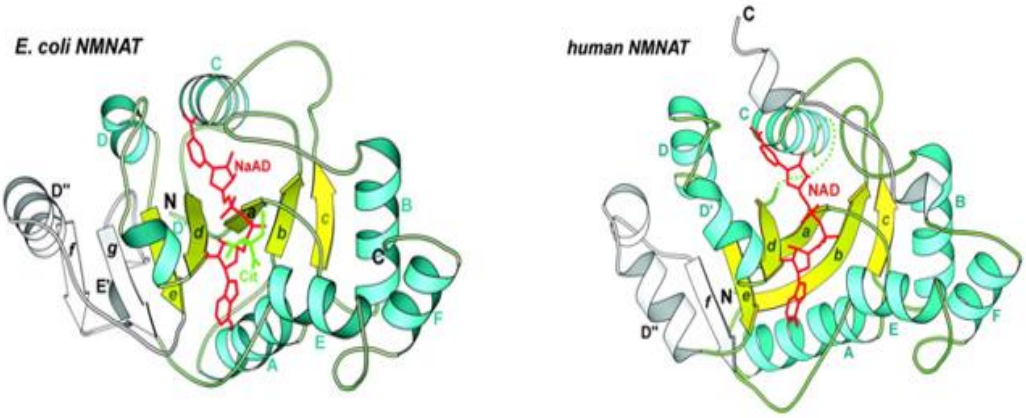

Figure 2.7. Ribbon representation showing the difference between *E. coli* NaMNAT and human NMNAT protomer structure.
The bound ligands are represented by *red sticks* for NaAD or NAD^+, while the SO_4^{2-} and citrate are represented with green *sticks*. The secondary structures are labelled grey for the random coils, yellow for strands, and cyan for helices. The dotted line indicates the disordered region in hsNMNAT (Zhou et al., 2002).

Mononucleotide substrate specificity

In contrast to bacteria NaMNAT (EC 2.7.1.18), which prefers NaMN over NMN (Gazzaniga *et al.*, 2009), the human NMNAT (hNMNAT EC 2.7.1.1) exhibits equal dual substrates recognition towards both mononucleotides hence, can flexibly participate in both pathways leading to the synthesis of NAD^+. The diverse substrate specificities exhibited by Na/NMNAT are mediated by the carboxyl group and carboxamide group of the nicotinate and nicotinamide substrates. In bacteria *Ec*NMNAT, the positive dipole of α-helix C and the main chain amide group of Tyr85, Ala86, Leu117 create an anion-binding pocket, which is responsible for recognising the negative charge on NaMN carboxylate group. The surrounding hydrophobic residues further enhance the electrophilic nature of this pocket, thus increasing its ability to discern between a carboxamide (NMN) and a carboxylate (NaMN) and its reason for a higher affinity towards NaMN than NMN. Conversely, the hNMNAT can recognise both NaMN and NMN readily with no need for any substantial spatial arrangement changes because of the existence of a negatively charged Asp residue (Asp173) and several conserved water molecules in the hNMNAT pyridine-binding site. This allows the enzyme to take up substrates of different electrostatic properties by changing the refined charge distributions of the binding site, thus making hNMNAT less rigid in stabilising different NMN/NaMN metabolic changes for NAD^+ synthesis (Zhang *et al.*, 2002; Zhou *et al.*, 2002).

Sequence conservation and secondary structure

As revealed from the crystallographic analysis on recombinant hNMNAT (Figure 2.7), the distinguished complex structures possess a disordered region encompassing a nuclear localisation signal (NLS) sequence PGRKRKW and two phosphorylation site serine residues (Ser109 and Ser136) which interacts with the nuclear-transporting proteins. However, the sequence complementary to this region is absent in bacterial NaMNAT (Schweiger *et al.*, 2001; Zhou *et al.*, 2002). Furthermore, the monomer structure of hNMNAT exhibits a dinucleotide-binding fold consisting of a six-stranded central parallel β-sheet fringed by several helices, which are quite different from bacteria *Ec*NaMNAT that has an added αβαβ (**D′′fE′g**) section implanted at the β sheet C-terminal end summing up to seven-stranded central β-sheet instead (Figure 2.7) (Zhang *et al.*, 2002). Besides, the hNMNAT C-terminal extension has a short helix (residues 267–274) situated near the pyridine-binding site, which possibly impacts substrate recognition (Zhou *et al.*, 2002), which is also absent in the bacterial NaMNAT (Zhang *et al.*, 2002).

Oligomeric states

As revealed from previous studies, hNMNAT exists in three different isoforms based on cellular activity and tissue distribution. These isoforms exhibit different functional units. Compared to the monomeric and dimeric structures typical of the bacterial NadD NaMNAT, the hNMNAT-1 exhibits a homo-hexameric structure, hNMNAT-2 a monomeric, and hNMNAT-3 a tetrameric structure.

The variances between bacteria and human Na/NMNAT active site, subunit interfaces, and limited sequence identity suggest that highly selective inhibitors may be found or designed (Zhang *et al.*, 2002; Zhou *et al.*, 2002).

2.2.6 Variation in metal ion specificity amongst NaMNAT

Thus far, all Na/NMNATs characterised are known to be metal-activated enzymes, requiring the presence of divalent cations for catalysis of the adenylyl transfer reaction. These divalent metals are essential for substrate binding and orientation of nucleotides as well as assist in catalysis. Aside from the physiologically relevant Mg^{2+}, different divalent metals like Ca^{2+}, Zn^{2+}, and Mn^{2+} are reported to function in phosphoryl transfer and substrate binding but not necessarily efficient at substrate turnover or product release (Knape *et al.*, 2015). This is largely due to the formation of a highly stable enzyme:product complex, which is tightly bound hence hampering product release.

Many studies have established Na/NMNAT isozyme to have a distinctive preference for varied divalent metal ions. For instance, the *E. coli* NMNAT (NadR) shows a higher preference for Ni^{2+} and Co^{2+} (Raffaelli *et al.*, 1999), hNMNAT1 prefers Zn^{2+} and Ni^{2+} compared to Mg^{2+} (Di Stefano *et al.*, 2010), whereas hNMNAT2 and hNMNAT3 attain optimal activity with Mg^{2+} (Raffaelli *et al.*, 2002; Sorci *et al.*, 2007). Similar to hNMNAT1, yeast NMNAT (yNaMNAT1) displayed maximal activity with Ni^{2+} (Emanuelli *et al.*, 1999), while yNMNAT2 prefers Co^{2+} (Emanuelli *et al.*, 2003).

2.2.7 Studies suggesting inhibition of NaMNAT

It is hypothesised that by suppressing the activity of NaMNAT in the cell, the production of NAD^+ will be disrupted, hence resulting in cell death. Rodionova *et. al* (2014) confirmed this in *Mycobacterium smegmatis* model system using a protein knockdown approach to induce the deprivation of target enzyme NaMNAT, which consequently displayed a strong bactericidal effect with changes in the levels of NaMN and eventual depletion of NAD(H) pool. The depleting effect was more pronounced in vital pathways such as Kreb cycle,

cholesterol catabolism, fatty acid, and aromatic compounds synthesis that depend so much on NAD(P) redox reaction. The metabolic activities were suppressed, consequently affecting the production of ATP energy (Rodionova *et al.*, 2014). The expectation is that inhibitors that would be designed against the NaMNAT enzyme must be able to deplete the NAD^+ pool and result in the entire collapse of the central metabolic system, consequently inhibiting bacterial growth (Sorci *et al.*, 2009; Sorci *et al.*, 2013).

2.3 The Role and Interaction of Divalent Metal Ions in Enzyme Activity

Metal ions serve many functions in proteins, including structural stability enhancement of the proteins in the active conformation required for biological function, modification of protein structures, and regulation or catalytic processes of enzymes. Enzymes affected by metal ions are classified as either metalloenzymes or metal-enzyme complexes. The metalloenzymes exhibit high-affinity interactions with metal ions which are not lost when isolated. In contrast, metal-enzyme complexes are loosely associated with metal ions, hence exhibit lower-affinity interactions, which are easily lost during isolation (Vallee, 1955).

Divalent metal ions interact with protein through various modes, including metal-ligand and enzyme-bridge complexes, and can serve as Lewis acids, structural regulators, electron donors or acceptors (Riordan, 1977). Figure 2.8 illustrates the different types of interaction of metal ions with enzymes. Typically, in metal activated enzymes, metal ions interact with the substrate forming a substrate-metal complex that functions as the actual substrate. This complex is formed either prior to or alongside the formation of the enzyme-substrate complex. In some instances, as observed for most metalloenzymes, the metal binds first to the protein, where it functions as a site of contact with the substrate. In which case, the metal can function either as a binding site, as a part of the enzyme catalytic system or both. Metal ions also interact with enzyme by acting at a site distant from the active site, where it induces structural rearrangement. In such cases, the metal could either serve to maintain the enzyme's structure while indirectly influencing catalytic activity or regulating activity by stabilising the enzyme's active conformations (Riordan, 1977).

1) $M + S = MS$
$E + MS = EMS$

2) $E + M = EM$
$EM + S = EMS$

3) $E + M = ME$
$ME + S = MES$

Figure 2.8. The interaction between metal ions (M), enzyme (E), and substrate (S).
(1) metal ion forming a substrate-metal complex that acts as the true substrate, (2) metal ion binding first to the enzyme serving as a site of interaction for substrate and (3) Metal ion interacting with enzyme at a distant site, away from the active site (Riordan, 1977).

During enzymatic catalysis, metals can participate in redox (30%) and non-redox reaction (70%). In the former, metal ions are involved directly in electron transfer process and undergoes a cyclic transformation in oxidation state; whereas in the non-redox catalysis, metals serve as a Lewis acid where it attracts electrons by interacting with electronegative donors from the ligand to increase the polarity of reactive chemical bonds, consequently increasing its electrophilic character and promoting the transfer of atoms or groups (Riordan, 1977).

2.4 Effect of Magnesium Ion on the Structural Integrity of ATP-Binding Proteins

The presence of divalent cations such as Mg^{2+} is crucial for activity in ATP binding proteins, as they participate in co-substrate binding and orientation of nucleotides as well as assist in catalysis. Though the metal is not a component of the enzyme active site, its presence is employed for catalysis. During enzymatic catalysis, Mg^{2+} binds ATP substrate to form ATP-Mg^{2+} complex, which is the activated form of the substrate required by the ATP binding enzymes (Riordan, 1977). The formation of ATP-Mg^{2+} complex enhances the binding energy, consequently enhancing the specificity of the enzyme-substrate interactions. This is possible through the counteraction of some negative charges present on the phosphoryl group of ATP by Mg^{2+}, thereby limiting nonspecific ionic interactions between the enzyme and the phosphoryl group of ATP. Also, the interactions between the Mg^{2+} and the oxygen atoms of

the phosphoryl group holds the nucleotide in well-defined conformations that the enzyme can specifically bind (Figure 2.9)(Jeremy M Berg, 2002).

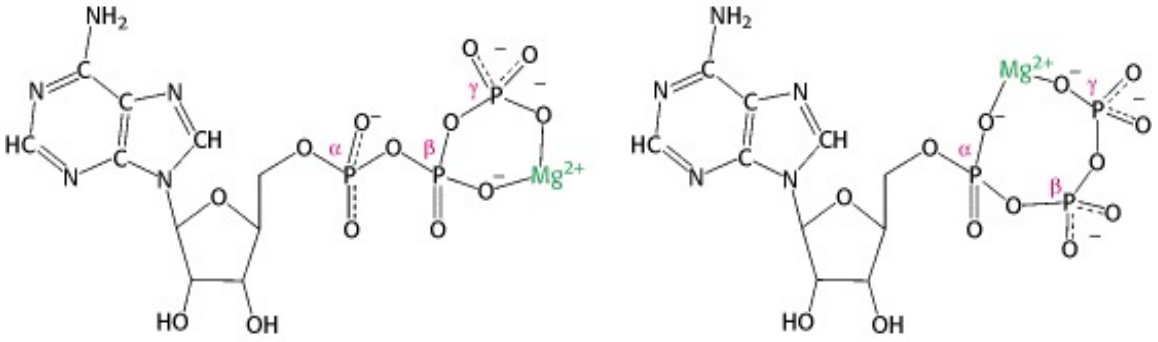

Figure 2.9. Structure depicting the different isomeric forms of the ATP-Mg^{2+} complex.
Depending on the particular enzyme, Mg^{2+} can directly coordinate with any of the two oxygen atoms of the phosphate group to allow for enzyme binding (Jeremy M Berg, 2002).

Furthermore, Mg^{2+} increases the binding energy between the enzyme and the ATP-Mg^{2+} complex by facilitating additional contact points. In certain enzymes such as DNA polymerases, Mg^{2+} bind directly to the side chains (glutamate and aspartate residues) of the enzyme. Some other enzymes, such as the adenylate kinases, interact with the Mg^{2+} indirectly via hydrogen bonds to the coordinated water molecules (Figure 2.10) (Jeremy M Berg, 2002). The presence of glycine and other positive charge residues such as lysine, arginine and histidine are also important for the interaction with ATP (Chauhan *et al.*, 2009).

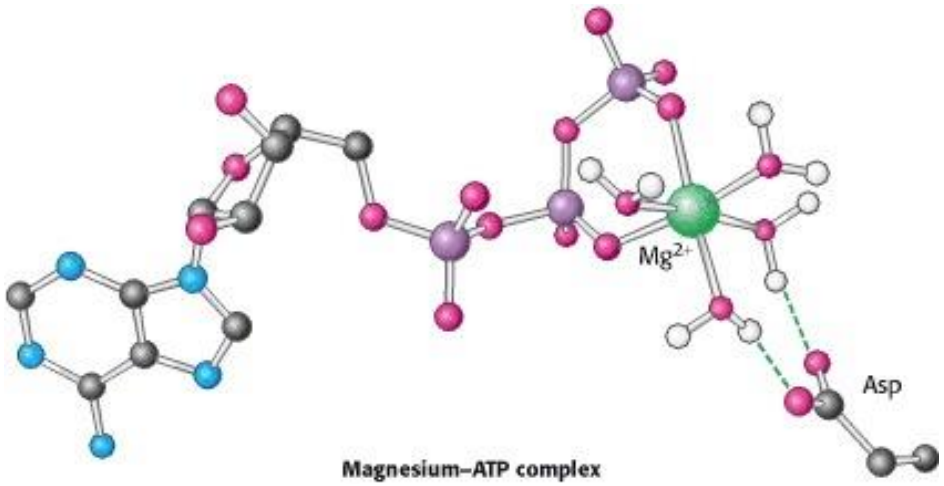

Figure 2.10. The interaction of adenylate kinase with ATP-Mg^{2+} complex.
The Mg^{2+} is coordinated to the β and γ phosphate groups, while the remaining coordination positions are bound to four water molecules that interact with the aspartate residue on the enzyme (Jeremy M Berg, 2002).

In NaMNAT enzyme, Mg^{2+} is presumed to polarise the active site, thereby facilitating the nucleophilic attack on the α- phosphorous of ATP. The destabilisation of the ester bond between the α- and β-phosphate of ATP displaces the adenyl group, which is transferred to NMN (Lowe and Tansley, 1983).

2.5 Computational Modelling

Computational modelling involves the simulation and studying of complex systems using computers. It is a theoretical aspect of science that combines mathematics, physics, and computer science, and it is demonstrating to be an extremely useful complement to experimental investigations. Over the years, different sophisticated applications and techniques have been developed to simulate to near reality, as well as explore the molecular recognition and the dynamics of biomolecular events between a ligand and a receptor site (Bras *et al.*, 2015). These techniques employ a range of physical methodologies, including classical molecular mechanics (MM) and quantum mechanics (QM). Because of the predictive power of computational biochemistry in providing insight and information about certain data that are sometimes inaccessible from experiment, the integration of computational modelling with empirical studies has been embraced to augment experimental data and provide further elucidation of biological processes at the atomic level, which can be extrapolated for rational drug design (Hung and Chen, 2014).

In this study, computational approaches comprising homology modelling, molecular docking, and molecular dynamic simulation were utilised in evaluating and analysing the molecular interactions and ligand bioactivity between the NaMNAT proteins (*Kp*NaMNAT and *Ef*NaMNAT) and ATP, NMN, and NAD^+.

2.5.1 Homology modelling

To computationally analyse or calculate protein-ligand interactions, it is essential to have the structure of the protein of interest at hand. Due to the limitation in the availability of experimental three-dimensional (3-D) crystal structures of proteins, computational modelling has become another route of predicting or deriving unavailable protein structures (Kopp and Schwede, 2004). This is possible through homology modelling, which utilises the amino acid sequence of the target protein and an experimentally determined crystal structure of a related homologous protein as a model to construct a 3-D structure of the protein. The precision at which homology modelling predicts the 3-D structures of proteins is equivalent to what can be

obtained experimentally. For a specific protein structure to be built, a library of experimentally determined protein structures is probed to select appropriate templates. This template selection is dependent on the similarities in the structure and sequence alignment as the query sequence. Hence, the quality of a homology model is dependent on the quality of the sequence alignment and the template structure in use. The higher the sequence identity, the higher the model quality, and as the sequence identity declines, so the quality of the model decreases (Chung and Subbiah, 1996). Homology modelling is applicable for purposes like protein-ligand interaction and drug design predictions which require atomic-resolution data. Since *Kp*NaMNAT and *Ef*NaMAT are novel proteins whose crystal structures are yet to be determined, a 3-D model of the proteins was built by utilising homology modelling. Further analyses were conducted by molecular docking and molecular dynamic simulation.

2.5.2 Molecular docking

Molecular docking studies the fitting together of two or more molecular structures. It involves the *in-silicon* process of simulating ligands' binding, including substrates, drugs, or inhibitors, into the active site of macromolecules such as protein or nucleic acid to predict how the small molecules will interact with the macromolecule *in vivo*. The primary aim of molecular docking is to find the correct positions of ligands in the protein binding pocket and to envisage the affinity between the ligand and the protein (Morris and Lim-Wilby, 2008). These are achieved through two basic docking processes, sampling and scoring. Sampling generates all probable positions, orientations, and conformations of the ligand within the protein sites. The scoring function aids in accurately determining the most energetically advantageous binding pose and classifies it in ranking order (McConkey *et al.*, 2002). Though the available docking programs operate slightly differently, these two basic docking processes are the essential composite of a molecular docking program (Phillips *et al.*, 2018).

The information obtained from the examination of the interactions of a given ligand and the binding sites via molecular docking allows for the characterisation of the behaviour of the ligand in the receptor of target proteins as well as expound on the fundamental biochemical processes (McConkey *et al.*, 2002) consequently, providing insight for the design of novel ligands. As against the earliest reported docking method of the lock and key mechanism, the induced-fit mechanism was utilised in this study to estimate the dynamic level of interaction shown between the nucleotide ligands ATP, NMN, and NAD^+ and *Kp*NaMNAT protein receptor.

2.5.3 Molecular dynamic (MD) simulation

MD simulation is a computational method utilised to mimic complex molecular systems at an atomic level and compute the motions of atoms present in the actual environment of individual molecules. It analyses the physical movements and fluctuations of atoms and molecules over a set timeframe while the dynamic evolution of the system is sighted. The application of MD simulation enables the sampling of the conformational space of protein molecules as well as the determination of the kinetic and thermodynamic properties, thus providing a connection between structure and dynamics, as well as an understanding of the structural and mechanistic properties of the protein molecule (Karplus and McCammon, 2002). A combination of the forces with the energy of all particles within the system must be calculated (Pounds, 2004) in order to set an MD system for simulation. MD utilises molecular mechanics force fields to estimate the potential energies and forces of a system of interacting particles by numerically solving the classical Newtonian equations of motion so as to determine the trajectories of atoms and molecules in and around the system. The interaction between the atoms is mathematically expressed as:

bonded non-bonded

$$\boldsymbol{E}_{\text{total}} = \overbrace{\boldsymbol{E}_{\boldsymbol{stretching}} + \boldsymbol{E}_{\boldsymbol{bending}} + \boldsymbol{E}_{\boldsymbol{torsional}} + \boldsymbol{E}_{\boldsymbol{cross-terms}}} + \overbrace{\boldsymbol{E}_{\boldsymbol{coulombic}} + \boldsymbol{E}_{\boldsymbol{vdw}}}$$

(Bras et al.*, 2015).*

The force field function comprises of both bonded and non-bonded interaction terms. The Bonded interactions include bonds stretching, valence angle bending, sometimes torsional dihedral angles (soft terms) and improper dihedrals (hard terms). In contrast, electrostatic (Coulomb) and Van der Waals (vdw) interactions add to nonbonded interactions (Guvench and MacKerell, 2008).

Diverse force field models have been designed with varying parameters. However, the choice of force field implemented depends on the conditions and nature of the studied system. The widely used molecular force fields for biomolecular simulations include AMBER (Cornell *et al.*, 1995; Kollman, 1996; Duan *et al.*, 2003), CHARMM (MacKerell *et al.*, 1998), OPLS-AA (Jorgensen *et al.*, 1996), GROMOS (Oostenbrink *et al.*, 2004) and NAMD (Phillips *et al.*, 2005).

The MD simulations of proteins require many steps. These include energy minimisation, solvation, system heating, equilibration, and production phase (Figure 2.11). Since the simulation of proteins is performed to repeat the experimental conditions, some parameters like pressure and temperature are considered for the different physical conditions. Generally, simulation of proteins is performed in an isothermal-isobaric (NPT) ensemble or canonical ensemble (NVT). These are solvated with explicit solvent and kept in a unit cell. An array of explicit water models are obtainable such as TIP5P (Mahoney and Jorgensen, 2000), SPC, and SPC/E (Berendsen *et al.*, 1987), TIP3P, TIP4P (Jorgensen *et al.*, 1983).

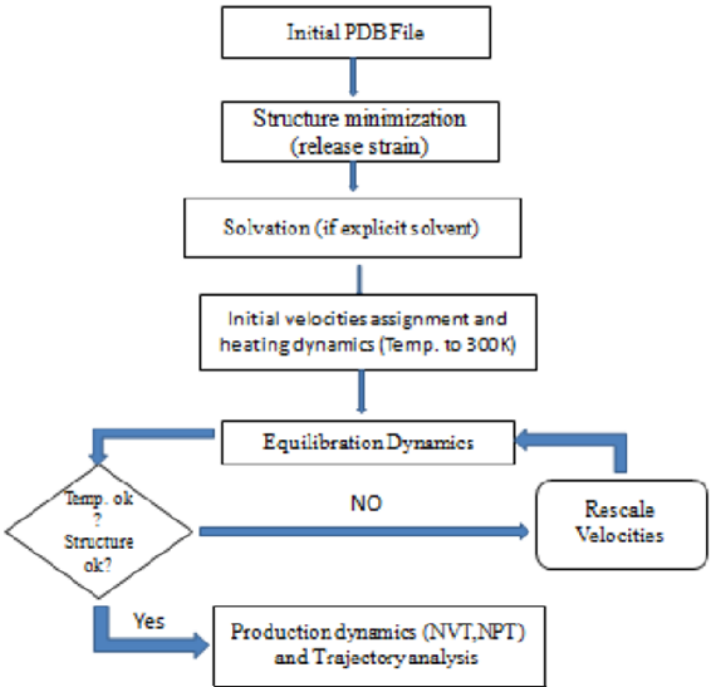

Figure 2.11. Diagrammatic representation of the stages involved in MD simulation of a protein.(Sachin Patodia, 2014)

Upon routine completion of MD simulation, trajectories generated from the production phase of the simulation run are analysed and visualised to investigate motions and conformational fluctuations at an atomic level using visualisation software which can reveal the structural parameters in a time-dependent way. Parameters that are normally evaluated include time average structure, the total energy of a system, Root mean square deviation (RMSD) difference between two structures, Root mean square fluctuation (RMSF), Radius of Gyration and interface related terms such as order parameter, electrostatic potential, and density of groups. In this study, the OPLS force field and TIP3 explicit solvent model were employed for the parameterisation and the solvation of the *Kp*NaMNAT-ligand complex systems.

Chapter 3

EXPRESSION AND PURIFICATION OF RECOMBINANT *Kp*NaMNAT AND *Ef*NaMNAT

3.1 Introduction

The recombinant *Kp*NaMNAT (B5XZR5) used for this experiment is made up of 235 amino acids (inclusive of the extra N- terminal tag). Its molecular weight is predicted as ~27 kDa, and the theoretical isoelectric point (pI) is 5.82 using ProtParam ExPASY tool. The recombinant *Ef*NaMNAT (A0A133MWI0) comprises 223 amino acids (inclusive of the extra N- terminal tag), with a predicted molecular weight of ~26 kDa and a theoretical pI of 5.79 (ProtParam ExPASY).

This chapter focuses on the basic biochemical and molecular biology procedures employed in expressing, purifying, and assessing the recombinant *Kp*NaMNAT and *Ef*NaMNAT as well as the outcome of these techniques.

Details of the buffer and reagent preparations are described in Appendix A.

3.2 Materials

Expression vectors pET-11a and pET-28a were obtained from Novagen (Damstadt, Germany). Glycerol stock of JM109 cells and competent T7 cells were used. Agar was purchased from Merck Biosciences. Tryptone, yeast extract, NaCl, ampicillin, Kanamycin, isopropyl-β-thiogalactopyranoside (IPTG), Sepharose, $NiSo_4$, Tween-20, bromophenol blue, BLUeye Prestained molecular weight marker (Catalog # 94964), N,N,N′,N′-tetramethylethylenediamine (TEMED), bisacrylamide, acrylamide, sodium dodecyl sulfate (SDS), β-mercarptoethanol, glycine, Coomassie Brilliant Blue G-250, Coomassie Brilliant Blue R-250, and glacial acetic acid were obtained from Sigma-Aldrich. Snakeskin™ dialysis tubing (10K MWCO, 22 mm) was purchased from *Thermo scientifi*c (South Africa). Other biochemicals and reagents used were procured from Sigma and of analytical grade.

The preparation of buffers and reagents are described in Appendix A.

3.3 Methods

3.3.1 Vector construct

The engineered vectors used for expressing the recombinant *Kp*NaMNAT and *Ef*NaMNAT proteins in *E. coli* T7 cells were pET-28a and pET-11a, respectively. The gene fragment encoding for *Kp*NaMNAT was inserted into pET-28a at the NcoI and BamHI site resulting in a sequence with hexahistidine and a thrombin cleavage site (Figure 3.1). For *Ef*NaMNAT, hexahistidine was incorporated into the N-terminus of the gene sequence for the purpose of using IMAC, thus resulting in a sequence with an uncleavable hexahistidine tag. Insertion of the sequence into pET-11a was at the NdeI and BamHI sites (Figure 3.2). The vectors also contained an origin of replication which allows for replication in the host cell, a gene that confers resistance to antibiotics ampicillin (pET-28a) and kanamycin (pET-11a) (allowing for selection of cells containing target vector), and a multiple cloning site for restriction enzymes to cut and insert the target gene fragment, consequently allowing the expression of the NaMNAT proteins (Appendix S2).

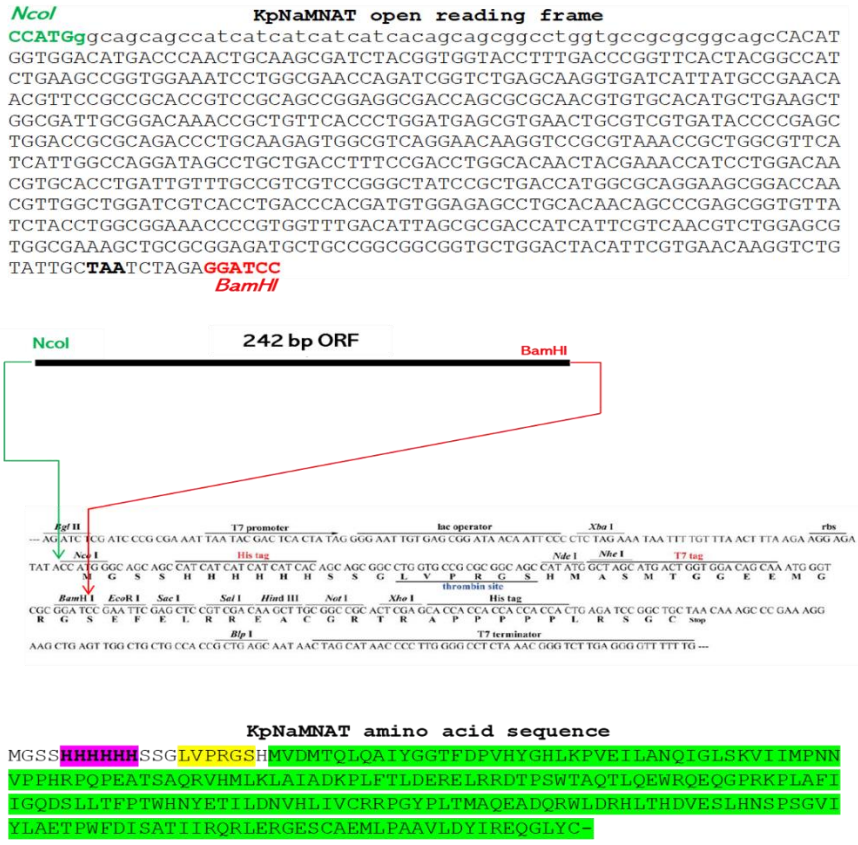

Figure 3.1. Picture depicting the constructed vector used for expressing recombinant *Kp*NaMNAT.
The gene fragment encoding for *Kp*NaMNAT was inserted into pET-28a at the NcoI and BamHI sites resulting in a *Kp*NaMNAT sequence with a hexahistidine as indicated in purple and a thrombin cleavage site indicated in yellow.

Figure 3.2. Picture depicting the constructed vector used for expressing the recombinant *Ef*NaMNAT. Hexahistidine was factored into the N-terminus of the gene sequence, as shown in purple. The resulting sequence was inserted into pET-11a at the NdeI and BamHI sites.

3.3.2 Transformation of competent *E. coli* T7 cells

Competent *E. coli* T7 host cell was transformed with the aid of heat shock to increase membrane permeability and enable the uptake of the constructed vector pET-11a-*Ef*NaMNAT and pET-28a-*Kp*NaMNAT, respectively, through the cell membrane (Cohen *et al.*, 1972). Lyophilised pET-11a-*Ef*NaMNAT and pET-28a-*Kp*NaMNAT were rehydrated with 100 µL ddH_2O to a final concentration of 40 ng/µL and centrifuged (12 000 × *g*, ~30 sec). The vector (200 ng) was added directly to the already thawed competent cells and mixed by gently flicking. The transformation mix was incubated on ice for 30 min, followed by heat shock (42 °C, 45 sec). The cells were immediately incubated on ice for 2 min, after which 900 µL of SOC media was added and incubated (37 °C, 250 rpm, 60 min). The cells were plated on LB-agar plates containing either 50 µg/mL ampicillin and 35 µg/mL chloramphenicol for pET-11a-

*Ef*NaMNAT transformation mix or 30 μg/mL kanamycin, and 35 μg/mL chloramphenicol for pET-28a- *Kp*NaMNAT transformation mix and after that, the plates were incubated (37 °C, 16-24 h).

3.3.3 Over-expression of recombinant *Kp*NaMNAT and *Ef*NaMNAT

Upon successful transformation, single colonies containing T7-pET-11a-*Ef*NaMNAT or T7-pET-28a-*Kp*NaMNAT from the LB-agar containing the selective antibiotics were picked and inoculated into 20 mL 2xYT media supplemented with appropriate antibiotics (50 μg/mL ampicillin for T7-pET-11a-*Ef*NaMNAT and 30 μg/mL kanamycin for T7-pET-28a-*Kp*NaMNAT). The culture was then incubated (37 °C, 250 rpm, 12-16 h). The overnight culture was diluted in 1:50 freshly prepared 2xYT media containing appropriate antibiotics as earlier stated and incubated (37 °C, 250 rpm) until OD_{600} ~0.6. The culture was incubated on ice for about 10-15 min, after which overexpression of target proteins was induced using 0.5 mM IPTG. The target proteins were overexpressed by incubating the cell culture (30 °C, 200 rpm, 6 h). Cells were finally harvested by centrifugation (4 °C, 5000 × *g*, 10 min). The supernatant containing media was discarded, and the pellet was suspended in 25 mL resuspension buffer (Appendix A) per litre of culture, followed by freezing (-20 °C, 20 h) to facilitate cell lysis. Frozen cells were thawed and then subjected to sonication on ice using QSonica Q55 sonicator at an amplitude of ~50-70 μm per cycle. The lysate was centrifuged (4 °C, 18000 × *g*, 15 min) to separate the soluble fraction from the insoluble. Extracts from the lysate, soluble (supernatant), and insoluble (pellet) fractions were analysed on 12.5% (w/v) sodium dodecyl sulphate polyacrylamide gel electrophoresis (SDS-PAGE) for expression of recombinant proteins (section 3.3.5).

3.3.4 Purification of recombinant *Kp*NaMNAT and *Ef*NaMNAT

This was performed using nickel ion-immobilized metal affinity chromatography (Ni^{2+}-IMAC), a method used to purify proteins with intrinsic affinity for divalent metal cations (Porath, 1992). Due to the high affinity that histidine has for transition metals, this technique was adopted to purify the target proteins containing N-terminus hexahistidine tag. Solubilised cell fraction containing the target proteins (*Ef*NaMNAT and *Kp*NaMNAT) was subjected to Ni^{2+}-IMAC using low pressure and gravity pump (Bio-Rad Model EP-1 Econo™). Approximately 9.5 mL of Sepharose resin was added to the column and washed with a 10 column volume of ~100 mL ddH_2O to remove the ethanol used to preserve the resin. The matrix was charged with Ni^{2+} by passing 0.1 M $NiSO_4$ through gravity and then washed with

ddH_2O. After that, the Ni^{2+}-resin was pre-equilibrated with 30 column volumes of equilibration buffer at a 4 mL/min flow rate. The solubilised cell fraction was loaded onto the column at a flow rate of 2 mL/min, and the unbound fraction was collected as flow through. This was followed by equilibration, washing, and equilibration using 20, 30, and 20 column volume of respective buffers (Appendix A) at 4 mL/min to remove any unbound and non-specifically bound proteins from the column. The bound hexahistidine-tagged protein was eluted with an elution buffer containing 350 mM imidazole at 2 mL/min flow rate, which competitively displaced the his-tagged protein bound to Ni^{2+} in the column and then collected in the elution fraction. Eluted fractions containing the recombinant proteins were stored on the ice for further analysis.

3.3.5 Qualitative and quantitative assessment of recombinant *Kp*NaMNAT and *Ef*NaMNAT

Sodium dodecyl sulphate polyacrylamide gel electrophoresis (SDS-PAGE)

Overexpression of the recombinant proteins and the quality of the purified proteins were analysed using discontinuous SDS-PAGE (Laemmli, 1970). The expression profile was prepared as follows; 1 mL of resuspended cells from expression were sonicated, 50 µL of lysate was reserved for SDS-PAGE, while the remaining was centrifuged. The lysate, supernatant, and pellet were respectively diluted with reducing sample buffer in a ratio of 1:1. The Pellet sample was further subjected to sonication for about 20-30 sec for easy loading on the gel. The purification profile was prepared by collecting the flow-through, wash, and elution fractions and subsequently diluted with the reducing sample buffer in a ratio of 1:1. All samples were incubated (100 °C, 5 min) to further denature the protein. Samples were afterwards loaded on the SDS-PAGE (prepared according to Table 3.1), and electrophoresis was performed at 140 V until the dye front was about 0.5 cm from the end of the gel. Coomassie blue dye solution (Appendix A) was used to stain the gel and afterwards destained to display the protein band patterns. The molecular weight of the protein band was estimated by plotting a graph of Log molecular weight of standard markers against the relative distance migrated (Rf) on the running gel.

Table 3.1. Recipe for preparing 12.5% (w/v) Separating and 4% (w/v) stacking gels.

Reagent	4% (w/v) Separating Gel	12.5% (w/v) Stacking Gel
Monomer solution	6.25 mL	940 µL
1.5 M Tris (pH 8.8)	3.75 mL	0
0.5 M Tris (pH 6.8)	0	1.75 mL
Distilled Water	4.75 mL	4.30 mL
10% (w/v) SDS	150 µL	70 µL
TEMED (N,N,N′,N′-Tetramethylethylenediamine)	15 µL	15 µL
10% (w/v) Ammonium Persulfate	75 µL	35 µL

Ultraviolet-visible (UV-vis) spectroscopy

A further assessment of the quality and the quantity of the recombinant proteins was conducted using UV-vis spectroscopy. This procedure analyses protein based on the amount of light absorbed by the sample. Since *Kp*NaMNAT and *Ef*NaMNAT contain tryptophan and tyrosine residues, absorption will be exhibited maximally at 280 nm.

Briefly, eluted fractions containing the target proteins were dialysed in two changes against dialysis buffer 1 (Appendix A) at 4 °C for 3 and16 h respectively, using a 10 kDa molecular weight cut-off (MWCO) dialysis tubing to remove salts. In a 1 mL reaction volume, 50 µL of the dialysed protein sample was diluted in 950 µL of the dialysate (1/20 dilution) and measured on the UV- vis Spectrophotometer (*Jasco V-630*). Absorbance was monitored between 240 nm and 350 nm at 20 °C using a 100 mm micro-QS quartz absorbance cuvette. Three UV spectra were collected (200 nm/min scanning speed, 1.5 nm bandwidth, 1.0 nm data interval). The spectra were automatically averaged and then corrected by subtracting the baseline (corresponding to the buffer) from the data.

The concentration of the purified recombinant proteins was estimated spectrophotometrically by measuring absorbance at 280 nm and 340 nm (Penzkofer *et al.*, 2007), in conjunction with Beer-Lambert law,

$$A = \varepsilon cl$$

Where A = absorbance (arbitrary unit)

ε = molar extinction coefficient at 280 nm (*Ef*NaMNAT = 30370 $M^{-1}cm^{-1}$ and *Kp*NaMNAT = 37930 $M^{-1}cm^{-1}$, obtained theoretically using ProtParam ExPASY.)

c = concentration in Molar

l = path length in cm

A plot of corrected absorbance ($A_{340–280\ nm}$) against dilution was generated, and the slope was used to deduce the concentration of the purified recombinant proteins.

3.4 Results

Over-expression

SDS-PAGE showed that overexpression of recombinant *Kp*NaMNAT and *Ef*NaMNAT was induced using 0.5 mM and 1.0 mM IPTG. This was evident by the presence of a prominent band corresponding to the theoretical molecular weight deduced for *Kp*NaMNAT (~27 kDa) and *Ef*NaMNAT (~26 kDa) sequences (Figure 3.3). In contrast, no such visible band was detected in the absence of IPTG. A good yield of soluble protein was observed from these analysed cell lysates, as shown in Figure 3.4. The amount of wet cell pellet obtained for recombinant *Kp*NaMNAT expression was ~7.5 g/L of culture, while ~9.5 g/L was obtained for *Ef*NaMNAT.

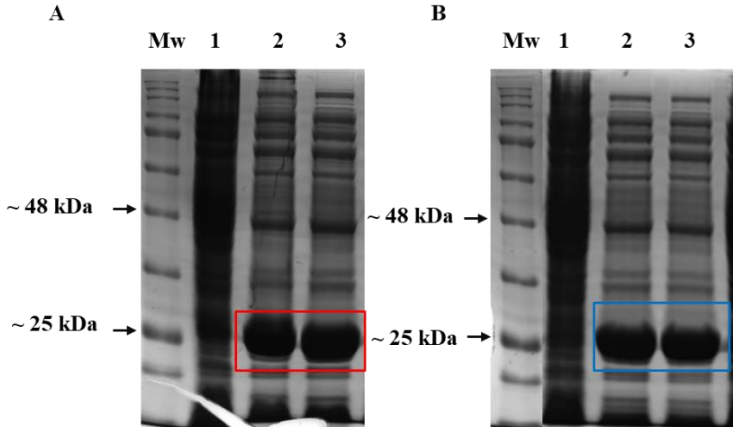

Figure 3.3. SDS-PAGE showing the overexpression of the recombinant proteins.
(A) *Kp*NaMNAT and (B) *Ef*NaMNAT at (1) 0.0 mM IPTG, (2) 0.5 mM IPTG, and (3) 1.0 mM IPTG induction. Fractions with zero IPTG showed no overexpression of the protein. However, fractions containing 0.5 mM and 1.0 mM IPTG displayed a significant amount of expressed protein as indicated in the box. The analysis was carried out on a 12.5% polyacrylamide gel containing 10% (w/v) SDS and visualised with coomassie brilliant blue staining.

Purification, qualitative and quantitative assessment

Purification of the solubilised cell fraction using Ni^{2+}-affinity chromatography proved effective in isolating the his-tagged recombinant proteins and in achieving pure proteins (Figure 3.4). Furthermore, qualitative assessment of the proteins via UV absorption spectrum monitored between 240 and 350 nm revealed a trough at 260 nm and a flat baseline at 340 nm (Figure 3.5). The protein concentration was estimated to be ~7.4 mg/mL for *Kp*NaMNAT and ~6.5 mg/mL for *Ef*NaMNAT using the gradient generated from the construct of corrected absorbance against concentration (Figure 3.6), coupled with Beer-Lambert's law, as shown in Appendix B.

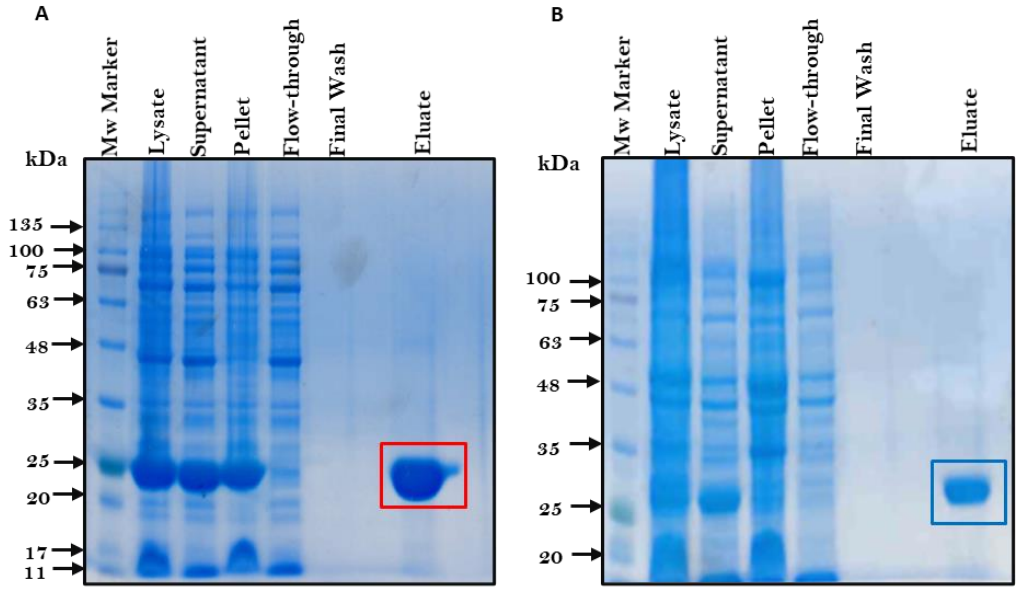

Figure 3.4. SDS-PAGE analysis of expressed and purified NaMNAT from (A) *K. pneumoniae* and (B) *E. Faecium*.
The overexpression of recombinant K*p*NaMNAT and *Ef*NaMNAT in E. coli was achieved using 0.5 mM IPTG (30 °C, 230 rpm, 6 h). Crude lysate of E. coli containing overexpressed *Kp*NaMNAT and *Ef*NaMNAT was subjected to centrifugation to separate the soluble fraction (supernatant) from the insoluble (pellet). The solubilised fraction was purified by Ni^{2+}-IMAC and eluted with 350 mM imidazole. All fractions were analysed on a 12.5% (w/v) polyacrylamide gel containing 10% (w/v) SDS and visualised with coomassie brilliant blue staining. The purified protein is indicated in the box.

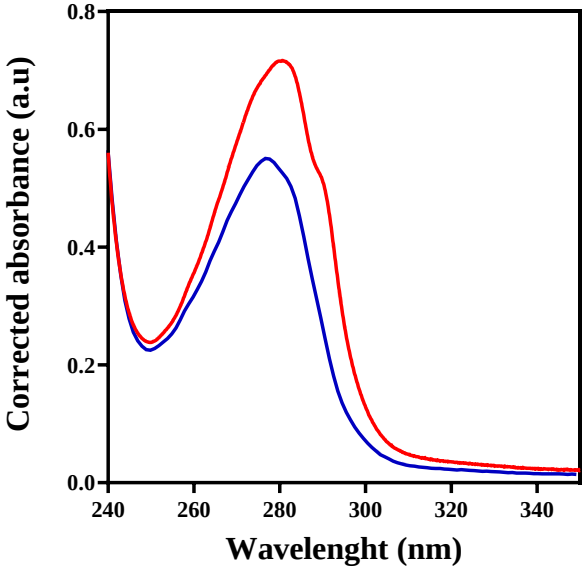

Figure 3.5. The UV absorption spectrum of *Kp*NaMNAT and *Ef*NaMNAT for Quality assessment.
The UV absorption was monitored spectrophotometrically between 240 and 350 nm wavelength using a 100 mm micro-QS Abs cuvette. Protein samples were analysed in 10 mM NaH_2PO_4, 1 mM EDTA, 0.01% (w/v) NaN_3, pH 7.2. *Kp*NaMNAT is represented by the red profile and *Ef*NaMNAT in blue. A trough at 260 nm and a flat baseline at 340 nm indicate that the proteins are free of DNA contamination and aggregation, respectively.

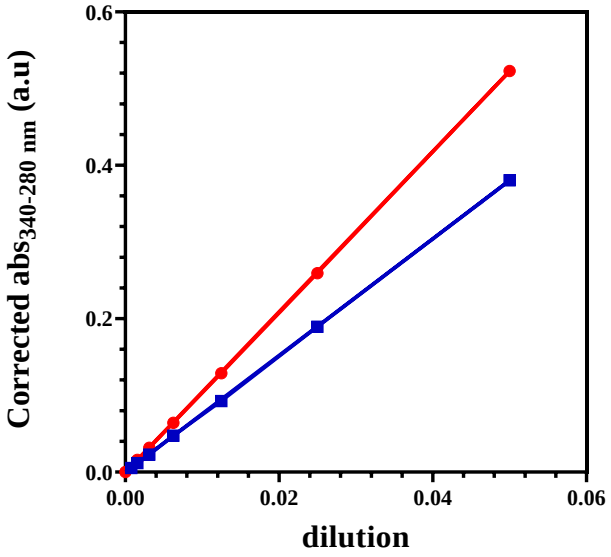

Figure 3.6. A plot of corrected absorbance versus protein dilution used to quantify recombinant *Kp*NaMNAT and *Ef*NaMNAT.
*Kp*NaMNAT profile is represented in red, and *Ef*NaMNAT in blue. 1:20-fold protein dilution was carried out in 10 mM NaH_2PO_4, 1 mM EDTA, and 0.01% (w/v) NaN_3, pH 7.2 at 20 °C and absorbance monitored spectrophotometrically at 280 nm and 340nm. The resulting slopes of the two constructed linear regression ($y = 10.46x - 0.001$) and ($y = 7.612x - 0.00007$) for *Kp*NaMNAT and *Ef*NaMNAT respectively was used in conjunction with beer lambert's law to determine their concentration as ~7.4 mg/mL and ~6.5 mg/mL respectively, $R^2 = 1$.

3.5 Discussion

The use of vector constructs pET-28a-*Kp*NaMNAT and pET-11a-*Ef*NaMNAT in *E. coli* T7 Strain, together with the expression conditions 0.5 mM IPTG, 30 °C, 230 rpm shaking, and 6 h induction time was efficacious at overexpressing the proteins. This is supported by the result obtained from the expression profile of the recombinant proteins (Figure 3.3), as the band signifying the presence of the proteins on the SDS-PAGE agrees with the theoretical molecular weight deduced for *Kp*NaMNAT and *Ef*NaMNAT sequence. Moreover, the SDS-PAGE revealed that overexpression of recombinant *Kp*NaMNAT and *Ef*NaMNAT proteins in soluble form could be achieved even on a large-scale production using T7 cells transformed with pET-hexahistidine.

One-step affinity purification using Ni^{2+}-IMAC, as indicated by the SDS gel (Figure 3.4), was equally effective. This is evident from the series of fractions obtained during the purification process (Figure 3.4, lane 5 - 7). The absence of target protein in the flow-through and wash fractions, as indicated in Figure 3.4, lanes 5 and 6, suggests the successful trapping of the N-terminal hexahistidine tagged proteins in the Ni^{2+} chelator resin column via selective coordinate covalent binding between Ni^{2+} and the imidazole ring of the poly-histidine tag. Furthermore, the appearance of one band with a molecular mass corresponding to ~27 kDa and ~26 kDa in the respective elution fraction of *Kp*NaMNAT and *Ef*NaMNAT purification profile (Figure 3.4, lanes 7) indicates successful isolation of the target proteins. Compared to the preceding fractions analysed (Figure 3.4, lane 2-6), the homogeneity of the elution fractions (Figure 3.4, lane 7) yielded more than 95% pure protein, which is free of nucleic acid contamination and aggregation. This fraction amounted to ~50 mg of purified *Kp*NaMNAT and ~42 mg of purified *Ef*NaMNAT per gram of wet cells.

The procedures employed in this chapter complete the successful expression and purification of the novel recombinant *Kp*NaMNAT and *Ef*NaMNAT. Attempt to perform an on-column cleavage of the hexahistidine tag on *Kp*NaMNAT was not effective, possibly because of the proximity between the thrombin cleavage site and the N-terminus as a result of steric hindrance. All subsequent experiments are performed with pure *Kp*NaMNAT and *Ef*NaMNAT with the histidine-tag.

Chapter 4

FUNCTIONAL CHARACTERISATION OF RECOMBINANT *Kp*NaMNAT AND *Ef*NaMNAT

4.1 Introduction

Following the successful overexpression and the one-step affinity chromatography purification of the recombinant *Kp*NaMNAT and *Ef*NaMNAT, an activity assay was carried out spectrophotometrically to confirm the functional properties of both proteins for NaMNAT activity. This was achieved using a dual enzyme catalysed reaction involving alcohol dehydrogenase (ADH) (Balducci *et al.*, 1995). The coupled enzyme assay enabled the quantification of NaMNAT activity by monitoring NADH production at 340 nm, with NMN and ATP as the initial substrate (Figure 4.1). In addition, the effect of pH on the activity of both enzymes was assessed, and because divalent metal cation is required for NaMNAT activity, the impact of different divalent cations on the activity of these enzymes at varying pH was also examined. Since NaMNATs can either utilise NaMN or NMN substrate to synthesise NAD^+, to save cost and avoid the cumbersome use of a third enzyme (NAD^+ synthase) which would be required to convert the NaAD product to NAD^+, NMN was the substrate used for this experiment.

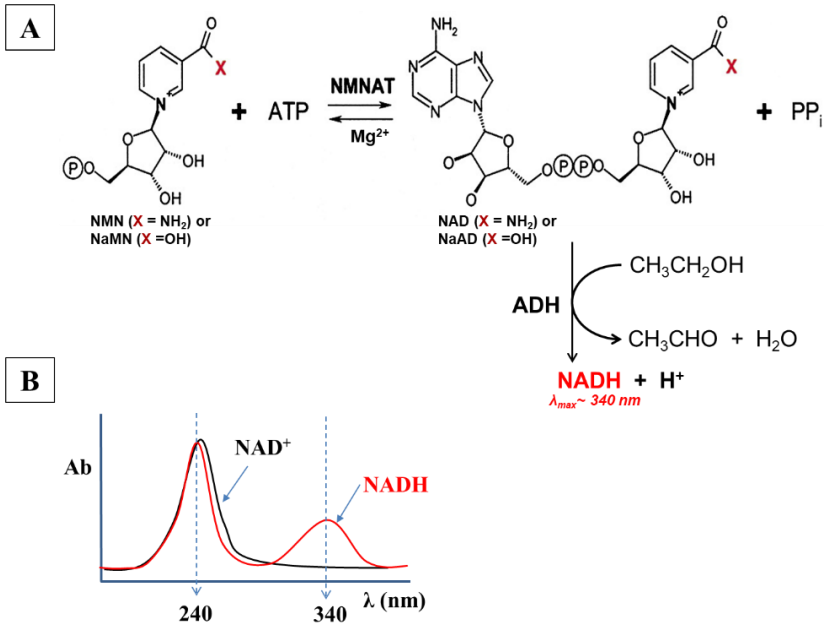

Figure 4.1. A schematic illustration of (A) the coupled enzyme reaction that involves both NaMNAT and alcohol dehydrogenase (ADH) and (B) the absorbance spectra of NAD^+ and NADH.
NaMNAT can utilise either NMN or NaMN substrates to produce NAD^+ and NaAD, respectively. The NAD^+ produced is then reduced to NADH by ADH in the presence of ethanol and monitored at 340 nm. The rate at which NADH is produced is dependent on the rate at which NaMNAT utilises the NMN substrate to produce NAD^+. The difference in the absorbance of NAD^+ and NADH enables the quantification of NaMNAT activity.

4.2 Materials

NMN, ATP, alcohol dehydrogenase (ADH) from *Saccharomyces cerevisiae* (Catalog # A7011), and DTT were purchased from Sigma-Aldrich. Other buffer components and reagents such as ethanol, sodium phosphate (NaH_2PO_4), sodium azide (NaN_3), Tris-HCl, sodium acetate, Na-glycine, magnesium chloride ($MgCl_2$), calcium chloride ($CaCl_2$), copper(II) sulphate ($CuSO_4$), nickel(II) sulphate ($NiSO_4$), zinc sulphate ($ZnSO_4$), cobalt chloride ($CoCl_2$), manganese chloride ($MgCl_2$), and iron(II) sulphate ($FeSO_4$), were from Sigma and of analytical grade.

4.3 Methods

4.3.1 Effect of pH on enzyme activity

The enzymes activity with respect to pH was determined by performing a continuous coupled assay (Balducci *et al.*, 1995) in 0.1 M sodium acetate buffer (pH 5.5), 0.1 M sodium phosphate buffer (pH 6.0–8.0), 0.1 M Tris-HCl buffer (pH 8.5–9.0), and 0.1 M sodium glycine buffer (pH 9.0–10.5). The assay was conducted using a 1 mL reaction mixture containing 1 µM of the recombinant protein, 5 mM $MgCl_2$, 1 mM ATP, 1% (v/v) ethanol, 10 U/mL ADH, 1 mM DTT, and 0.01% (w/v) NaN_3. The reaction was initiated at 20 °C by adding 0.5 mM NMN. The absorbance of NADH synthesis from the reduction of NAD^+ produced by the respective recombinant enzymes was monitored spectrophotometrically using Jasco V-630 UV-Vis spectrophotometer at 340 nm for 60 sec. The slope of the Abs/time generated for each assay was plotted against the pH. The negative control for the assay was carried out in the absence of the recombinant proteins.

4.3.2 Effect of divalent metal ion on enzyme activity

The effect of divalent cations on the activity of *Kp*NaMNAT and *Ef*NaMNAT at different pH was evaluated by preparing each 2 mM metal salts ($CaCl_2$, $CoCl_2$, $MgCl_2$, $MnCl_2$, $CuSO_4$, $FeSO_4$, $NiSO_4$, and $ZnSO_4$) in 50 mM sodium acetate (pH 5.0–6.0), and 50 mM Tris-HCl (pH 7.0–9.0). The respective 1 mL reaction mixture contained other reaction components in the same proportion as section 4.3.1 and conducted under the same condition (Balducci *et al.*, 1995). The negative control was carried out in the absence of metal. Furthermore, given that ADH is maximally active at pH 9.0, its activity was assessed in the presence and absence of the different divalent metals in 50 mM Tris-HCl, pH 9.0, as a control.

4.4 Results

The effect of pH on *Kp*NaMNAT and *Ef*NaMNAT activity, as demonstrated in Figure 4.2, revealed increasing activity in *Kp*NaMNAT with an increasing pH until optimum pH was attained at 8.0. Afterwards, a decline in the activity of the enzyme was observed until pH 10.5. In contrast, *Ef*NaMNAT only displayed a significant activity at pH 8.0.

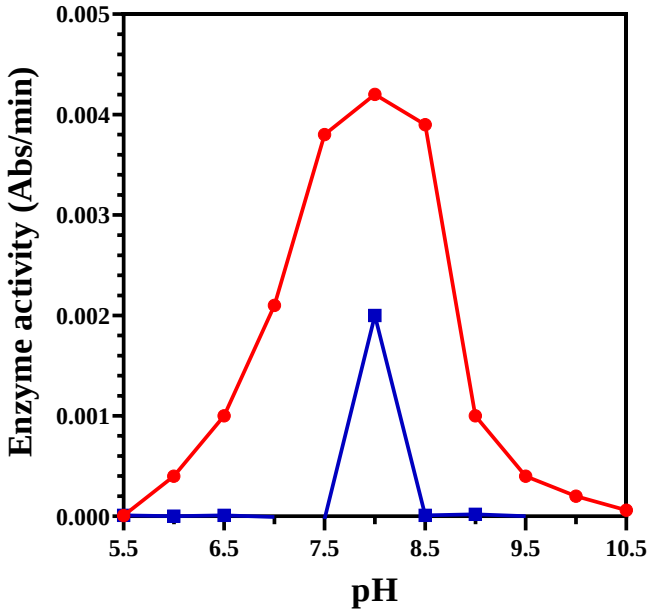

Figure 4.2. The activity profile of recombinant *Kp*NaMNAT and *Ef*NaMNAT at different pH.
The red profile represents the reaction rate for *Kp*NaMNAT, while the blue profile represents *Ef*NaMNAT. Assay was conducted in 0.1 M sodium acetate (pH 5.5), 0.1 M NaH_2PO_4 (pH 6.0–8.0), 0.1 M Tris-HCl (pH 8.5–9.0) and 0.1 M sodium glycine (pH 9.0–10.5) buffers. *Kp*NaMNAT demonstrated a broad pH optimal with maximal activity observed at pH 8.0, while *Ef*NaMNAT displayed a narrow pH optimum of 8.0.

In this study, the requirement of divalent metal ions for the catalysis of the adenylyl transfer reaction was investigated. It was found that in the absence of divalent metal cation, there was no NaMNAT activity exhibited by both recombinant enzymes. This was furthered established as ADH was active in the absence of metal ions (Figure S3 appendix B). Therefore, the effect of divalent cations Mg^{2+}, Ca^{2+}, Mn^{2+}, Cu^{2+}, Ni^{2+}, Co^{2+}, Fe^{2+}, and Zn^{2+} on the activity of the recombinant proteins were evaluated. Between pH 5.0 and 9.0, Mg^{2+} was the most effective cation with *Kp*NaMNAT, exhibiting maximal activity at pH 9.0 in 50 mM Tris-HCl (Figure 4.3A). This can be substituted to a great extent by Ni^{2+}. Zn^{2+} and Cu^{2+} supported partial activity, while Ca^{2+} repressed *Kp*NaMNAT activity (Table 4.1). *Ef*NaMNAT, on the other hand, demonstrated very low activity towards NMN in the presence of all the metals. However, maximal activity was sustained with Zn^{2+} (Figure. 4.3B) at pH 7.0. An equal activity was also

observed at pH 6.0 in the presence of Ni^{2+}. Ca^{2+} and Mg^{2+} were maximally active at pH 8.0 and 9.0, respectively. Generally, the activity displayed was minimal, so also for Cu^{2+}. The impact of Co^{2+}, Fe^{2+}, and Mn^{2+} on the enzyme's activity could not be assessed due to the formation of precipitates probably arising from the reaction of the metals with the enzyme.

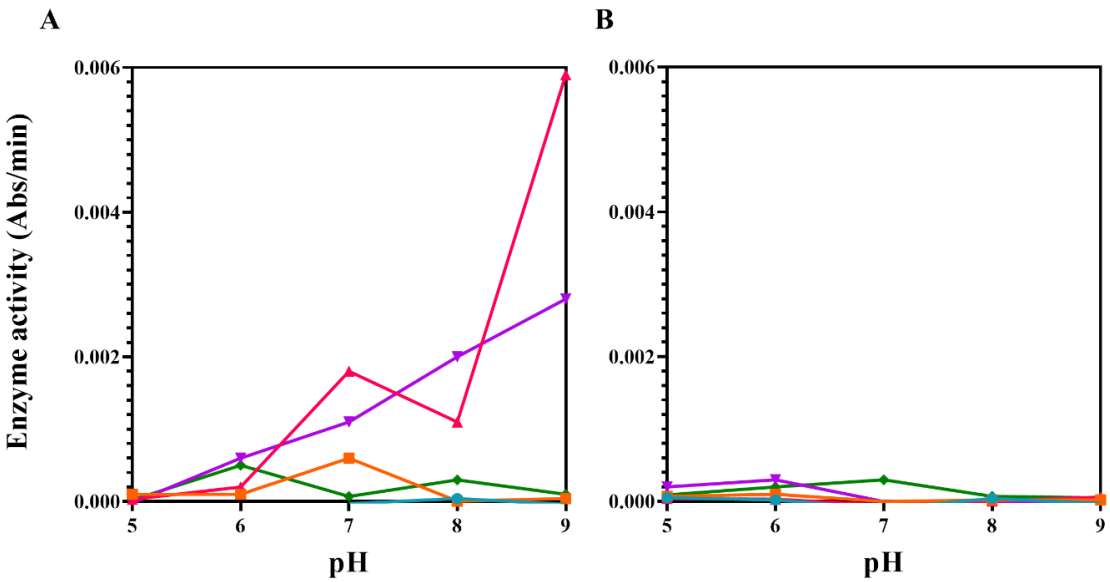

Figure 4.3. The activity profile of *Kp*NaMNAT and *Ef*NaMNAT in the presence of different divalent metal cations and at varying pH.
Analysis was carried out in 50 mM Na-acetate (pH 5.0–6.0) and 50 mM Tris-HCl (pH 7.0–9.0) spectrophotometrically using ATP and NMN as substrates. The divalent metals Mg^{2+}, Ni^{2+}, Ca^{2+}, $Cu^{2+,}$ and $Zn^{2+,}$ are represented by pink, purple, blue, brown, and green, respectively. (A) *Kp*NaMNAT in the presence of the metals displayed maximum activity with Mg^{2+} at pH 9.0, while (B) *Ef*NaMNAT showed lower activity towards NMN; however, optimal activity was recorded with Zn^{2+} at pH 7.0 and Ni^{2+} at pH 6.0.

Table 4.1. Influence of divalent cations on the activity of *Kp*NaMNAT at different pH.

Divalent Metal	Concentration (mM)	Relative Activity (%)				
		pH 5.0	pH 6.0	pH 7.0	pH 8.0	pH 9.0
None	0	0	0	0	0	0
Mg^{2+}	2	100	100	100	100	100
Cu^{2+}	2	333	50	33	1	1
Ca^{2+}	2	0	0	0	4	0
Ni^{2+}	2	0	300	61	48	47
Zn^{2+}	2	67	250	4	27	2

*Relative activity was assayed in 50 mM Na-acetate (pH 5.0–6.0) and Tris-HCl (pH 7.0–9.0) containing 1 mM ATP and 0.5 mM NMN at 20 °C. The analysis was recorded with respect to Mg^{2+} (100%).

4.5 Discussion

Insight from the functional studies conducted revealed that the recombinant *Kp*NaMNAT and *Ef*NaMNAT target proteins were able to utilise ATP and NMN as substrates to form NAD^+. This was evident given that the increase in absorbance at 340 nm arose from NADH formation by ADH, implying that the purified recombinant *Kp*NaMNAT and *Ef*NaMNAT were active and possessed NaMNAT activity. Compared to most Na/NMNAT characterised proteins (Raffaelli *et al.*, 1997; Raffaelli *et al.*, 1999; Emanuelli *et al.*, 2001; Emanuelli *et al.*, 2003), *Kp*NaMNAT showed broad pH optima between 6.5 and 9.0 when utilising NMN as a substrate. Surprisingly, *Ef*NaMNAT exhibited a narrow optimum pH and pseudo activity at pH 8.0 (Figure 4.2), which was not reproducible. These were presumed to be due to *Ef*NaMNAT having a poor affinity for the NMN substrate given that previous studies have revealed that the NadD bacterial NaMNAT exhibited a substrate preference for NaMN over NMN (Hughes *et al.*, 1983; Mehl *et al.*, 2000), as demonstrated in *E. coli* NaMNAT(NadD) (Zhang *et al.*, 2002), *S. aureus* NaMNAT (*sa*NaMNAT) (*Han et al., 2006*), and *B. subtilis* NaMNAT (bsNadD) (Olland *et al.*, 2002). Moreover, Osterman and Begley identified that most Gram-positive bacterial pathogen essentially utilises only the PncA-PncB route to salvage NAD^+ synthesis (Osterman and Begley, 2007) rather than the concomitant usage of NMN salvage route (Figure 2.3). Hence, the NaMNAT from Gram-positive may display a much lesser preference for NMN. Furthermore, given that the "H/TXGH" signature motif sequence plays a major role in recognising and binding substrate (Izard and Geerlof, 1999), the replacement of glycine residue with alanine in the sequence motif of *Ef*NaMNAT (Figure 2.6) could possibly alter the specificity or the binding affinity for NMN; hence, the poor substrate usage as observed in the reaction rate of *Ef*NaMNAT compared to *Kp*NaMNAT.

The optimum pH demonstrated by both *Kp*NaMNAT and *Ef*NaMNAT seems to vary between pH 8.0 and 9.0 (Figure 4.2 and 4.3). This variation appears to be partly influenced by changes in the ionic strength of the solution since different buffers and concentrations were utilised in the different assays. Moreover, ADH exhibited an optimal activity between pH 8.0 and 9.0 (Silverstein, 2016), and given that it controlled the formation of NADH in the assay. This could also impact the optimal pH displayed by the NaMNAT proteins.

Considering the requirement of divalent cations for NaMNAT activity (Magni *et al.*, 1999), neither *Ef*NaMNAT nor *Kp*NaMNAT was active in the absence of a divalent metal ion; however, ADH was active. This indicates the importance of divalent metal cations in the catalysis of the adenylyl group from ATP to NMN. Previous studies have demonstrated

Na/NMNATs exhibit selective preferences for varying divalent metal cations other than Mg^{2+}. Our investigation on the impact of different divalent cations on the activity of recombinant *Kp*NaMNAT and *Ef*NaMNAT (Figure 4.3) showed both enzymes to exhibit a differential requirement for Mg^{2+}. *Kp*NaMNAT attained a maximal activity in the presence of Mg^{2+} and subsequently Ni^{2+} to a substantial extent; thus, showing a similarity in metal ion preference as observed in *L. braziliensis* NMNAT (Contreras *et al.*, 2015), human (hNMNAT- 2 and 3) (Sorci *et al.*, 2007) and *S. cerevisiae* (yNMNAT-1) (Emanuelli *et al.*, 1999). On the other hand, Zn^{2+} serves as a more efficient cofactor *in vitro* to sustain *Ef*NaMNAT activity, with the reaction rate being 13 times higher than Mg^{2+} of the same concentration. This preference for Zn^{2+} by *Ef*NaMNAT is no surprise. It is in concordance with what is observed in the hNMNAT-1 (Emanuelli *et al.*, 2001) and yNMNAT-2 (Emanuelli *et al.*, 2003), reported to demonstrate a very low K_{app} value for Zn^{2+}. Moreover, the hNMNAT-1 is reported to require a higher concentration of Mg^{2+} of at least 10–15 mM to achieve maximum activity (Raffaelli *et al.*, 2002; Sorci *et al.*, 2007). Perhaps this could be another factor to the reduced activity demonstrated by *Ef*NaMNAT towards NMN, as the concentration of Mg^{2+} in the assay carried out was only 2 mM.

From the functional study conducted, it is apparent that the rate at which *Kp*NaMNAT and *Ef*NaMNAT utilise NMN substrate differs. It is also evident that both proteins have preferences for different divalent cations and exhibit a differential requirement for Mg^{2+}. Although *Ef*NaMNAT activity was not reproducible, the presence of the histidine tag is unlikely to have affected the activity of the protein, considering that *Kp*NaMNAT was active despite having a slightly longer tag. However, this does not rule out the possibility of the histidine tag interfering with the activity.

Chapter 5

LIGANDIN ACTIVITY OF RECOMBINANT *Kp*NaMNAT AND *Ef*NaMNAT

5.1 Introduction

This chapter describes the structural characterisation of *Kp*NaMNAT and *Ef*NaMNAT, the methods and techniques used in the study. The secondary structure content was determined using Far-UV circular dichroism (CD) spectropolarimetry, which measures the differences in the absorption of left-handed and right-handed circularly polarised light generated by the chromophores in the polypeptide backbone (Greenfield, 2006). The absorption disparity produces different CD spectra, which were further analysed using the analysis program-CONTIN-LL on DichroWeb online server to estimate the composition of the secondary structure elements (β-strands, α-helices, and loops) of the proteins. The tertiary structure of the proteins was then studied by means of fluorescence spectroscopy and thermal shift assay using extrinsic fluorescent dyes, 2′/3′-O-(N-Methyl-anthraniloyl)-adenosine-5′-triphosphate (mant-ATP), 8-anilino-1-naphthalenesulfonic acid (ANS), and SYPRO Orange in the absence and presence of ATP, NMN, $NAD^{+,}$ and divalent metal cations (Mg^{2+}, Ni^{2+}, Ca^{2+}, Cu^{2+}, and Zn^{2+}). The interaction of these extrinsic fluorescent dyes with the hydrophobic pockets on the protein is usually accompanied by a change in the fluorescent properties of the dyes (Gasymov and Glasgow, 2007; Niesen *et al.*, 2007). The information derived from these fluorescent changes, both in the absence and presence of ligand, was used to gain insight into the possible structural conformation, stability, and the interaction of ligands with *Kp*NaMNAT and *Ef*NaMNAT. Finally, the quaternary structure of the proteins was estimated by size-exclusion high-pressure liquid chromatography (SE-HPLC), which provides information as to the overall native size and the oligomeric state of the protein in solution.

5.2 Materials

NMN, ATP, NAD, GTP, ANS (8-anilino-1-naphthalenesulfonic acid) (Catalog # A3125), mant-ATP (2′/3′-O-(N-Methyl-anthraniloyl)-adenosine-5′-triphosphate) (Catalog # 18723), SYPRO Orange dye (Catalog # S5692), and DTT were purchased from Sigma-Aldrich, gel filtration standard molecular weight markers from Bio-Rad (Catalog # 1511901), and Snakeskin™ dialysis tubing (10K MWCO, 22 mm) was purchased from *Thermo scientifi*c (South Africa). Other biochemicals and reagents used include sodium phosphate, sodium azide,

Tris-HCl, magnesium chloride, calcium chloride, copper(II) sulphate, nickel(II) sulphate, zinc sulphate, and urea were from Sigma and of analytical grade.

5.3 Methods

5.3.1 Secondary structure content analysis

To analyses the secondary structural content of the recombinant *Kp*NaMNAT and *Ef*NaMNAT, 5 µM dialysed fraction of the proteins (section 3.3.5) were prepared in 10 mM NaH_2PO_4, pH 7.5 and subjected to far-UV CD spectroscopy using Jasco J-1500 CD spectrometer (20 °C, 1 nm bandwidth, 0.5 nm data pitch, 100 nm/min scanning speed). CD spectra were collected between 180 and 255 nm using a 1 mm path length high transparency CD quartz cuvettes under continuous nitrogen flush to remove oxygen. The conformation of the denatured proteins was also examined by treating protein samples with 8 M urea under the same conditions. For each sample, three scans were collected and automatically averaged by the system. Collected data were corrected by subtracting the baseline corresponding to the buffer from the data (Greenfield, 2006). The resulting CD spectra were processed using SigmaPlot 12.0 version (Systat Software, Inc.).

To estimate the composition of β-strands, α-helices, and loops of the proteins, the CD spectra data were deconvoluted using the analysis program- CONTIN-LL on DichroWeb online server. This software analyses CD spectra using ridge regression analysis to fit the spectrum of unknown protein by comparing it to the spectra of an extensive database of proteins that have been characterised via X-ray crystallography (Provencher and Gloeckner, 1981). Briefly, the CD spectra data generated as ASCII file from far-UV CD spectroscopy was uploaded on DichroWeb (http://dichroweb.cryst.bbk.ac.uk/html/process.shtml). Information about the data file such as input unit, wavelength range (nm), data pitch (nm), and the lowest nm data point to use in the analysis was inputted. The CONTIN analysis program, reference dataset 6, was used to analyse the data, while the output was set as theta (machine units), mdeg. Other information provided included the path length (cm), molecular weight (Daltons) and concentration of the protein (mg/mL), after which data was submitted for analysis.

5.3.2 Tertiary structure analysis

The hydrophobicity, structural conformation, stability, and interaction of *Kp*NaMNAT and *Ef*NaMNAT with ATP, NMN, NAD^+, and divalent metal cations (Mg^{2+}, Ni^{2+}, Ca^{2+}, Cu^{2+}, and Zn^{2+}) were probed by fluorescence spectroscopy using ANS and mant-ATP, and thermal

shift assay using SYPRO Orange fluorescent dye. Except otherwise stated, all measurements were performed in 10 mM NaH_2PO_4, 0.01% (w/v) NaN_3, and 1 mM DTT, pH 7.5.

Extrinsic ANS fluorescence spectroscopy

ANS binding studies were performed in the absence and presence of ATP, NMN, NAD^+, as well as Mg^{2+}, Ni^{2+}, Ca^{2+}, Cu^{2+}, and Zn^{2+}. Five samples (1 mL each) containing 50 µM ANS and 5 µM dialysed protein were prepared and supplemented with either 8 M urea, 1 mM ATP, 1 mM NMN, and 1 mM NAD. To all the samples containing nucleotide ligand, 2 mM $MgCl_2$ was added. Blanks were prepared for the respective samples by excluding 5 µM protein.

Due to complex formation of calcium and phosphate salt, Tris-HCl buffer was used to assay the divalent metal cations. 2 mM salt of $MgCl_2$, $NiSO_4$, $CaCl_2$, $ZnSO_4$, and $CuSO_4$ were each prepared in 25 mM Tris-HCl, pH 7.5. Analysis was performed using a 1 mL reaction volume containing 100 µM ANS and 20 µM protein in the respective metal salt buffers. Blanks were also prepared for the respective test samples by excluding the 20 µM protein. All samples were excited at 395 nm, with emission spectra collected over a 400–650 nm wavelength range using a 10 mm path length quartz cuvette in a Jasco FP-6300 spectrofluorometer (20 °C, 5 nm bandwidth, 1 nm data pitch, 200 nm/min scanning speed). Three emission spectra were collected per experiment, averaged and corrected for signal from free ANS and the buffer absorption. The resulting spectra were processed using SigmaPlot. Figure 5.1 shows the structure of ANS and its binding in a hydrophobic pocket.

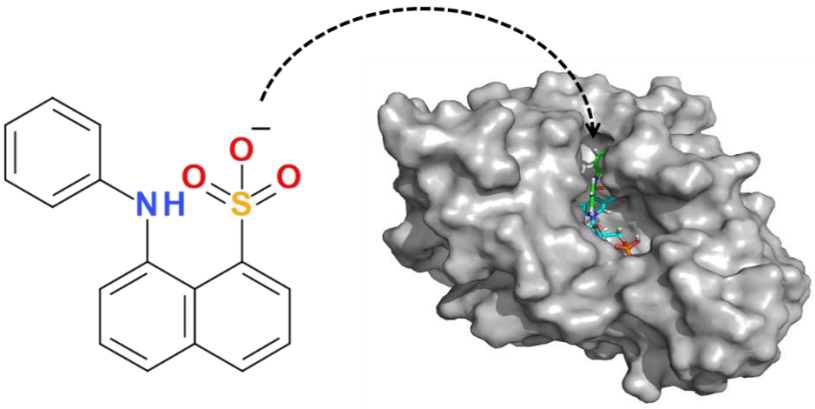

Figure 5.1. The structure of 8-Anilino-1-naphthalenesulfonic acid (ANS) and its binding in the hydrophobic pocket of *Kp*NaMNAT

Extrinsic mant-ATP fluorescence spectroscopy

Further investigation on ligand binding was performed using mant-ATP fluorescence (Figure 5.2). This study was also conducted both in the absence and in the presence of nucleotide molecules ATP, NMN, and NAD^+, as well as the divalent metal cations (Mg^{2+}, Ni^{2+}, Ca^{2+}, Cu^{2+}, and Zn^{2+}). Six samples (1 mL each) containing 10 µM mant-ATP and 2.5 µM dialysed protein were prepared and supplemented with either 8 M urea, 2 mM $MgCl_2$, 1 mM ATP, 1 mM NMN, and 1 mM NAD. To the samples containing the nucleotide ligands, 2 mM $MgCl_2$ was added. Blanks were also prepared for the respective samples by excluding 2.5 µM protein.

In order to examine the interaction of the divalent metal cations, 2 mM of $MgCl_2$, $NiSO_4$, $CaCl_2$, $ZnSO_4$, and $CuSO_4$ were each prepared in 25 mM Tris-HCl pH 7.5. Analysis was performed using a 1 mL reaction volume containing 10 µM mant-ATP and 2.5 µM dialysed protein in the respective metal salt buffers. Blanks were also prepared for the respective test samples by excluding the 2.5 µM protein. All samples were excited at 355 nm with emission spectra collected over a 400–600 nm wavelength range using a 10 mm path length quartz cuvette in a Jasco FP-6300 spectrofluorometer (20 °C, 2.5 nm bandwidth, 1 nm data pitch, 200 nm/min scanning speed). For each sample, three scans were collected, averaged, and corrected for the signal from free mant-ATP and the buffer. The resulting spectra were processed using SigmaPlot.

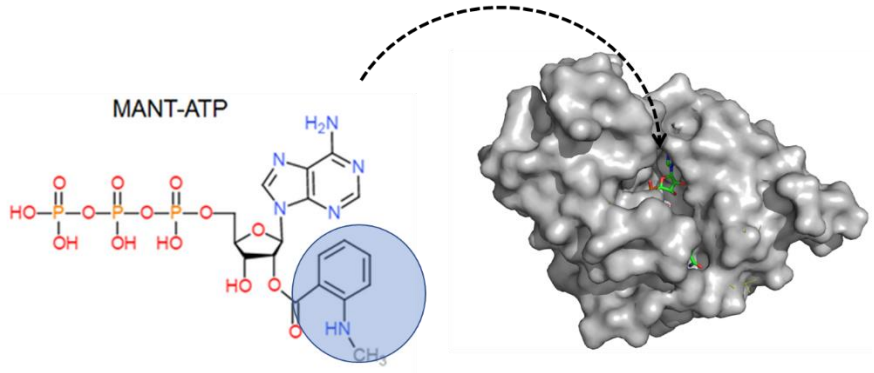

Figure 5.2. Pictorial representation of the binding of 2′/3′-O-(N-Methyl-anthraniloyl)-adenosine-5′-triphosphate (mant-ATP) to the nucleotide binding site on NaMNAT protein.
The blue ring indicates the fluorophore N-methylanthraniloyl present in the mant-ATP.

SYPRO Orange thermal shift assay

To determine the melting temperature (T_m) of recombinant *Kp*NaMNAT and *Ef*NaMNAT, SYPRO Orange dye was used to monitor the thermal denaturation of the recombinant proteins. This study was conducted in the absence and presence of ATP and

divalent metal cations (Mg^{2+}, Ni^{2+}, Ca^{2+}, Zn^{2+}, and Cu^{2+}) using a Real-Time PCR Detection System (Bio-Rad CFX96 Touch)

The protein sample was dialysed in two changes against 25 mM Tris-HCl, at 4 °C for 3 and 16 h respectively, using a 10 kDa molecular weight cut-off dialysis tube. Stock concertation of the protein samples (50 µM) was prepared by resuspending the proteins in ddH_2O. Based on the varying requirements, buffers were prepared as follows; Buffer-A (25 mM Tris-HCl, pH 7.5), Buffer-B (25 mM Tris-HCl, 0.1 mM ATP, pH 7.5), Buffer-C (25 mM Tris-HCl, 0.1 mM ATP, and 5 mM metal salt, pH 7.5), and Buffer-D (25 mM Tris-HCl, and 5 mM metal salt, pH 7.5). The metal salts supplemented into buffers- "C" and "D" were $MgCl_2$, $NiSO_4$, $CaCl_2$, $ZnSO_4$, and $CuSO_4$. To assay the proteins in the absence of ligand, Buffer-A was used while Buffer-B was used in the presence of ATP ligand only. Buffer-C was used to assay the proteins and their interaction with ATP and various divalent metals, while Buffer-D was used to assay the proteins and their interaction with the various divalent metal ions in the absence of ATP.

The 96 well PCR microplate (Bio-Rad) was prepared, as shown in Figure 5.3. Each of the 96 wells of the PCR microplate was aliquoted 10 µL of buffer, 10 µL of protein, and 5 µL of SYPRO Orange dye, making a 25 µL reaction volume. The final protein concentration to dye concentration in the mixture was 20 µM : 10 ×. The plate was sealed with a Microseal 'B' PCR Plate Sealing Film (Bio-Rad), vortexed, and then centrifuged for 30 sec before running in a Real-Time PCR Detection System.

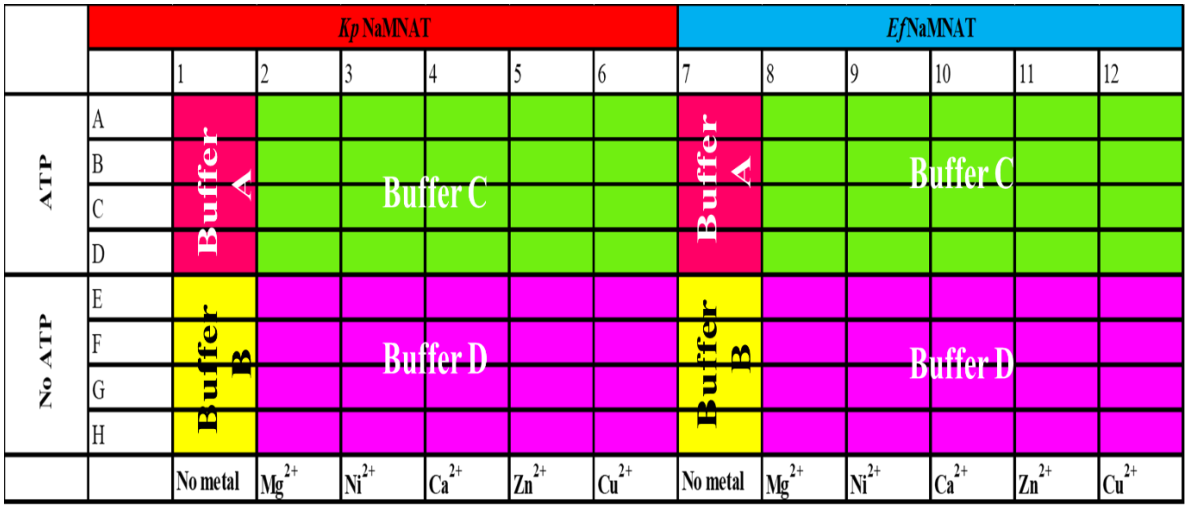

Figure 5.3. Pictorial representation of the 96-well PCR multi-plate showing the experiment layout.

The melting curve was obtained at 20 °C to 80 °C in increments of 0.5 °C for 10 sec. Each sample was conducted in quadruplicate, averaged, and corrected for buffer and dye fluorescence signal. Upon completion, the relative fluorescence unit (RFU) and the derivative of the fluorescence signal with respect to the temperature (-d(RFU)/dT) were accessible via CFX Maestro software and exported to excel. The average RFU or -d(RFU)/dT was corrected by subtracting the averaged blank. The fraction unfolded was determined using the corrected average of the RFU. The fraction unfolded, and the corrected average of (- d(RFU)/dT) were plotted individually against temperature.

5.3.3 Quaternary structure analysis

The native size of both proteins was deduced using SE-HPLC (UFLC Shimadzu) by measuring the retention time of the protein. A TSKgel SuperSW2000 column (Tosoh Bioscience), made of silica base material stationary phase with a mean particle size of 4 µm, 12.5 nm pore size, and a fractionation range of 5–150 kDa was used. The column (4.6 × 300 mm) was equilibrated with the prepared SE-HPLC buffer at 20 °C. A 20 µL of protein sample (~7.4 mg/mL *Kp*NaMNAT and ~6.5 mg/mL *Ef*NaMNAT) were loaded into the column at a flow rate of 0.2 mL/min for 40 min. The elution of protein was detected at 280 nm. To deduce the apparent molecular weight of the proteins 20 µL of Bio-Rad gel filtration standard molecular weight markers (Appendix A) were loaded onto the column, and they were analysed under the same conditions. A calibration curve of log molecular weight (M_r) of the standard proteins against their retention time was constructed. The resulting retention time of the proteins was used to estimate their molecular weight and subsequent oligomeric state from the calibration curve.

5.4 Results

Far-UV circular dichroism (CD) spectroscopy

Based on the ability to polarise light, the peptide bonds of K*p*NaMNAT and *Ef*NaMNAT served as a chromophore in the far-UV region. Analysis of the resulting CD spectra showed a peak of positive ellipticity at 190±0.5 nm and two troughs with a negative ellipticity at 220±0.5 nm and 208±0.5 nm (Figure 5.4), suggesting that the recombinant proteins were predominately α-helical (Greenfield, 2006). The deconvolution of the CD spectra data via DichroWeb analysis program, CONTINLL algorithm, reference set 6 (Provencher and Gloeckner, 1981; Sreerama and Woody, 2000) further revealed that *Ef*NaMNAT exhibited more α-helix and β-strand than

*Kp*NaMNAT. However, *Kp*NaMNAT exhibited additional unordered coils, which seems to be absent in the secondary structure content of *Ef*NaMNAT (Table 5.1). In the presence of a denaturant (8 M urea), both proteins exhibited loss of both positive and negative ellipticity.

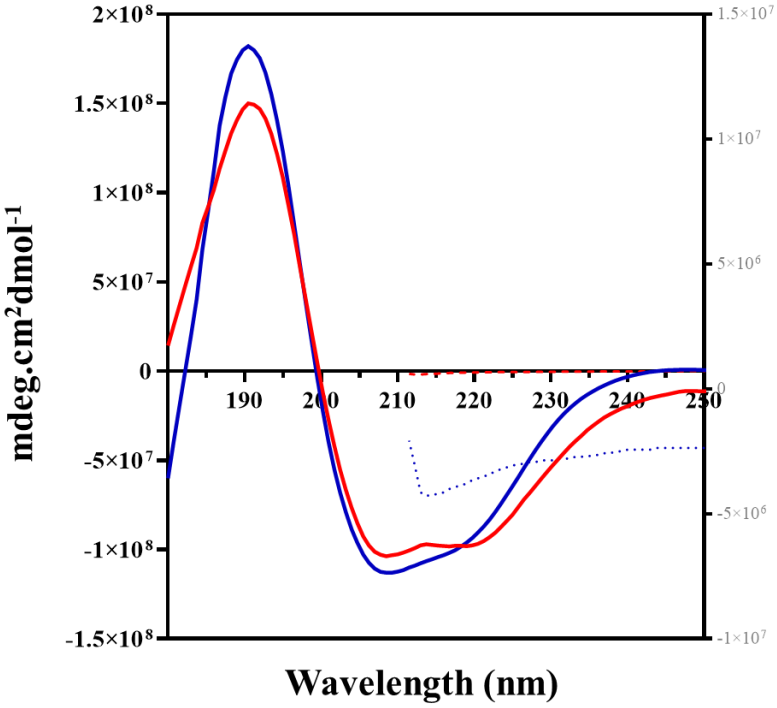

Figure 5.4. Characteristic far-UV CD spectra of *Kp*NaMNAT and *Ef*NaMNAT.
Recombinant *Kp*NaMNAT represented in the red spectrum and *Ef*NaMNAT represented in the blue spectrum were analysed in 10 mM NaH_2PO_4, pH 7.5, using CD QS 1 mm standard cuvette, 1 nm bandwidth, and 0.5 nm data pitch at 20 °C. The resulting CD spectra of the proteins display peaks of positive ellipticity at 190±0.5 nm and negative ellipticity at 220±0.5 nm and 208±0.5 nm. The corresponding denatured proteins are represented in dotted lines. *Kp*NaMNAT is plotted along the secondary *y*-axis.

Table 5.1. Calculated secondary structure fractions of the recombinant NaMNAT proteins as derived from DichroWeb analysis program- Contin-LL (Provencher and Gloeckner Method), reference set 6.

NaMNAT Protein	α Helix (%)	β Strand (%)	β Turn (%)	Unordered (%)	NRMSD
*Kp*NaMNAT	57.2	8.2	21.3	13.3	0.075
*Ef*NaMNAT	63.0	16.0	21.0	0.0	0.115

*NRMSD- Normalised root-mean-square deviation indicates how best fit is the estimated data to the experimental data. Low values are accepted as a good fit.

Extrinsic ANS fluorescence spectroscopy

The hydrophobicity of the recombinant proteins and the interaction of the ligands with the protein were analysed using ANS anionic dye. This was possible because of the spectral properties of the anionic dye. Changes in the fluorescence intensity and shifts in the emission

spectra of ANS provide insight into the polarity and fluctuations in the protein binding pockets. In the fluorescence binding studies conducted, excitation of ANS at 395 nm resulted in a significant increase in quantum yield (ΔΦ) and a blueshift in the maximum emission wavelength, from 508 nm to 499 nm for *Kp*NaMNAT and 513 nm to 506 nm for *Ef*NaMNAT, which is characteristic of ANS interacting with a hydrophobic pocket of a protein (Gasymov and Glasgow, 2007). Compared to *Kp*NaMNAT in its native form, the interaction of ANS with denatured *Kp*NaMNAT resulted in a 12 nm redshift and a decrease in fluorescence ΔΦ. In the presence of 1 mM ATP, 1 mM NMN, and 1 mM $NAD^{+,}$ there was no shift observed in the maximum emission wavelength of ANS. But a decrease in ΔΦ was demonstrated in the order of NMN, ATP, and NAD^+ (Figure 5.5A). Table 5.2 shows the tabulated result.

Similarly, when compared to its native, the denatured conformation of *Ef*NaMNAT displayed a 2 nm redshift and a decrease in the ΔΦ of ANS fluorescence (Figure 5.5B). In the presence of 1 mM ATP, 1 mM NMN, and 1 mM NAD^+, a decrease in the ΔΦ of ANS fluorescence was observed coupled with a 5 nm blueshift in emission wavelength for each of the ligands (Table 5.2). The fluorescence spectra showing the absorbance of all ligands in the presence and absence of ANS can be found in Figure S4 appendix B.

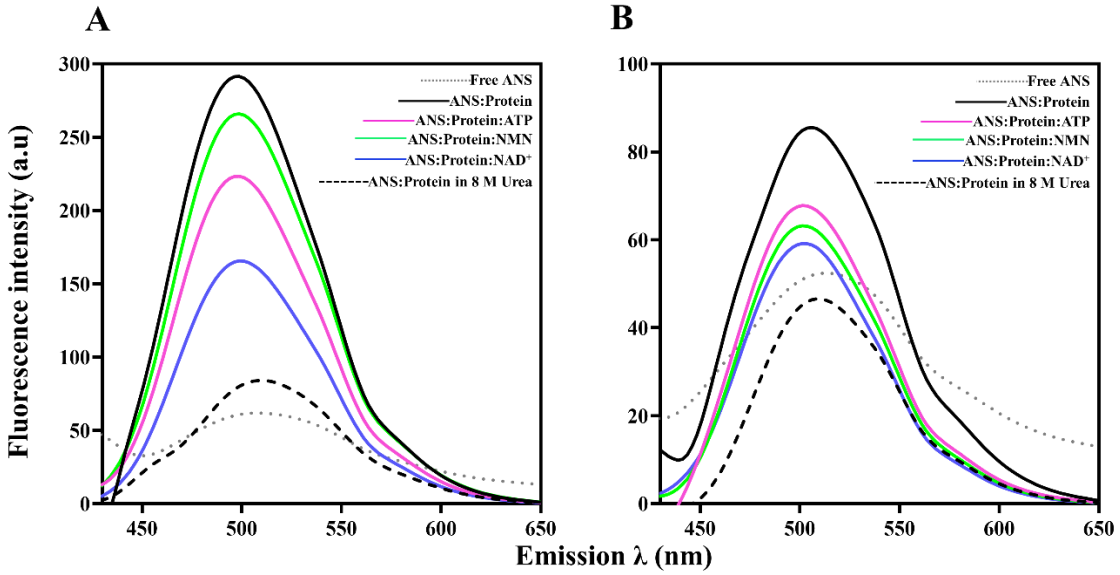

Figure 5.5. ANS fluorescence emission spectra of recombinant (A) *Kp*NaMNAT and (B) *Ef*NaMNAT in the absence and presence of nucleotide ligands.
ANS was excited at 395 nm and emission spectra collected between 400 and 650 nm. Analysis of the proteins in the presence of 8M urea, 1 mM ATP, 1 mM NMN, and 1 mM NAD^+ was performed in 10 mM NaH_2PO_4, 0.01% (w/v) NaN_3, and 1 mM DTT, pH 7.5. The resulting spectra for both proteins appear similar, as both proteins display decreases in quantum yield upon ATP, NMN, and NAD^+ binding compared to the apo. However, the fluorescence intensity observed for *Kp*NaMNAT is much higher than in *Ef*NaMNAT. ANS in buffer is represented by the gray dotted lines.

Table 5.2. Fluorescence properties of ANS upon binding to *Kp*NaMNAT and *Ef*NaMNAT in their native and denatured forms, and in the presence of ATP, NMN, and NAD^+, in relation to the native protein.

		Maximum emission wavelength (λ) nm	Quantum yield (ΔΦ) relative to Apo	Shift relative to Apo (nm)	Type of shift relative to Apo
*Kp*NaMNAT	**Native**	499	Baseline	Baseline	Baseline
	Denatured	511	Decrease	12	Redshift
	ATP	499	Decrease	0	No shift
	NMN	499	Decrease	0	No shift
	NAD^+	499	Decrease	0	No shift
*Ef*NaMNAT	**Native**	506	Baseline	Baseline	Baseline
	Denatured	508	Decrease	2	Redshift
	ATP	501	Decrease	5	Blueshift
	NMN	501	Decrease	5	Blueshift
	NAD^+	501	Decrease	5	Blueshift

In the presence of the varying divalent metal cations, an increase in ANS fluorescence intensity coupled with a blueshift was observed for *Kp*NaMNAT in the presence of Ni^{2+}, $Zn^{2+,}$ and Cu^{2+}. However, in the presence of Mg^{2+}, and Ca^{2+}, a slight decrease in ANS fluorescence intensity and a redshift was observed (Figure 5.6A). *Ef*NaMNAT exhibited an increase in ANS fluorescence intensity in the order of Mg^{2+}, Cu^{2+}, Ca^{2+}, $Ni^{2+,}$ and Zn^{2+} (Figure 5.6B), with Cu^{2+}, $Ni^{2+,}$ and Zn^{2+} displaying a blueshift while Mg^{2+} and Ca^{2+} showed a redshift in the maximum emission wavelength. Table 5.3 shows the tabulated result.

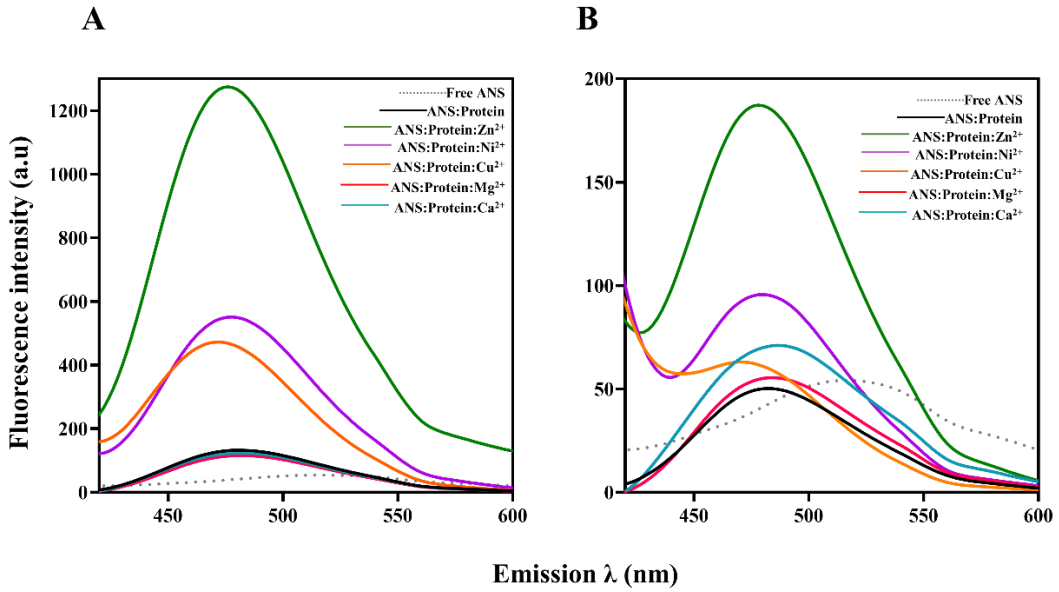

Figure 5.6. ANS fluorescence emission spectra of recombinant (A) *Kp*NaMNAT and (B) *Ef*NaMNAT in the absence and presence of divalent cations.
ANS was excited at 395 nm and emission spectra collected between 400 and 650 nm. Analysis was performed in 25 mM Tris-HCl containing 2 mM of respective metal salt (**Mg^{2+}**, Ni^{2+}, Ca^{2+}, Cu^{2+} and Zn^{2+}), pH 7.5. The resulting spectra for both proteins indicate an increase in quantum yield in the presence of Zn^{2+}, Ni^{2+}, and Cu^{2+}. The gray dotted lines represent ANS in buffer.

Table 5.3. Fluorescence properties of ANS upon binding to *Kp*NaMNAT and *Ef*NaMNAT in the presence of varying divalent metal cations in relation to no metal.

		Maximum emission wavelength (λ) nm	Quantum yield (ΔΦ) relative to Apo	Shift relative to Apo (nm)	Type of shift relative to Apo
***Kp*NaMNAT**	**No Metal**	480	Baseline	Baseline	Baseline
	Mg^{2+}	482	Slight decrease	2	Redshift
	Ni^{2+}	478	Increase	2	Blueshift
	Ca^{2+}	482	Slight decrease	2	Redshift
	Zn^{2+}	470	Increase	10	Blueshift
	Cu^{2+}	472	Increase	8	Blueshift
***Ef*NaMNAT**	**No Metal**	482	Baseline	Baseline	Baseline
	Mg^{2+}	484	Increase	2	Redshift
	Ni^{2+}	480	Increase	2	Blueshift
	Ca^{2+}	486	Increase	4	Redshift
	Zn^{2+}	478	Increase	4	Blueshift
	Cu^{2+}	470	Increase	12	Blueshift

Extrinsic mant-ATP fluorescence spectroscopy

Mant-ATP is a fluorescent analogue that contains N-methylanthraniloyl chromophore (Figure 5.2), which is used as an external probe to reveal nucleotide-binding sites within a protein. The binding of mant-ATP to the respective recombinant proteins (Figure 5.7) was accompanied by an increase in the ΔΦ and a blueshift in the maximum emission wavelength from 450 nm to 430 nm for *Kp*NaMNAT and 450 nm to 442 nm for *Ef*NaMNAT. The interaction of mant-ATP with *Kp*NaMNAT in the presence of 1 mM ATP and 1 mM NAD^+ resulted in fluorescence quenching and a redshift in the maximum emission wavelength to 436 nm in the presence of ATP and 446 nm for NAD^+. However, a blueshift to 428 nm was observed in the presence of 5 mM Mg^{2+}. The fluorescence spectra for denatured *Kp*NaMNAT compared to its native form displayed a decreased ΔΦ and a redshift in maximum emission wavelength from 430 to 448 nm. Table 5.4 shows the tabulated results.

Similarly, the binding of mant-ATP to *Ef*NaMNAT in the presence of 5 mM Mg^{2+}, 1 mM ATP and 1 mM NAD^+ resulted in fluorescence quenching and redshifts in the maximum emission wavelength to 450, 454, and 452 nm, respectively. On the other hand, the fluorescence spectra for denatured *Ef*NaMNAT displayed no shift in the maximum emission wavelength; however, there was a decrease in the ΔΦ (Table 5.4).

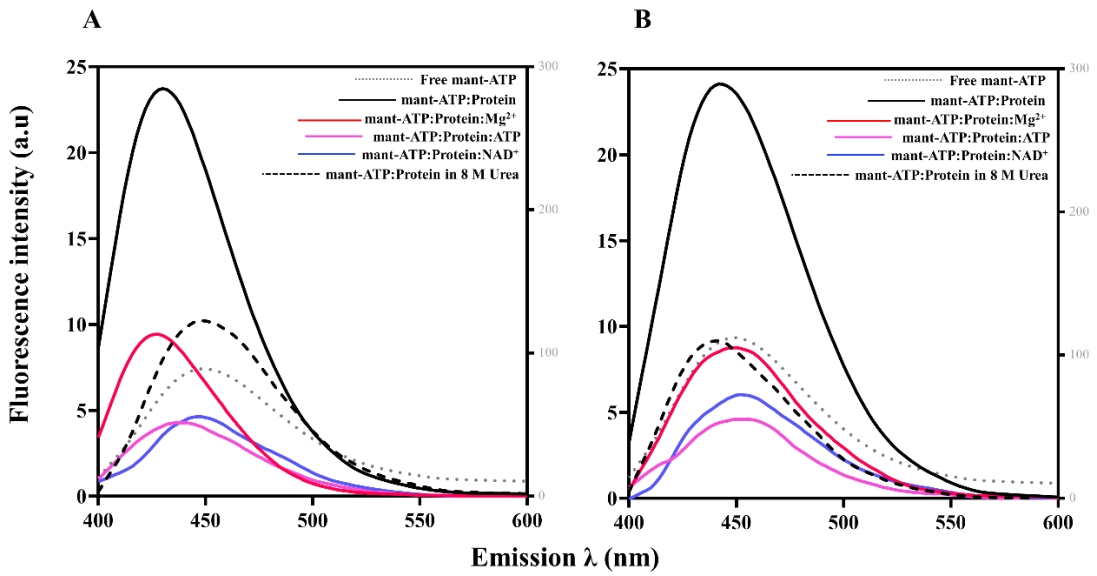

Figure 5.7. Fluorescence emission spectra of mant-ATP interacting with (A) *Kp*NaMNAT and (B) *Ef*NaMNAT nucleotide-binding site.
Analysis of the proteins in the presence of the nucleotide ligands was carried out in 10 mM NaH_2PO_4, 0.01% (w/v) NaN_3, pH 7.5 containing 10 µM mant-ATP and 2.5 µM protein. The specific binding of mant-ATP to *Kp*NaMNAT and *Ef*NaMNAT in the presence of Mg^{2+}, ATP, NAD^+, and 8 M urea resulted in the fluorescence quenching of mant-ATP, compared to the Native form. Excitation was at 355 nm, and emission spectra were collected between 400 and 600 nm. The free mant-ATP is represented by gray dotted lines and is plotted along the secondary *y*-axis.

Table 5.4. Showing the fluorescence properties of mant-ATP upon binding to *Kp*NaMNAT and *Ef*NaMNAT in their native and denatured forms, as well as in the presence of Mg^{2+}, ATP, NMN, and NAD^+, in relation to the native protein

		Maximum emission wavelength (λ) nm	Quantum yield (ΔΦ) relative to Apo	Shift relative to Apo (nm)	Type of shift relative to Apo
***Kp*NaMNAT**	**Native**	430	Baseline	Baseline	Baseline
	Denatured	448	Decrease	18	Redshift
	Mg^{2+}	428	Decrease	2	Blueshift
	ATP	436	Decrease	6	Redshift
	NAD^+	446	Decrease	16	Redshift
***Ef*NaMNAT**	**Native**	442	Baseline	Baseline	Baseline
	Denatured	442	Decrease	0	No shift
	Mg^{2+}	450	Decrease	8	Redshift
	ATP	454	Decrease	12	Redshift
	NAD^+	452	Decrease	10	Redshift

In the presence of the divalent metal cations, the binding of mant-ATP to *Kp*NaMNAT was followed by a decrease in fluorescence intensity (Figure 5.8A) and redshifts in the maximum emission wavelength to 432 nm and 460 nm in the presence of Zn^{2+}, and Ca^{2+} respectively. However, Mg^{2+} and Ni^{2+} displayed a blueshift, with a maximum emission wavelength of 426 nm and 422 nm, respectively. Conversely, *Ef*NaMNAT in the presence of all the metals demonstrated a decrease in mant-ATP fluorescence (Figure 5.8B) and redshifts in the maximum emission wavelength for Mg^{2+}, while blueshifts were observed for Zn^{2+} and Ca^{2+}. Table 5.5 shows the tabulated results.

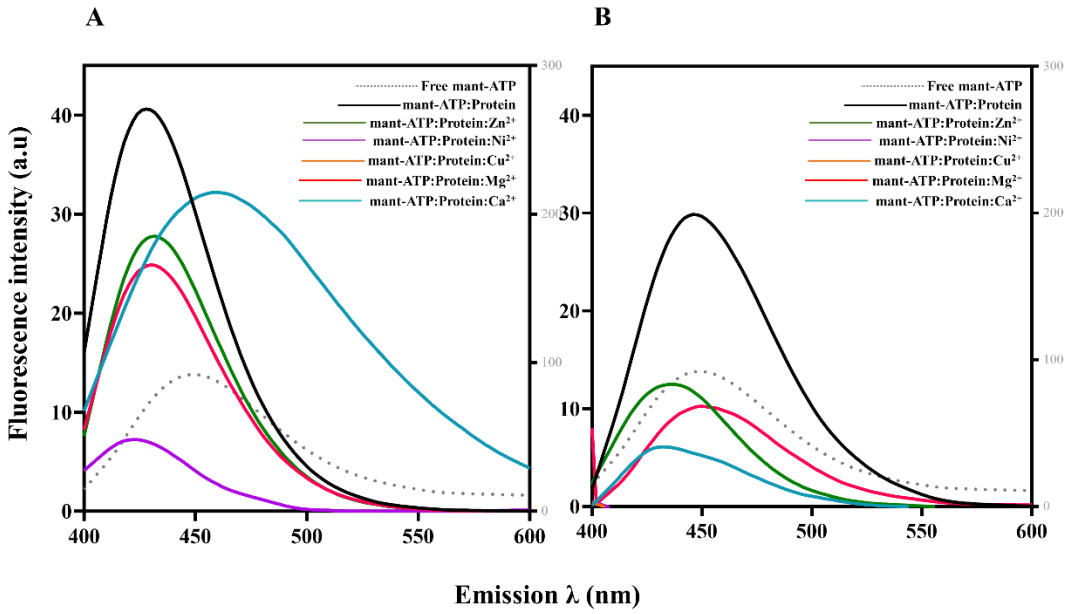

Figure 5.8. Fluorescence emission spectra of mant-ATP interacting with (A) *Kp*NaMNAT and (B) *Ef*NaMNAT in the absence and presence of divalent cations.
Compared to the native proteins, a decrease in the fluorescence intensity of mant-ATP was observed in the presence of the divalent metals (Mg^{2+}, Ni^{2+}, Ca^{2+}, Cu^{2+} and Zn^{2+}). The quenching effect of Ni^{2+} and Cu^{2+} is more evident in *Ef*NaMNAT than in *Kp*NaMNAT. Analysis of the proteins and the divalent cations was measured in 25 mM Tris-HCl, containing 2 mM salt of respective metals, pH 7.5. Excitation was at 355 nm, and emission spectra were collected between 400 and 600 nm. The free mant-ATP is represented by gray dotted lines and is plotted along the secondary *y*-axis.

Table 5.5. Showing the fluorescence properties of mant-ATP upon binding to *Kp*NaMNAT and *Ef*NaMNAT in the presence of varying divalent metal cations in relation to no metal.

		Maximum emission wavelength (λ) nm	Quantum yield (ΔΦ) relative to Apo	Shift relative to Apo (nm)	Type of shift relative to Apo
***Kp*NaMNAT**	**No Metal**	428	Baseline	Baseline	Baseline
	Mg^{2+}	426	Decrease	2	Blueshift
	Ni^{2+}	422	Decrease	6	Blueshift
	Ca^{2+}	460	Decrease	32	Redshift
	Zn^{2+}	432	Decrease	4	Redshift
	Cu^{2+}	ND	Decrease	ND	ND
***Ef*NaMNAT**	**No Metal**	444	Baseline	Baseline	Baseline
	Mg^{2+}	450	Decrease	6	Redshift
	Ni^{2+}	ND	Decrease	ND	ND
	Ca^{2+}	432	Decrease	12	Blueshift
	Zn^{2+}	436	Decrease	8	Blueshift
	Cu^{2+}	ND	Decrease	ND	ND

ND*- Not determined.

SYPRO Orange thermal shift assay

The binding of SYPRO Orange to proteins is such that as the temperature increases, the protein unfolds, allowing the dye to access more hydrophobic pockets, consequently increasing its fluorescence. The thermal denaturation assay conducted using SYPRO Orange dye (Figure 5.9 and Table 5.6) showed *Kp*NaMNAT to exhibit a T_m of 40 °C in the absence of ligands while in the presence of ATP, its T_m slightly increases by 0.5 °C. The addition of Mg^{2+} in the absence and presence of ATP did not impact the T_m of the protein, but Ca^{2+} increases the T_m by 0.5 °C both in the absence and presence of ATP. Ni^{2+} decreases the T_m of the protein to 39 °C with a high initial unfolding transition, however, the addition of Zn^{2+}, and Cu^{2+} resulted in lack of unfolding transition with a decreasing T_m of 39 °C and 36 °C, in the absence of ATP and 37 °C and 39 °C in the presence of ATP, respectively.

*Ef*NaMNAT, on the other hand, displayed a T_m value of 43 °C in the absence of ligands and 47 °C in the presence of ATP, which is higher than what was obtained for *Kp*NaMNAT. The addition of the metals both in the absence and presence of ATP showed a rightward shift in the melting curve coupled with an increasing T_m in the order of Ca^{2+}, Mg^{2+}, Zn^{2+}, Ni^{2+}, and Cu^{2+}. The absorbance spectra for ATP and all the cations are shown in Figure S5 appendix B.

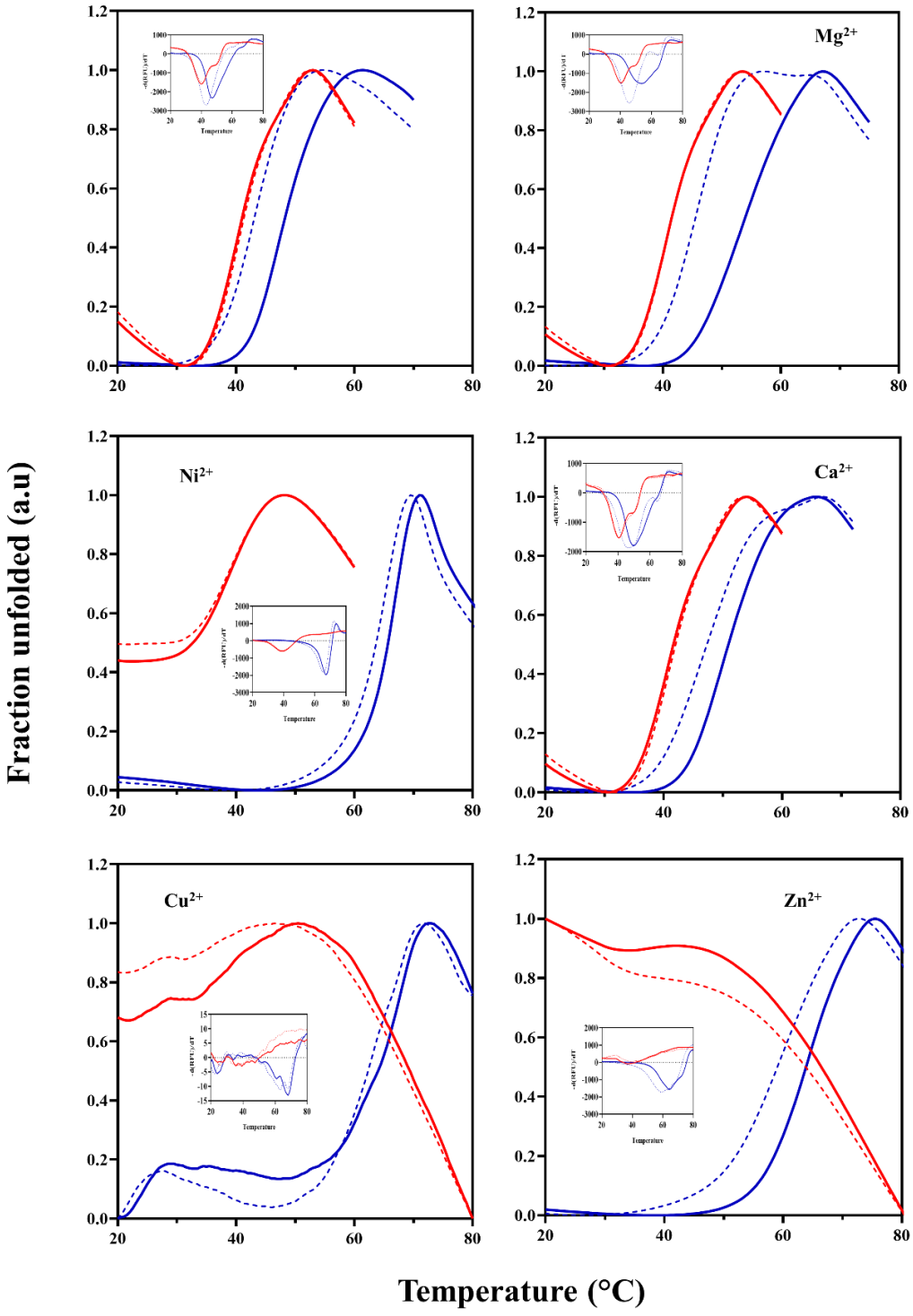

Figure 5.9. Thermal denaturation profile of recombinant *Kp*NaMNAT and *Ef*NaMNAT.
The thermal shift analysis of the recombinant protein's stability and ligand interactions was monitored using SYPRO Orange dye in 25 mM Tris-HCl, pH 7.5 with 0.1 mM ATP, and 5 mM metal salts ($MgCl_2$, $NiSO_4$, $CaCl_2$, $ZnSO_4$, and $CuSO_4$). The melting curve and melting peak for *Kp*NaMNAT are represented in red and for *Ef*NaMNAT in blue. The thermal unfolding was analysed in the absence (dotted lines) and presence (solid lines) of ATP and the different divalent metal cations. As the temperature increase, fluorescence emission also increases, giving rise to a sigmoidal curve that shows the transition of protein unfolding. The lack of a transition observed for *Kp*NaMNAT in the presence of Zn^{2+} and Cu^{2+} indicates that the protein is not well folded, while the high initial unfolding transition observed for Ni^{2+} indicates that the protein is partially unfolded at room temperature. A rightward shift as observed in the unfolding transition and melting peak of *Ef*NaMNAT in the presence of ligands indicates increasing stability.

Table 5.6. Showing the melting temperature (Tm) for *Kp*NaMNAT and *Ef*NaMNAT in the absence and presence of ATP and varying divalent metal cations

	***Kp*NaMNAT (°C)**		***Ef*NaMNAT (°C)**	
	No ATP	**ATP**	**No ATP**	**ATP**
No Metal	40.5	40.0	43.0	47.0
Mg^{2+}	40.5	40.5	45.5	53.5
Ni^{2+}	39.0	39.0	65.5	67.0
Ca^{2+}	41.0	40.5	46.5	49.5
Zn^{2+}	39.0	37.0	59.5	64.5
Cu^{2+}	36.0	39.0	63.5	68.0

Size exclusion high-pressure liquid chromatography (SE-HPLC)

To deduce the native molecular weight of the recombinant proteins, they were subjected to SE-HPLC, whereby a calibration curve of log molecular weight (M_r) of the standard proteins against their retention time was constructed (Figure 5.10B). The resulting chromatogram (Figure 5.10A) depicts a single peak with a retention time of 16.95 min for *Ef*NaMNAT. This retention time was estimated to be ~40 kDa on the calibration curve. On the other hand, two distinctive peaks labelled A and B were observed for *Kp*NaMNAT with a retention time of 18.39 and 16.49 min. These were estimated to be ~20 kDa and ~50 kDa, respectively, on the calibrations curve.

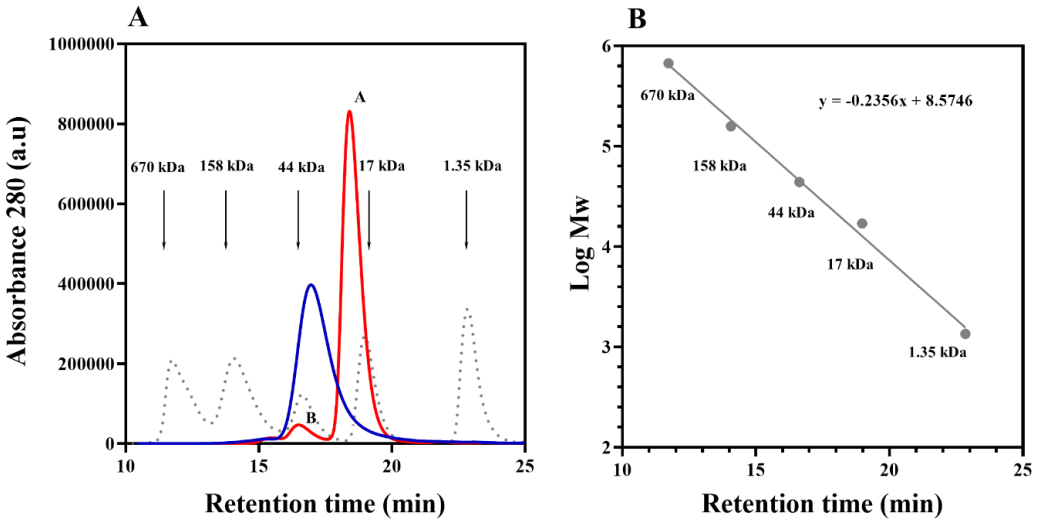

Figure 5.10. Quaternary structure characterisation of *Kp*NaMNAT and *Ef*NaMNAT by Size Exclusion-HPLC

(A) Chromatogram of recombinant and standard proteins determined in 10 mM NaH_2PO_4, 750 mM NaCl, and 0.01% (w/v) NaN_3, pH 7, at 20 °C. The elution profile of the standard proteins is depicted in gray dotted lines, *Kp*NaMNAT in red, and *Ef*NaMNAT in solid blue lines. The arrows indicate the standard molecular weight markers (Vitamin B 12 1.35, Myoglobin 17, Ovalbumin 44, g-globulin 158, and Thyroglobulin 670 kDa). (B) Constructed calibration curve of log Molecular Weight (M_r) of the standard proteins against their retention time, used to estimate the quaternary size of the proteins. The molecular weight for the 2 distinctive peaks of *Kp*NaMNAT (A and B) was ~20 kDa and ~50 kDa, respectively, while *Ef*NaMNAT was estimated to be ~40 kDa

5.5 Discussion

NMNATs are globular proteins belonging to the α/β class. The N-terminal domain of Na/NMNATs is characterised by the presence of β-strands (β) and α-helices (α), whereas the C terminal domain of NMNATs is mainly comprised of α-helices and loops (Lau *et al.*, 2009), which function in the identification of substrate preference. The predominant α-helical characteristic feature displayed by the recombinant *Kp*NaMNAT and *Ef*NaMNAT (Figure 5.4, Table 5.1) corresponds with most identified NMNAT (Saridakis *et al.*, 2001; Werner *et al.*, 2002; Zhang *et al.*, 2002; Yoon *et al.*, 2005) given, that all NaMNATs share a common dinucleotide binding domain characterised by alternating α-helices and β-strands. The loss of both positive and negative ellipticity demonstrated by the recombinant proteins in denaturant presence indicates loss of secondary structure upon protein unfolding; thus, suggesting that the purified recombinant *Kp*NaMNAT and *Ef*NaMNAT were in their native conformation.

Besides the characterised dinucleotide binding domain known as Rossmann fold, NMNATs possess a highly conserved active site sequence motif (H/T)XGH (Izard and Geerlof, 1999) required for recognition and binding of substrates (Figure 2.6). In the absence of a three-dimensional structure of *Kp*NaMNAT and *Ef*NaMNAT, insight into the recombinant proteins' structural conformation and ligand binding properties were probed using ANS and mant-ATP, owing to their strong fluorescence energy transfer properties. Following the observable attributes of these fluorescent dyes (Gasymov and Glasgow, 2007), a blueshift in maximum emission wavelength coupled with an increase of fluorescence intensity (quantum yield) was obtained upon the binding of ANS or mant-ATP to the recombinant proteins, thus, establishing the presence of binding pockets. The 2 nm redshift observed in *Ef*NaMNAT upon unfolding as compared to the 12 nm redshift for unfolded *Kp*NaMNAT in the ANS binding studies (Table 5.2) suggests that the binding pocket in *Ef*NaMNAT appears to be exposed to aqueous solvent and located in a more hydrophilic region compared to *Kp*NaMNAT whose binding site seems to be more buried and comparatively devoid of aqueous solvent. This is further supported by the differences observed in the quantum yield of the recombinant proteins as ANS can access more hydrophobic pockets in *Kp*NaMNAT compared to *Ef*NaMNAT, hence a higher quantum yield obtained for *Kp*NaMNAT upon ANS binding, which is three times more than the quantum yield obtained for *Ef*NaMNAT (Figure 5.5). This is indicative of the nature of the hydrophobicity of *Ef*NaMNAT and *Kp*NaMNAT binding pockets. Equally, mant-ATP interaction with the unfolded *Ef*NaMNAT yielded no significant shift in the emission wavelength compared to the 18 nm redshift observed for *Kp*NaMNAT (Table 5.4), further

supporting the differences in the hydrophobicity of the nucleotide binding sites. This is no surprise considering that both proteins only share about 30% sequence identity. More so, the differences in the quaternary structure exhibited by the proteins could be a contributing factor since the oligomeric structure of *Ef*NaMNAT is dimeric, and *Kp*NaMNAT majorly exists as a monomer in solution (Figure 5.10) (Olland *et al.*, 2002; Zhang *et al.*, 2003).

The synthesis of NAD^+ by NaMNAT involves the binding of two substrates, ATP and NMN to form PPi and NAD^+. Generally, NaMNAT is believed to catalyse adenylyl transfer by a nucleophilic attack on the α-phosphate of ATP by the 5' phosphate of the mononucleotide resulting in the cleavage of the ester bond between the α- and β-phosphates of ATP and the displacement of NMN at the α-phosphate, thus releasing NAD^+ and inorganic pyrophosphate from the enzyme (Lowe and Tansley, 1983). Although the order of substrate binding mechanism in *Kp*NaMNAT and *Ef*NaMNAT is unknown, upon the binding of each ligand (ATP, NMN, or NAD^+) to the recombinant proteins, the result in this study showed a decrease in fluorescence intensity of ANS and mant-ATP. This we presumed to be due to the higher affinity of the ligands for the binding site (Figure 5.5 and 5.7) given that the presence of highly conserved histidine residues of the "H/TXGH" motif (Figure 2.6) and other positively charged residues such as arginine at the binding site interact with the phosphoryl group of the nucleotide ligand (Olland *et al.*, 2002; Zhang *et al.*, 2002) thereby restricting the binding of the anionic dyes while favouring the interaction of the ligands within the active site. Furthermore, considering that mant-ATP is a fluorescent analogy of ATP, the displacement of mant-ATP as observed by the decrease in fluorescent intensity upon the binding of NMN and NAD^+ suggests the possibility of these ligands sharing a common binding site with ATP.

The binding of ligands to proteins usually induces conformational changes that may consequently affect the function of the proteins. In the presence of ANS, the binding of ATP, NMN, and NAD^+ to *Ef*NaMNAT resulted in a blueshift in the fluorescence emission wavelength (Table 5.2), suggestive of ligand-induced conformational changes. This blueshift is noteworthy considering that *Ef*NaMNAT demonstrated a binding pocket that appears to be more solvent-exposed. We presume that the binding of the ligands reconfigures the side chains of some residues lining the binding domain. Hence, resulting in the formation of a hydrophobic transient subpocket (Stank *et al.*, 2016) or a more closed active site as described in *E.coli* NaMNAT, which buries more than 90% of the bound $NaAD^+$ (Zhang *et al.*, 2002) or yet a deep cleft similar to what (D'Angelo *et al.*, 2000) observed of archaeal NaMNAT catalytic site location. This conformational flexibility displayed may not only be necessary for substrates binding, but it may also play a role in facilitating product release (Saridakis *et al.*, 2001).

On the contrary, the binding of the ligands ATP, NMN, and NAD^+ induced no significant conformational change in *Kp*NaMNAT, as demonstrated by there being no shift in maximum emission wavelength. Although massive conformational changes in many loop regions around the active site of *E. coli* NaMNAT and *B. Subtillis* NaMNAT were reported upon the binding of $NaAD^+$ (Olland *et al.*, 2002; Zhang *et al.*, 2002), there are also reports of relatively little or no conformational change induced upon ligand binding to human cytosolic NaMNAT (Zhang *et al.*, 2003) and *P. aeruginos*a NaMNAT (Yoon *et al.*, 2005). Therefore, the possibility of conformational changes only occurring upon the simultaneous binding of the two substrates in the active site may be true for *Kp*NaMNAT (Yoon *et al.*, 2005). This could also be an indication to the kind of binding mechanism demonstrated by the two proteins. However, further kinetic and direct binding studies will be required in order to describe this process effectively.

Given that ATP binding is highly conserved and bacterial NaMNATs exhibit a highly conserved ATP binding site (Lau *et al.*, 2009), the changes in the hydrophobicity of the binding site observed upon ATP binding in the presence of Mg^{2+} possibly ensued from the polarisation of the active site by magnesium ions proximate to the α-phosphate of ATP so as to support the nucleophilic attack on the α-phosphate of ATP by the 5′ phosphate of the mononucleotide (D'Angelo *et al.*, 2000). Furthermore, the presence of the conserved histidine residues of the "H/TXGH" motif and other positively charged residues such as arginine (Olland *et al.*, 2002; Zhang *et al.*, 2002) within the active site facilitate nucleotidylation of NMN (Veitch *et al.*, 1998) and provide stabilisation of the transition state by forming a hydrogen bond with the ATP phosphate oxygen atom (D'Angelo *et al.*, 2000). This hydrogen bond formation attracts water hence contributes to the alteration in the polarity of the microenvironment as observed in *Kp*NaMNAT and *Ef*NaMNAT. NAD^+/$NaAD^+$ as observed in *sa*NaMNAT (Han *et al.*, 2006), *bs*NaMNAT (Olland *et al.*, 2002), and archaeal *mt*NMNAT (Saridakis *et al.*, 2001), is seen bound in an extended conformation to NaMNAT and buried in a deep cleft which is solvent accessible (Magni *et al.*, 1999) in readiness for release. This solvent-accessible pocket previously observed in other NaMNATs perhaps exist for *Kp*NaMNAT and *Ef*NaMNAT upon NAD^+ binding; hence, the changes observed in the hydrophobicity of the binding site.

Divalent cations such as Mg^{2+} play a vital role in the co-binding of nucleotides and catalysis. Besides Mg^{2+}, many studies have established Na/NMNAT isozyme to have a distinctive preference for varied divalent metal cations. The binding of Ca^{2+}, Cu^{2+}, Ni^{2+}, and Zn^{2+} to both proteins resulted in mant-ATP fluorescence quenching, similar to what was observed for Mg^{2+} (Figure 5.8). This is expected as the binding of metal cations should polarise

the active site to allow for substrate binding and phosphor transfer (D'Angelo *et al.*, 2000), thus indicating their efficiency in stabilising the NaMNAT-substrate complex. However, studies have shown that not all metals that substitute Mg^{2+} in substrate binding and phosphoryl transfer, are efficient at substrate turnover (Knape *et al.*, 2017). This is possibly true for *Kp*NaMNAT and *Ef*NaMNAT.

Moreover, previous investigations showed that the release of NAD^+/$NaAD^+$ product from NaMNAT binding site would require modification or significant rearrangement of the protein structure (Olland *et al.*, 2002; Han *et al.*, 2006). Upon binding Mg^{2+} and Ni^{2+} to *Kp*NaMNAT and the binding of Zn^{2+} and Ca^{2+} to *Ef*NaMNAT (Table 5.5), a shift in emission wavelength to higher energy was observed, suggesting an induced conformational change in the structure of the proteins. These conformational dynamics displayed possibly play a role in facilitating product release (Saridakis *et al.*, 2001), thus suggesting their unique role as an efficient cofactor in the enzyme's turnover. This is consistent and in agreement with the results obtained from the enzyme activity assay, indicating *Kp*NaMNAT to be optimally active in the presence of Mg^{2+} followed by Ni^{2+} and *Ef*NaMNAT in the presence of Zn^{2+}. Besides, the poor substrate turnover exhibited by Mg^{2+} when bound to *Ef*NaMNAT probably contributed to the reduced activity demonstrated by *Ef*NaMNAT towards NMN in the activity assay.

Akin to ANS, the binding of SYPRO Orange dye to hydrophobic surfaces in protein increases fluorescence. The significant increase in fluorescence intensity corresponds with increasing temperature, hence, resulting in a sigmoidal curve that signifies the unfolding of the protein (Figure 5.9). The T_m is the temperature at which 50% of the protein is denatured or unfolded and is at the inflection point of the unfolding curve. The higher the T_m of a protein, the more thermally stable it is, and any changes to the T_m signify an alteration in the stability. Compared to *Kp*NaMNAT, *Ef*NaMNAT demonstrated a higher Tm, thus suggesting *Ef*NaMNAT to be more stable than *Kp*NaMNAT (Table 5.6).

The binding of a ligand to protein tends to rigidify proteins, consequently increasing their stability. This attribute typically allows for the identification of protein-binding ligands through an increase in thermal stability. Upon ATP binding to *Ef*NaMNAT, a rightward shift in the unfolding curve coupled with an increase in T_m was observed, suggesting enhancement in *Ef*NaMNAT stability. This stability was further increased in the presence of Mg^{2+}. However, the binding of ATP and Mg^{2+} to *Kp*NaMNAT has minimal effect on its stability. This information is consistent with the ANS fluorescence spectroscopy study. It corresponds with the ligand-induced conformational changes observed for *Ef*NaMNAT upon the binding of ATP as well as the no conformational changes observed for *Kp*NaMNAT upon addition of ATP.

Considering the impact of Mg^{2+}, Ca^{2+}, Zn^{2+}, $Cu^{2+,}$ and Ni^{2+} on the structural conformation and stability of the proteins, *Ef*NaMNAT exhibited a sigmoidal curve that shows the transitions of unfolding in the presence of all the assayed metals and a rightward shift upon the addition of ATP, consequently suggesting an increase in the stability of the protein by the divalent cations. Conversely, the binding of Zn^{2+}, $Cu^{2+,}$ and Ni^{2+} alters the conformation of *Kp*NaMNAT, consequently decreasing the stability of the protein. This is evident in the lack of unfolding transition observed for *Kp*NaMNAT in the presence of Zn^{2+} and Cu^{2+}, as well as the high initial unfolding transition observed for Ni^{2+} (Figure 5.9). At room temperature, Zn^{2+} completely unfolds *Kp*NaMNAT while Cu^{2+} and Ni^{2+} unfold about 70% and 40% of the protein, respectively. This unfolding of *Kp*NaMNAT exposes its hydrophobic pocket, allowing SYPRO Orange dye to access the hydrophobic regions and increases fluorescence intensity. This agrees with the blueshift and the extremely high quantum yield observed in the ANS binding study of *Kp*NaMNAT in the presence of Zn^{2+} and the subsequent high yields for Ni^{2+} and Cu^{2+} as against the low quantum yield for Mg^{2+}. The complete and partial unfolding of *Kp*NaMNAT by Zn^{2+}, $Cu^{2+,}$ and Ni^{2+} allows ANS to access more hydrophobic pockets, resulting in the high fluoresce observed (Figure 5.6). This also explains the low quantum yield observed for *Ef*NaMNAT in the presence of Zn^{2+}, despite the same concentration of protein.

The increasing stability demonstrated by *Ef*NaMNAT compared to *Kp*NaMNAT could be linked to the dimeric nature of the protein (Figure 5.10), given that dimers have larger stabilisation energy compared to monomers due to the inter-subunit interactions (Neet and Timm, 1994; Pollegioni *et al.*, 2003). Additionally, the type of structure in the subunit interfaces contributes to the magnitude of the conformational stability (Neet and Timm, 1994), given that factors such as an increase in the number of hydrogen bonds, helical propensity, ion-pairs, salt bridges, and van der Waals contacts impact protein stability (Gromiha, 2010). *Ef*NaMNAT exhibits a higher percentage of α helix and β-Strand and no unordered coils compared to *Kp*NaMNAT (Table 5.1) (Provencher and Gloeckner, 1981; Sreerama and Woody, 2000), which probably contributed to the increasing stability observed. The replacement of the glycine residue of the "TH/XGH" motif with alanine may adopt a more rigid structure of *Ef*NaMNAT due to reduced conformational flexibility, thus contributing to the stability and T_m of *Ef*NaMNAT (Idiong *et al.*, 2011).

The absence of shift as observed in the melting curves of *Kp*NaMNAT in the presence of the ligands could be an indication of a weak ligand interaction, suggesting that the binding of the ligands (ATP and Mg^{2+}) does not rigidify the protein, hence dynamic. Whereas the ligands are more tightly bound or fixed to *Ef*NaMNAT, which may impact their flexibility or

ability to interact at the active site effectively. Perhaps this is associated with the poor activity observed for *Ef*NaMNAT in the enzyme activity assay (Figure 4.3B).

The purified recombinant *Ef*NaMNAT, as indicated by SDS-PAGE (Figure 3.4) analysis, has a molecular mass of ~26 kDa, which agrees with the projected molecular mass for the amino acid sequence. Albeit SE-HPLC revealed the native molecular mass to be ~40 kDa (Figure 5.10), which exceeds the theoretical subunit mass yet, inconsistent with a dimeric formation. This is no surprise following the inconsistent hexamer formation of archaeal methanocaldococcus jannaschii NMNAT (NadM_MATJA) exhibiting a subunit molecular mass of about 21.5 kDa and a native molecular mass of 72 kDa (Raffaelli *et al.*, 1997; D'Angelo *et al.*, 2000). Also, recombinant hNMNAT1 composed of 32 kDa subunits was crystallised as a homo-hexameric protein (Werner *et al.*, 2002; Zhou *et al.*, 2002), yet the native molecular mass as revealed by gel filtration is suggestive of a tetramer (Emanuelli *et al.*, 1992; Zhou *et al.*, 2002). Besides, studies have shown the possibility of two identical subunits binding and giving rise to "close structure" with an intrinsic symmetry (Mei *et al.*, 2005). Given these, we propose the possibility of the recombinant enzyme *Ef*NaMNAT functioning as a homodimer in solution; thus agreeing with the consistent distinguishable features observed for NaMNATs from Gram-positive bacteria *S. aureus* (*sa*NaMNAT) (*Han et al., 2006*), *B. subtilis*(*bs*NadD) (Olland *et al.*, 2002) and *B. anthracis* (*ba*NaMNAT) (Lu *et al.*, 2008).

On the other hand, *Kp*NaMNAT displayed two distinctive peaks estimated to be ~20 kDa and 50 kDa (Figure 5.10), which are a possible indication that the protein exists both in the monomeric and oligomeric states, respectively. We speculate that *Kp*NaMNAT might exhibit dynamic oligomerisation with the possibility of its monomer subunits dimerising. However, in solution, *Kp*NaMNAT seems to exist and function mainly in the monomeric state, agreeing with previous observations of the quaternary structure of NaMNAT from Gram-negative *E. coli* (NadD) (Mehl *et al.*, 2000; Zhang *et al.*, 2002) and *P. aeruginosa* (Yoon *et al.*, 2005). The likelihood of *Kp*NaMNAT forming a higher oligomeric state upon substrate binding may also exist, similar to *P. aeruginosa* NaMNAT, which forms dimers and tetramers upon purine nucleotide-binding (Yoon *et al.*, 2005). A similar divergence as observed in the native monomeric (~20 kDa) and theoretical subunit mass (~27kDa) of *Kp*NaMNAT was also reported for 6 × His-*Pf*NMNAT (Bathke *et al.*, 2016; Contreras-Rodríguez *et al.*, 2018). However, we presumed that this unique behaviour of *Kp*NaMNAT in SE-HPLC might be due to the hydrodynamic nature of the protein, giving rise to a highly compact globular structure that is retained much longer in the matrix, thus reflecting on the native size of the protein.

Factors such as concentration of the protein, buffer system, pH, and gel matrices may also account for this.

Chapter 6

COMPUTATIONAL MODELLING OF *Kp*NaMNAT

6.1 Introduction

In addition to the empirical studies employed to characterise the biophysical behaviour of recombinant *Kp*NaMNAT and *Ef*NaMNAT, computational modelling was used to complement the empirical studies. In the absence of a crystal structure, the interaction of the ligands within the putative ligandin site of the protein receptor cannot be validated. Therefore, homology modelling was carried out to build a 3D model of the proteins. The reliability of the 3D model was authenticated through Ramachandran plot statistics to analyse the stereochemistry and geometry of the side chains. Next, simulation of the interaction between the 3D model and the ligands (ATP, NMN, and NAD^+) was accomplished via an induced-fit docking (IFD) performed in *Schrödinger* Maestro v12.2 algorithm, which utilises the combination of molecular docking and dynamic protocol in an implicit solvent model, involving the OPLS_2005 force field. Consequently, providing insight into the stabilisation of the ligands, the amino acid residues involved, and if the ligands bind at the same or different sites. Finally, molecular dynamic (MD) simulation was employed to further elucidate the dynamics of the protein when bound and unbound to ligands. The dynamics of the ligands within the receptor site, the impact of Mg^{2+} on the dynamics of the protein, and the substrate dynamics were also evaluated using MD simulation. These were achieved by measuring specific parameters such as the root-means-square-deviation (RMSD) of the protein alpha carbon atoms (Cα), the RMSD of the ligand with respect to protein, the protein side chains, Cα, and ligands root-mean-square-fluctuations (RMSF), the radius of gyration of the protein (Rg) and the solvent-accessible surface area (SASA) of the ligands. MD simulation was performed using Desmond [39e41] MD simulation engine executed in *Schrödinger*.

Due to the unattainability of a reliable 3D model for *Ef*NaMNAT (Figure S6 appendix B), this chapter only focuses on the molecular modelling and MD simulation studies of *Kp*NaMNAT.

6.2 Materials

High end desktop servers (16 CPU Intel® core i7™, 3.3 GHz, 20 M cache), MSI X99 motherboard with 32 GB DDR4-2133 MHz memory and 264 GB RAM, Nvidia GTX 750Ti graphics card, *Schrödinger* Maestro v12.2, and Linux server (2019 GPU-enabled *Schrödinger* Desmond).

6.3 Methods

6.3.1 Homology modelling and validation of *Kp*NaMNAT model

In the absence of the crystal structure of *Kp*NaMNAT, a 3D model was built using its amino acid sequences, which were submitted to SWISS-MODEL (a computerised protein structure homology modelling server) for analogue search. The crystal structure of *E. coli* nicotinic acid mononucleotide adenylyltransferase (SMTL ID: 1k4k.4) (Zhang *et al.*, 2002) with 76% shared sequence identity was used as the template in building the modelled structure. The FASTA sequence and the crystal structure of *E. coli* NaMNAT (*Ec*NaMNAT) were extracted from RCSB Protein Data Bank- PDB entry 1k4k (Zhang *et al.*, 2002) and used to evaluate the *Kp*NaMNAT model further. To validate and access the structural reliability of the predicted *Kp*NaMNAT model, the stereochemistry of the side chains was analysed with a Ramachandran plot, generated via PDBsum. 3D coffee alignment Expresso (T-COFFEE, version 11.00) was used to validate the sequence homology of *Kp*NaMNAT and *Ec*NaMNAT, while the structural alignment was visually analysed and the sequence alignment between the amino acid residues of the templates generated by superimposing predicted *Kp*NaMNAT model on the fourth subunit of *Ec*NaMNAT crystal structure using PyMol.

6.3.2 Protein and ligand preparation

Modelled *Kp*NaMNAT was prepared using the Protein Preparation Wizard module present in the molecular modelling algorithm (Maestro v12.2) for energy minimisation of the structure, which is suitable for further molecular modelling procedures. The following pre-processing was carried out on the protein structure; allocation of bond order, addition of hydrogen atoms, creation of zero bond orders to disulphide bonds and metals, removal of water molecules beyond 5 Å from heterogeneous atoms, and generation of head sticks using Epik module. Optimisation of hydrogen bond assignment was performed at pH 7.0 via PROPKA algorithm by sampling the alignment of water molecules, while water with 0-3 hydrogen bonds was removed. Lastly, the protein structure was modified by minimisation via OPLS_2005 force

field, which places restraints on heavy atoms. The heavy atoms were converged by utilizing a 0.3 Å RMSD cut-off minimisation termination. The stereochemistry of the side chains was examined to verify that no significant change had been induced during preparation of the structure (Pooe *et al.*, 2021). The resulting minimised structure was generated as Maestro (.mae) format for further analysis

Ligand preparation was carried out by obtaining the structure data files (SDF) for ATP (CID 11050836), NMN (CID 14180), and NAD^+ (CID 5892) from PubChem and uploaded to the Ligand Preparation module for energy minimisation via OPLS_2005 force field. The algorithm was programmed to create likely conditions of each ligand at pH 7.0±2 whilst correctly projecting the pK_a of these conditions at the set pH via the Epik module implemented in the algorithm. Desalting of the ligand and generation of probable tautomeric states (~3 ligand tautomer) were performed at pH 7.0±2. Furthermore, certain chiral centres were unaltered, whilst some were altered throughout the ligand preparation period to return chemically sensible structures with low energy states (Pooe *et al.*, 2021). The resulting minimised structures were individually generated as Maestro (.mae) file format for IFD.

6.3.3 Induced fit ligand docking.

Since the binding of ligand induces conformational changes in the configuration of the protein binding site, an induced fit ligand docking was used to gain further insight into the interaction of ATP, NMN, and NAD^+ with *Kp*NaMNAT. The prepared energy minimised ligands saved as Maestro (.mae) files were uploaded to the IFD module, which utilises the combination of dynamic protocol and molecular docking. The standard IFD protocol was utilised on the entire minimised protein structure in an implicit solvent model while using the OPLS_2005 force field. Metal ion and hydrogen bond constraints were introduced to re-docking as well as the initial stages. Ring conformational sampling with an energy window of 2.5 kcal/mol and a penalised non-planar conformation on amide bonds were used in IFD protocol. The van der Waals scaling for both ligand and receptor constraints were conditioned to 0.5 Å with no more than 20 poses per ligand. Residues around 5 Å of ligand poses were further processed by utilising the prime refinement algorithm in Maestro while prime energy was used to grade the processed protein-ligand complexes. The 20 topmost structures, as well as the receptor structures with minimum energy lower than 30 kcal/mol, were submitted for Glide redocking and scoring. Re-docking of each ligand into all the processed low-energy receptor structures was performed with Glide XP using the default settings (Achilonu *et al.*,

2020). The protein-ligand complex with the topmost scoring pose was generated as Maestro (.mae) file for MD simulation.

6.3.4 Molecular dynamic simulation and post-dynamic analysis

Molecular dynamics (MD) simulation was performed with a 2019 GPU-enabled *Schrödinger* Desmond machine. The topmost-scoring pose for each of the protein-ligand complex *Kp*NaMNAT:ATP, *Kp*NaMNAT:NMN, and *Kp*NaMNAT:NAD^+ or the minimised free protein (*Kp*NaMNAT- apo) saved as maestro (.mae) file was submitted to the Ubuntu/Linux operating system (OS) server for MD simulations studies. Preceding MD simulation, the four systems (*Kp*NaMNAT:ATP, *Kp*NaMNAT:NMN, *Kp*NaMNAT:NAD^+, and apo-*Kp*NaMNAT) for simulation were solvated and ionised by utilising the System Builder application module. The solvation of systems involves utilising TIP3P explicit solvent model with OPLS_2005 force field. Each of the systems was positioned in an orthorhombic water box while the distance set between any of the outermost atoms of the protein/ligand from the box boundaries was $a = b = c = 10$ Å. The box volume was minimised, and the system was centralised within the box. Counter ions were introduced to neutralise the system while it was placed 20 Å away from each of the ligands to prevent interaction between them. To determine the effect of Mg^{2+} on the ligand binding, NaCl or $MgCl_2$ (0.15 M) was introduced into the water box to physiologically condition the system. Upon completing the solvation and ionisation phase in the explicit solvent model, the system was submitted for the MD production phase (Achilonu *et al.*, 2020; Pooe *et al.*, 2021).

The MD simulation comprises eight separate phases with different parameters. Phase 1–7 involve equilibration, which contains brief simulation steps. In Phase 1, the parameters and type of the solvated system were detected. In Phase 2, Brownian Dynamics was used to carry out a 100 ps simulation in NVT condition at 10 K with restraints placed on the solute heavy atoms. 12 ps simulation in NVT condition at 10 K with restraints on heavy atoms were applied for phase 3. In phase 4 and 6, 12 ps simulations in NPT conditions at 10 K with restraints on heavy atoms was applied. For phase 5, pocket solvation was excluded while, in stage 7, a 24 ps simulation in NPT conditions at 10 K with no restraints placed on heavy atoms was employed. Stage 8 marked the final MD production phase, and it involved the long-range 100 ns simulation carried out at a constant temperature of 300 K (Achilonu *et al.*, 2020; Pooe *et al.*, 2021).

Following the MD simulation studies, analysis of the resulting trajectories was carried out using *Schrödinger* Maestro v12.2 post dynamically. Basically, four aspects of the data were

analysed. Firstly, the Simulation Quality Analysis algorithm was used to determine the quality of the simulation. This included the mean, the standard deviation, and the slope (ps^{-1}) of the temperature (K), potential energy (kcal/mol), total energy (kcal/mol) and volume ($Å^3$). Secondly, using the Simulation Interaction Diagram algorithm, the RMSD of the Cα atoms of the protein, RMSF of the protein residues as well as of the ligands, RMSD of the ligand with respect to the protein binding site, protein-ligand interaction, and SASA were analysed. Thirdly, the Rg was calculated through the Simulation Events Analysis algorithm, and lastly, the average of a representative cluster was estimated via the Trajectory Clustering algorithm.

6.4 Results

Validation of KpNaMNAT model

As derived from the Swiss Model structural assessment, the predicted 3D model shares 76% sequence identity with the crystal structure of *E. coli* NaMNAT (SMTL ID: 1k4k.4) and has a GMQE (Global Model Quality Estimation) of 0.87 and QMEAN (Qualitative Model Energy Analysis) of 0.51 (Figure S7 appendix B). Analysis of the stereochemistry of the model *Kp*NaMNAT side chains via Ramachandran plot statistics as generated from PDBsum showed the distribution of 172 residues (94%) within the most favour region, 11 residues (6%) within the allowed region, and no residue (0%) in the disallowed regions (Figure 6.1, and Table 6.1).

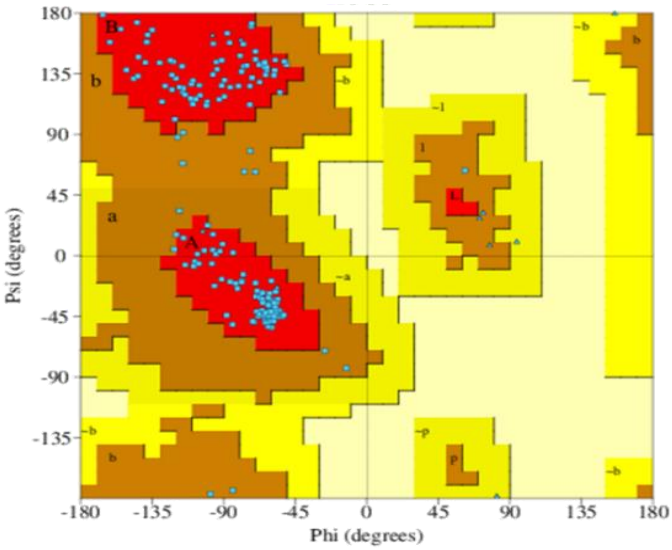

Figure 6.1. Ramachandran plot for model *Kp*NaMNAT as derived from PDBsum.
172 residues (94%) are within the most favour region, 11 residues (6%) are in the allowed region, and no residue (0%) is in the disallowed regions. Glycine and Proline residues were 10 and 17, respectively. The overall average G-Factor of the structure was measured as -0.10 (values < -0.5 are unusual structures).

Table 6.1. PROCHECK summary (Ramachandra plot statistics) for model *Kp*NaMNAT.

	No. of residues	%
Most favoured regions	172	94
Additional allowed regions	11	6
Generously allowed regions	0	0
Disallowed regions	0	0
Non-glycine and non-proline residues	183	100

Also, the validation of the homology sequence alignment of *Kp*NaMNAT and *Ec*NaMNAT by T-Coffee produced a good sequence alignment result with a score of 100 (Figure 6.2). Visual analysis of the superimposed structures, as seen in Figure 6.3, showed both *Ec*NaMNAT and the predicted *Kp*NaMNAT structures to be closely related. Moreover, the RMSD between the 201 amino acid residues of the two structures when aligned using PyMol is 0.082 Å.

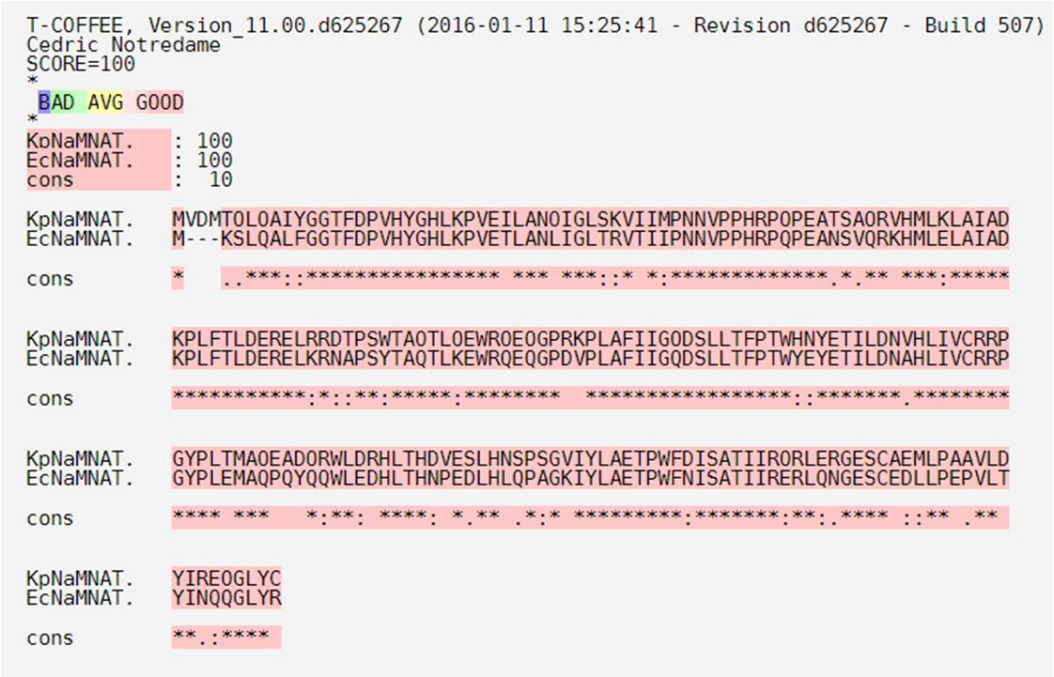

Figure 6.2. Sequence alignment of *Kp*NaMNAT and *Ec*NaMNAT as produced by T-Coffee.
The absence of blue, green, or yellow marks indicates a good sequence alignment.

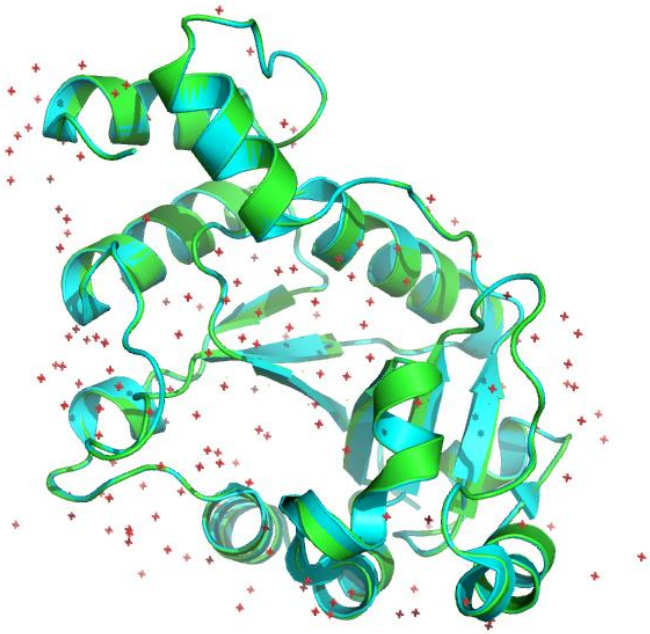

Figure 6.3. Structural alignment of *Kp*NaMNAT and *Ec*NaMNAT.
*Kp*NaMNAT is represented as a cartoon structure in Cyan while *Ec*NaMNAT is depicted as green. The red dots represent water molecules from the *Ec*NaMNAT crystal structure. The RMSD between the two structures, when superimposed on each other using PyMol, is 0.082 Å over 201 residues.

Ligand docking

Results of the IFD between the *Kp*NaMNAT receptor and all three ligands, ATP, NMN, and NAD^+, generated 13, 19, and 14 docking poses, respectively. The topmost docking pose for each ligand selected and submitted for MD simulation is shown in Figure 6.4. Table 6.2 presents the docking scores, glide gscore, emodel energy, and the IFD score of the topmost pose generated for each *Kp*NaMNAT receptor-ligand complex. The resulting negative emodel energy and glide scores project that the protein-ligand interaction proceeds exergonically. Overall, the poses revealed ATP, NMN, and NAD^+ to bind on the same site within the *Kp*NaMNAT receptor.

As revealed from the 2D molecular interaction plot of the IFD (Figure 6.4), the contact between the amino acid side chains (not more than 4 Å away from the ligand) and the ligands were stabilised mostly through van der Waals and H-bonding. ATP binding was stabilised by a π- π∗ interaction between Tyr11 and the adenine moiety couple with eight hydrogen bond contacts between Arg137, Asp112, Ile108, Gly12, Gly21, Phe180, Ile182, and ATP. Overall, 18 amino acid residues including three glycines, nine non-polar, four polar, and two charged amino acids were within 4 Å of ATP and possibly contributed to stabilising the ligand inside the receptor. The interaction between *Kp*NaMNAT and NMN involved four glycines, nine non-

polar, five polar, and one negatively charged amino acid residues. This NMN interaction was stabilised by a π- π∗ interaction between Hie22 and pyridine ring, in addition to six hydrogen bond contacts between Ile182, Gly21, His22, Phe15, Thr14, and Gly12 side chains. The side chains involved in the interaction of NAD^+ binding to *Kp*NaMNAT were 31 residues, majority were non-polar, ten were polar, four glycine residues, and one negatively charged residue. Stabilisation of this interaction involves a π- π∗ and a π-Cation interaction between Trp179 and pyridine ring, in addition to seven hydrogen bond interactions between Phe15, Thr14, Ser86, Asn44, Ser183, Ile182, and NAD^+.

Table 6.2. Details of the topmost poses generated for each *Kp*NaMNAT - ligand complex based on their induced-fit docking.

Protein receptor-ligand complex	Docking score (kcal/mol)	Glide gscore (kcal/mol)	Glide emodel (kcal/mol)	Glide energy (kcal/mol)	IFDScore (kcal/mol)
*Kp*NaMNAT:ATP	-8.027	-8.027	-98.225	-66.143	-477.550
*Kp*NaMNAT:NMN	-7.718	-7.718	-77.378	-50.636	-473.200
*Kp*NaMNAT:NAD^+	-10.975	-10.975	-130.125	-79.550	-481.080

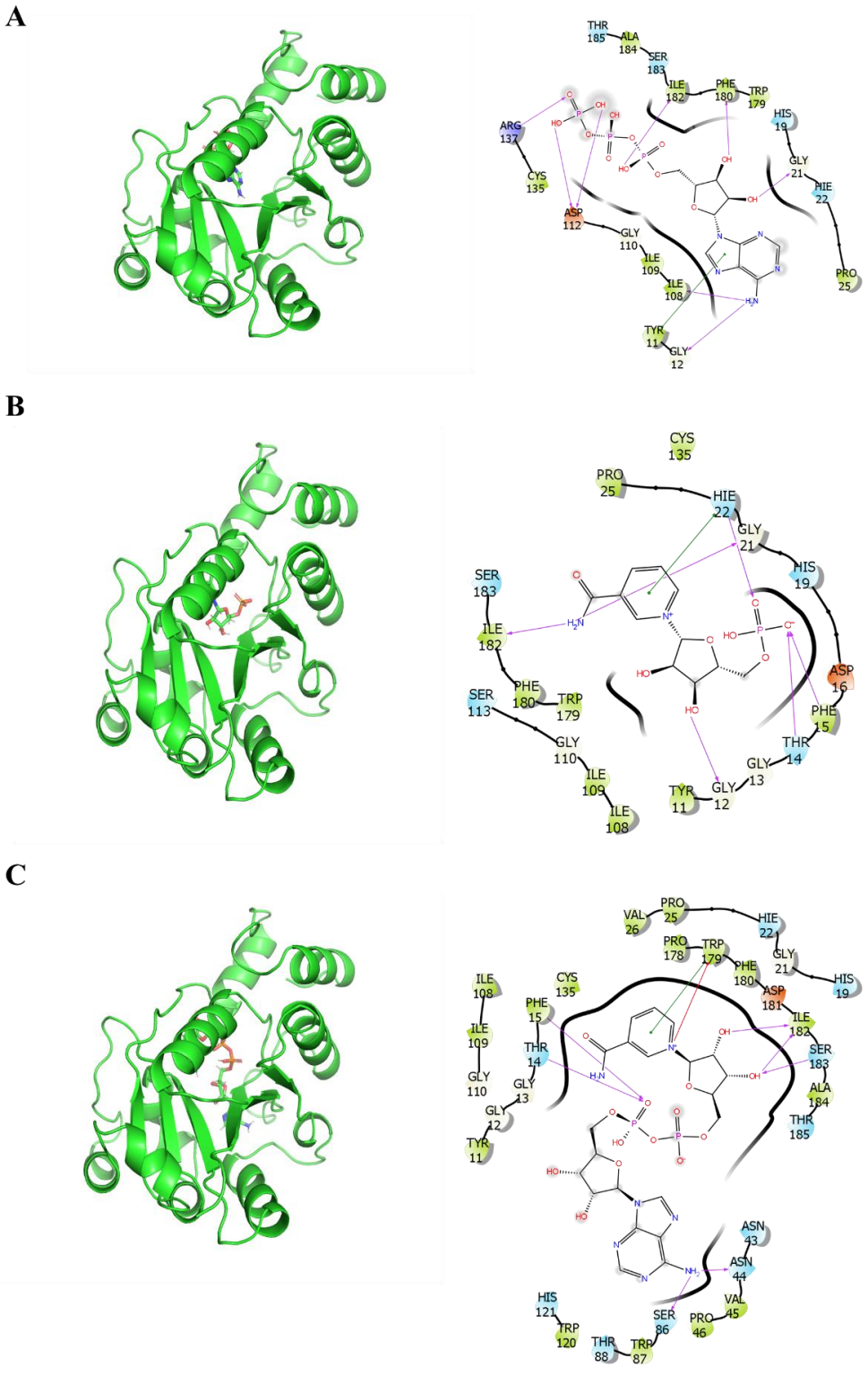

Figure 6.4. Ribbon representation versus 2-dimensional interaction plot of the induced-fit docking.
(A) *Kp*NaMNAT:ATP complex, **(B)** *Kp*NaMNAT:NMN complex, and **(C)** *Kp*NaMNAT:NAD^+ complex. The ligands are shown in stick representation. The amino acid residues are within 4 Å from the ligand and are represented as follows: blue is polar, green is non-polar, orange is negatively charged, and violet is positively charged. The hydrogen bond is represented as purple lines, salt bridge interactions as blue-red lines, green lines represent π- π∗ interaction, while exposure to solvent is indicated in gray. The ribbon representation was generated using PyMol, while the 2-D images were produced from the Maestro 2D interaction diagram.

Molecular dynamics simulation

To effectively assess the stability of the interaction between the enzyme and the ligands, MD simulation was performed. As derived from the System Builder module, Figure 6.5 shows the solvation and ionisation of the systems in an orthorhombic water box. The quality across all four simulated systems as generated from the Simulation Quality Analysis algorithm is indicated in Table 6.3. In all, the temperature, potential energy, volume, and total energy of the simulated systems were stable during the 100 ns simulation time with the average slope as ±0.001 unit/ps, thus indicating proper equilibration of the systems.

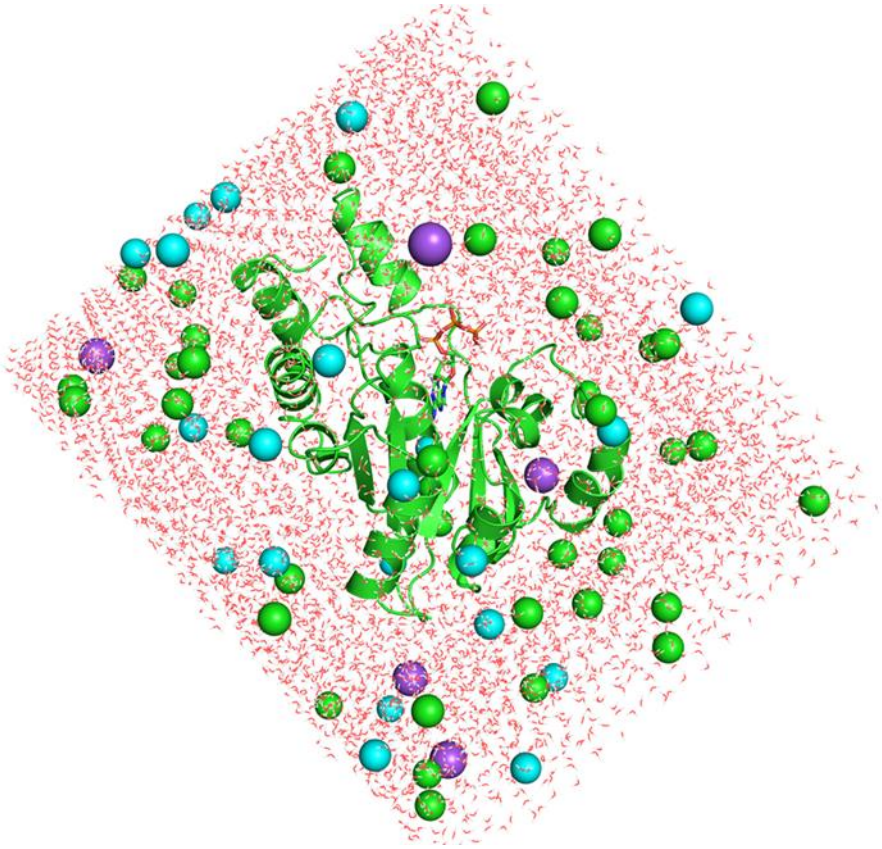

Figure 6.5. Ribbon representation of *Kp*NaMNAT protein in orthorhombic water box bound to ATP in the presence of Mg^{2+}.
The solvation and ionisation of the system involved using the TIP3P explicit solvent model with the OPLS_2005 force field. The balls in green depict Cl, cyan represent Mg^{2+}, Purple represents Na, the water molecules are shown in red, while the ligand is shown in stick. The distance between the outermost atom of the protein/ligand from the box boundaries is a = b = c = 10 Å.

Table 6.3. The simulation quality analysis of the four systems showing the mean, standard deviation (SD), and slopes of total energy (Et), Potential energy (Ep), temperature, and volume of the systems over the 100 ns simulation time.

		No Mg^{2+}			Mg^{2+}		
Simulated System	**Parameters**	**Mean**	**±SD**	**Slope (ps^{-1})**	**Mean**	**±SD**	**Slope (ps^{-1})**
***Kp*NaMNAT-Apo**	Et (kcal/mol)	-68588.8	99.70	0.000	-78526.9	100.75	0.000
	Ep (kcal/mol)	-84334.0	76.99	0.000	-94299.7	76.98	0.000
	T (K)	298.7	0.83	0.000	298.7	0.84	0.000
	V ($Å^3$)	255568.0	321.65	0.001	255259.1	325.19	0.001
***Kp*NaMNAT:ATP**	Et (kcal/mol)	-68736.4	101.04	0.000	78506.8	99.45	0.000
	Ep (kcal/mol)	-84535.3	77.33	0.000	94297.4	75.78	0.000
	T (K)	298.7	0.83	0.000	298.7	0.83	0.000
	V ($Å^3$)	256209.4	319.20	0.000	255402.6	319.12	0.001
***Kp*NaMNAT:NMN**	Et (kcal/mol)	-68842.2	101.24	0.000	-78668.2	102.29	-0.001
	Ep (kcal/mol)	-84628.8	77.06	0.000	-94455.0	78.94	-0.001
	T (K)	298.7	0.84	0.000	298.8	0.84	0.000
	V ($Å^3$)	256062	324.6	0.001	255310.6	320.11	-0.001
***Kp*NaMNAT:NAD^+**	Et (kcal/mol)	-68794.3	101.91	0.000	-78562.1	102.94	-0.001
	Ep (kcal/mol)	-84607.8	78.60	0.000	-94368.5	79.53	-0.001
	T (K)	298.7	0.83	0.000	298.7	0.84	0.000
	V ($Å^3$)	256309.8	323.25	-0.001	255682.1	316.03	0.001

As derived using the Simulation Interaction Diagram algorithm, the structural stability or fluctuations of each complex were measured through the RMSD and the RMSF. The Cα RMSD measures the average change in the displacement of the Cα atoms for a particular frame with respect to a reference frame; this was calculated for all frames in the trajectory (Figure 6.6). The overall average value of all frames in the trajectory in the absence of Mg^{2+} is 1.68±0.18 Å for KpNaMNAT-apo, 1.66±0.14 Å for *Kp*NaMNAT:ATP, 1.90±0.25 Å for *Kp*NaMNAT:NMN and 1.91±0.30 Å for *Kp*NaMNAT:NAD^+. The protein-ligand complexes in comparison to *Kp*NaMNAT-apo showed a comparable Cα RMSD within the 100 ns simulation time. In the presence of Mg^{2+}, the overall average value of all frames in the trajectory is 1.77±0.24 Å (KpNaMNAT-apo), 2.77±0.77 Å (*Kp*NaMNAT:ATP), 2.23±0.29 Å (*Kp*NaMNAT:NMN) and 2.21±0.27 Å (*Kp*NaMNAT:NAD^+). These are summarised in Table 6.4. The Cα RMSD of the protein-ligand complexes in the presence of Mg^{2+} is comparable to the *Kp*NaMNAT- apo, even though *Kp*NaMNAT:ATP complex system showed deviation or fluctuation after about 45 ns. However, this fluctuation change is within 3 Å and stabilises within a fixed value at the end of the simulation. Fluctuations of the order of 1–3 Å are

completely acceptable for small globular proteins whereas, fluctuations much larger than that indicate that the protein is undergoing a large conformational change during the simulation. Overall, the RMSD values for all the systems converge around a fixed value suggesting that the system was equilibrated, and the data generated suitable for further analysis (Figure 6.6).

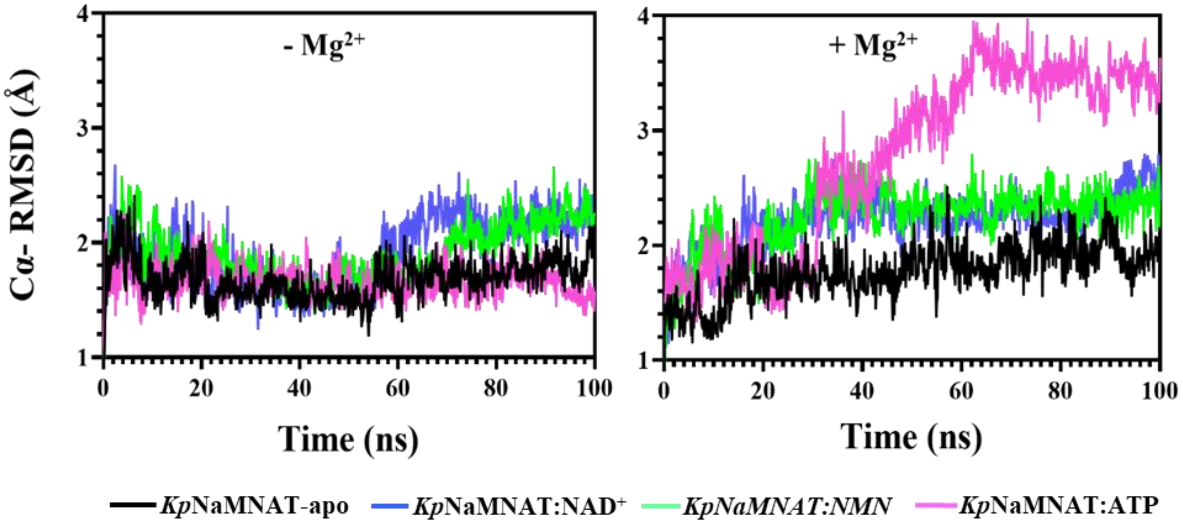

Figure 6.6. The root-mean-square deviation (RMSD) of the Cα atoms of *Kp*NaMNAT over 100 ns simulation time.
Analysis of *Kp*NaMNAT-apo and *Kp*NaMNAT:ligand complexes in the absence ($-Mg^{2+}$) and presence of magnesium ion ($+Mg^{2+}$). The fluctuation change for all protein-ligand complex is within 3 Å and stabilises within a fixed value at the end of the simulation.

Table 6.4. The overall RMSD average of all frames in the trajectory in the absence and presence of Mg^{2+}.

System	No Mg^{2+}	Mg^{2+}
	Å±SD	
*Kp*NaMNAT-apo	1.68±0.18	1.77±0.24
*Kp*NaMNAT:ATP	1.66±0.14	2.77±0.77
*Kp*NaMNAT:NMN	1.90±0.25	2.23±0.29
*Kp*NaMNAT:NAD^+	1.91±0.30	2.21±0.27

The protein RMSF is a valuable tool for characterising changes limited to the protein side chains. It evaluates the flexibility of the protein structure: the extent of the displacement of a particular atom or group of atoms in relation to its structure. Figure 6.7 shows the RMSF of the Cα atoms and the side chains of the protein residues for the four simulated systems in the absence and presence of Mg^{2+}, based on the 100 ns trajectory data. The results obtained in the absence of Mg^{2+} show that the side-chain fluctuations across the four systems are

comparable. No major side chain perturbation or deviation was observed in the receptor of the apo-structure upon ligand binding. However, in the presence of Mg^{2+}, the side chains of the *Kp*NaMNAT:ATP complex, fluctuated the most in comparison with the apo-protein, while the other two complexes *Kp*NaMNAT:NMN and *Kp*NaMNAT:NAD^+ showed subtle differences in the amino acid side chain RMSF, in relation to *Kp*NaMNAT-apo. The major fluctuations as observed in the *Kp*NaMNAT-ATP complex were within regions 113–118 and 140–151 residues with peaks at residues 148, 144, 141, 114, 116, 117, and 151, which corresponds to Ala, Met, Pro, Leu, Thr, Phe, and Arg amino acid residues, respectively. Peaks are an indication of regions of the protein with the most fluctuation during the simulation. The results obtained for the Cα RMSF and the side chains RMSF of the protein residues both in the presence and absence of Mg^{2+} are comparable.

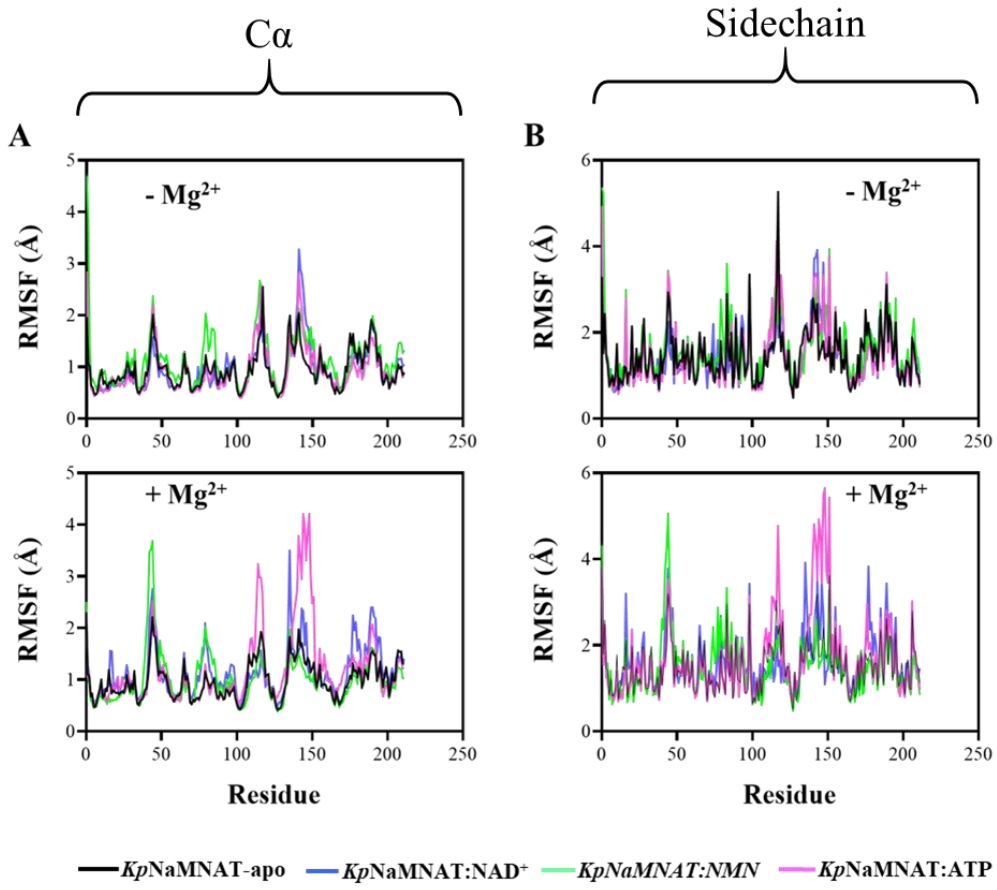

Figure 6.7. The root-mean-square fluctuation (RMSF) of the Cα atoms vs the side chains of the protein residues over 100 ns simulation time for *Kp*NaMNAT.
*Kp*NaMNAT-apo and *Kp*NaMNAT:ligand complexes in the absence ($-Mg^{2+}$) and presence of magnesium ion ($+Mg^{2+}$). In the absence of Mg^{2+}, no major side chain perturbation or deviation was observed upon ligand binding. However, in the presence of Mg^{2+}, the side chains of the *Kp*NaMNAT:ATP complex fluctuated the most, as observed within regions 113–118 and 140–151 residues. The results obtained for the Cα RMSF versus the side chains RMSF of the protein residues are comparable.

Another important parameter derived from the MD simulation is the Rg of the Cα atoms of *Kp*NaMNAT-apo and the *Kp*NaMNAT-ligand complexes, calculated using the Simulation Events Analysis algorithm. The Rg of a protein measures the compactness of the protein. The lower the Rg, the more compact it is and the higher the Rg, the less compact it is (Lobanov *et al.*, 2008). Figure 6.8 indicates the Rg for the four simulated systems over 100 ns MD simulation time. The average Rg is summarised in Table 6.5. The Rg profile of *Kp*NaMNAT:ATP in the presence of Mg^{2+} showed a massive divergence from the average Rg after 40 ns. Overall, except for *Kp*NaMNAT:ATP complex in the presence of Mg^{2+}, the Rg of the other simulated systems are comparable both in the absence and presence of Mg^{2+} because there was no substantial divergence from the average Rg during the 100 ns simulation time.

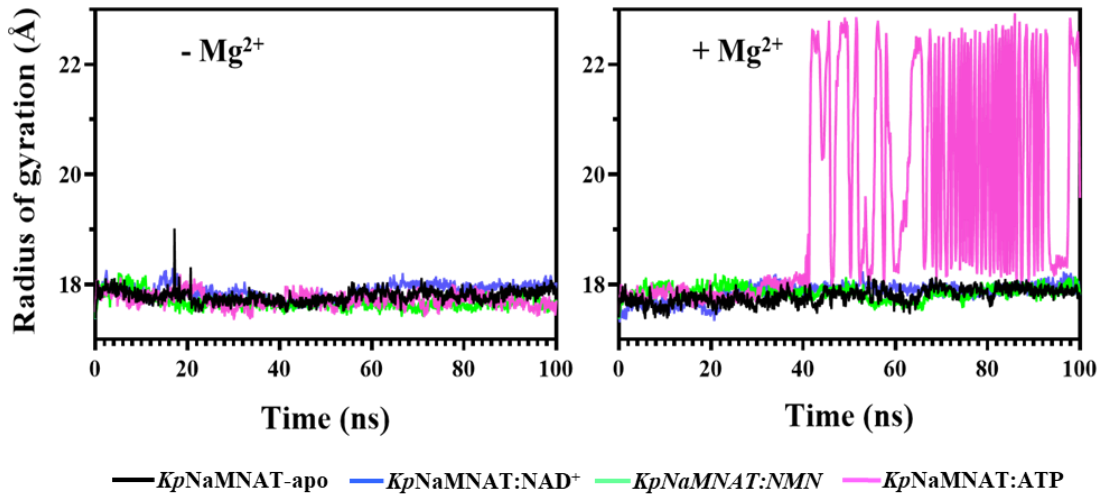

Figure 6.8. The radius of gyration (Rg) of the Cα atoms of *Kp*NaMNAT
*Kp*NaMNAT-apo (black), *Kp*NaMNAT:ATP complex (Purple), *Kp*NaMNAT:NMN complex (green), and *Kp*NaMNAT:NAD^+ complex (blue), in the absence ($-Mg^{2+}$) and presence of magnesium ion ($+Mg^{2+}$) over 100 ns simulation time. The Rg across the simulated systems are comparable, except for *Kp*NaMNAT:ATP complex in the presence of Mg^{2+}, which showed a massive deviation from the mean Rg after 40 ns.

Table 6.5. The radius of gyration of the four systems in the absence and presence of Mg^{2+}

System	No Mg^{2+}	Mg^{2+}
	Å±SD	
KpNaMNAT-apo	17.79±0.11	17.79±0.13
KpNaMNAT:ATP	17.73±0.12	19.37±1.82
KpNaMNAT:NMN	17.67±0.13	17.85±0.11
KpNaMNAT:NAD+	17.87±0.14	17.85±0.16

To gain further insight into the stability of the respective *Kp*NaMNAT-ligand complexes, the conformational dynamics of the ligands within the protein binding site and their interactions with the protein and the environment were examined. Using the ligand RMSD with regards to the protein, the internal changes of the ligand atoms were measured. The result obtained, as seen in the plot of ligand RMSD (Å) against 100 ns simulation time (Figure 6.9), showed an increasing fluctuation with ATP compared to NMN and NAD^+. The fluctuations observed in ATP was much higher in the presence of Mg^{2+} compared to when Mg^{2+} is absent. In the absence of Mg^{2+}, ATP (in comparison with NMN and NAD^+) demonstrates increasing fluctuation within the first 60 ns of the simulation. Thereafter, a sudden increase in the RMSD was observed, which then stabilised within the binding site in the last 40 ns of the simulation time. On the other hand, ATP in the presence of Mg^{2+} demonstrates an increasing fluctuation all through the 100 ns simulation time. Overall, ATP diffused away from its initial binding position. However, NMN only fluctuated within 10 ns of the simulation time and stabilised for the remaining 90 ns of the simulation time, while NAD^+ converged and stabilised between 35 and 100 ns.

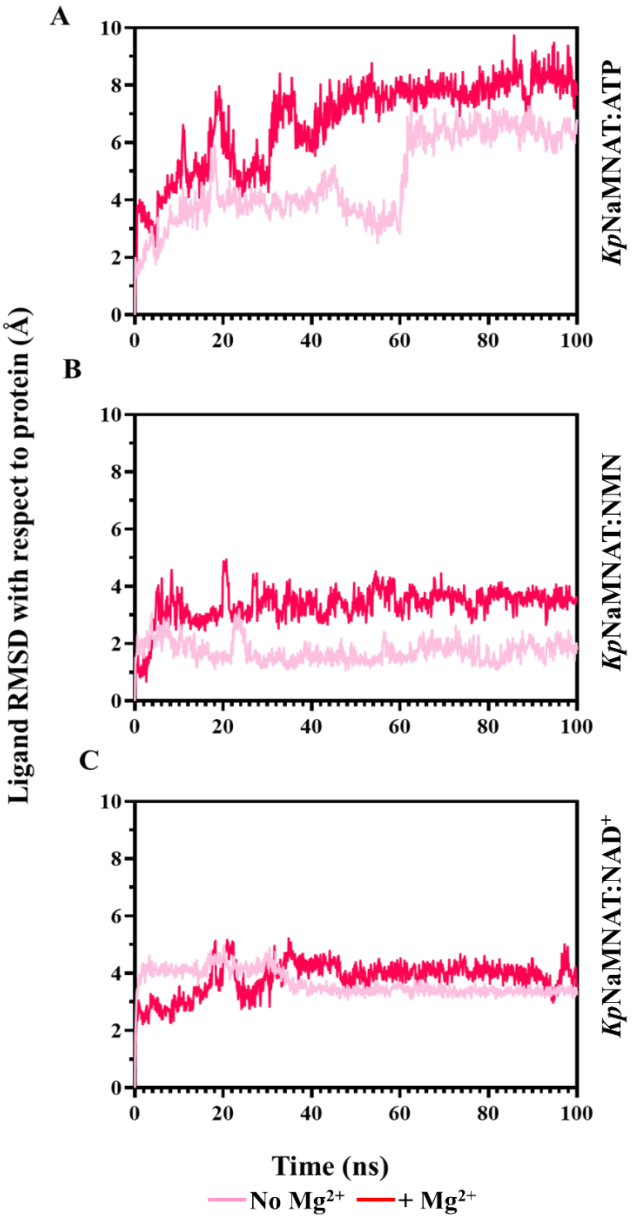

Figure 6.9. The root-mean-square deviation (RMSD) of the ligands with respect to *Kp*NaMNAT protein over a 100 ns simulation time.
(A) *Kp*NaMNAT:ATP complex **(B)** *Kp*NaMNAT:NMN complex and **(C)** *Kp*NaMNAT:NAD^+ complex. The pink profile indicates the absence of Mg^{2+} while the red profile indicates the presence of Mg^{2+}. Amongst all three ligands, ATP fluctuated the most both in the absence and presence of Mg^{2+}, while NMN and NAD^+ appear more stable within the protein receptor.

Furthermore, the interaction of the ligand with the protein entropic role in binding event was monitored using RMSF of individual atoms in the ligands with respect to the protein receptor. As shown in Figure 6.10, ATP atoms demonstrated the highest average RMSF value compared to the other ligands both in the absence (2.90±0.39 Å) and presence (2.60±0.52 Å) of Mg^{2+}, followed by NAD^+ (1.14±0.51 and 1.68±0.48 Å) and then NMN (1.17±0.16 and 1.23±0.37 Å).

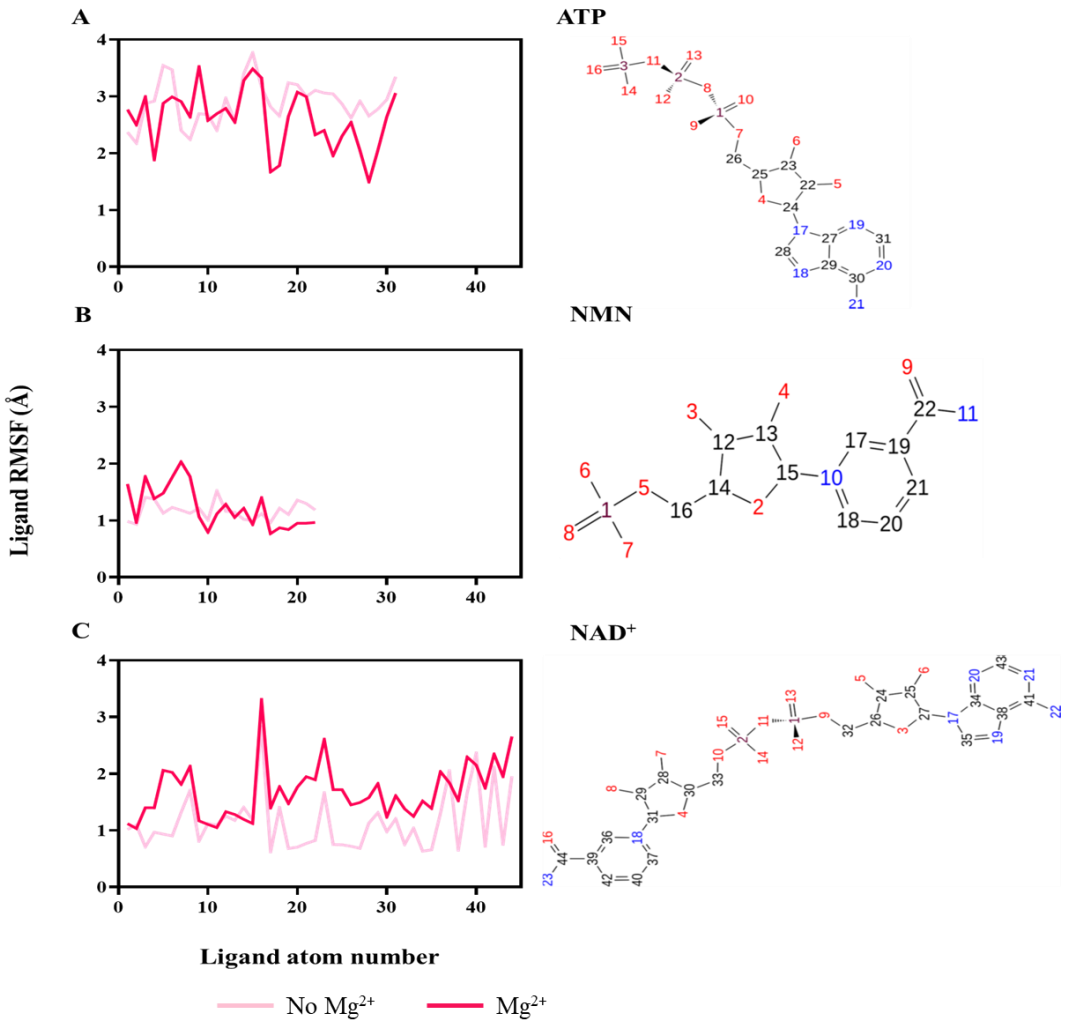

Figure 6.10. The root-mean-square fluctuation (RMSF) of the ligands
(A)ATP **(B)**NMN and **(C)**NAD^+ with respect to the protein, throughout 100 ns simulation time. The pink profile indicates the absence of Mg^{2+}, while the red profile indicates the presence of Mg^{2+}. ATP ligand demonstrated the highest average RMSF value compared to the other ligands both in the absence (2.90±0.39 Å) and presence (2.60±0.52 Å) of Mg^{2+}, followed by NAD and then NMN.

Examination of the SASA of the ligands (Figure 6.11) revealed ATP to exhibit the largest SASA value both in the absence and presence of Mg^{2+} (203.61±33.72 and 211.00±44.28 $Å^2$ respectively), followed by NAD^+ (106.66±45.44 and 176.60±38.83 $Å^2$ respectively), while NMN had the lowest SASA (103.95±22.99 and 141.69±29.28 $Å^2$ respectively). Overall, the average SASA of all three ligands increased with Mg^{2+}. However, the deviation observed for NAD^+ in the presence of Mg^{2+} was massive.

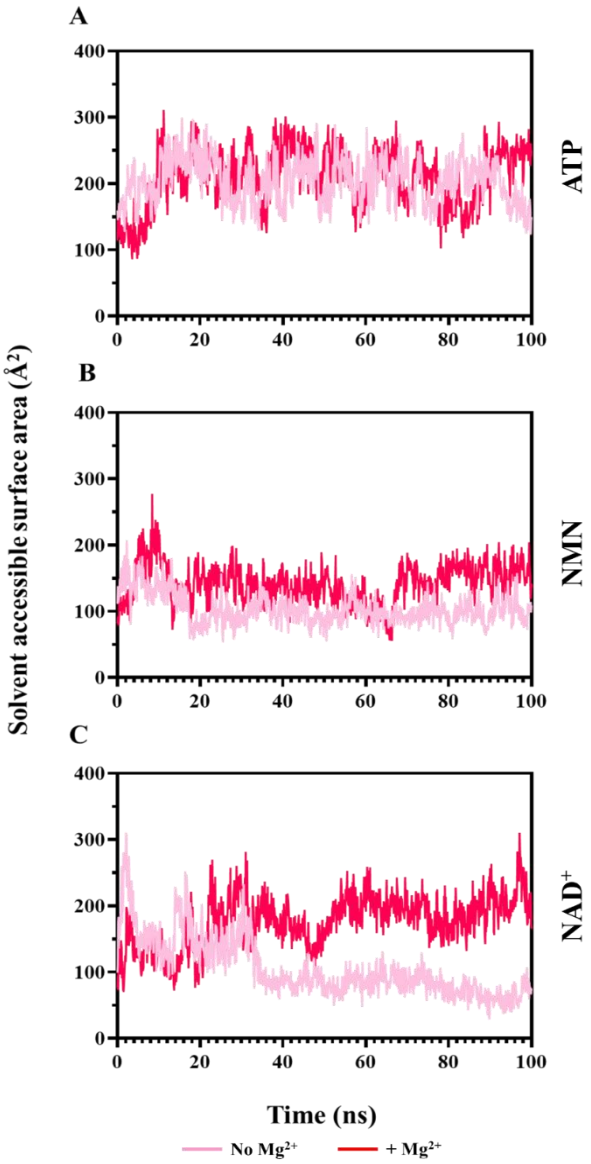

Figure 6.11. The solvent-accessible surface area (SASA) of ligands with respect to *Kp*NaMNAT.
(A)ATP **(B)**NMN and **(C)**NAD^+ throughout 100 ns simulation time. The pink profile indicates the absence of Mg^{2+}, while the red profile indicates the presence of Mg^{2+}. ATP exhibit the largest average SASA both in the absence and presence of Mg^{2+} (203.61±33.72 and 211.00±44.28 $Å^2$ respectively), followed by NAD^+ (106.66±45.44 and 176.60±38.83 $Å^2$ respectively), while NMN had the lowest SASA (103.95±22.99 and 141.69±29.28 $Å^2$ respectively). The average SASA of all three ligands increases with Mg^{2+}.

In addition to the conformational dynamics of the ligands within the protein receptor, the ligand interaction with the protein side chains was examined. Figure 6.12 shows the type of interactions that stabilise the ligands within the binding site with regards to the 100 ns simulation time. As seen from the stacked bar charts, most interactions between the ligands and the protein active site residues, both in the absence and presence of Mg^{2+} are hydrogen bonds, van der Waals, and water bridge. An increased ionic interaction was also observed in the presence of Mg^{2+} for all ligands.

A

- Mg^{2+}

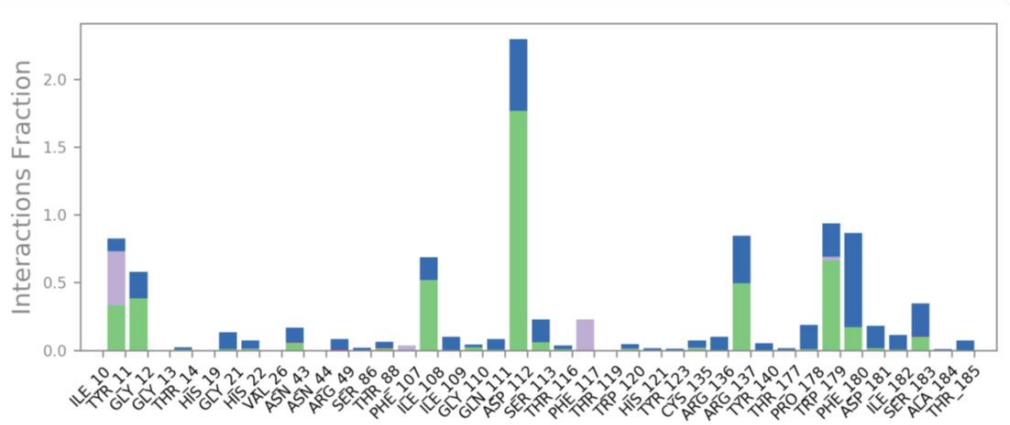

+ Mg^{2+}

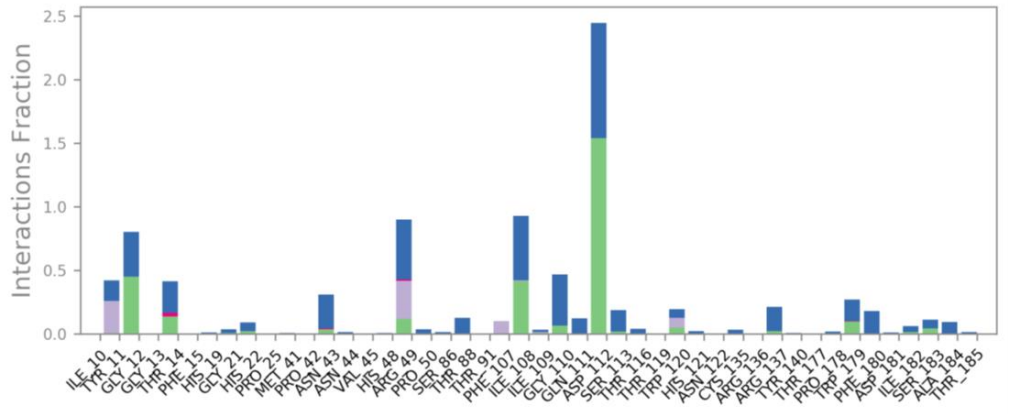

B

- Mg^{2+}

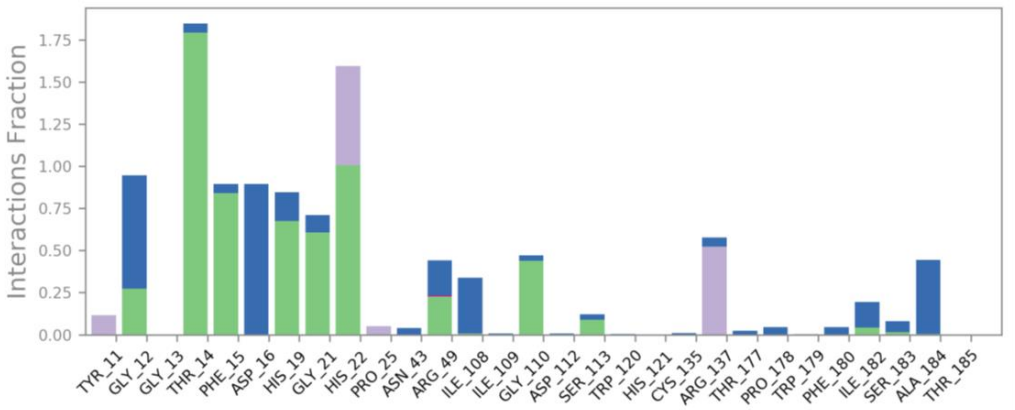

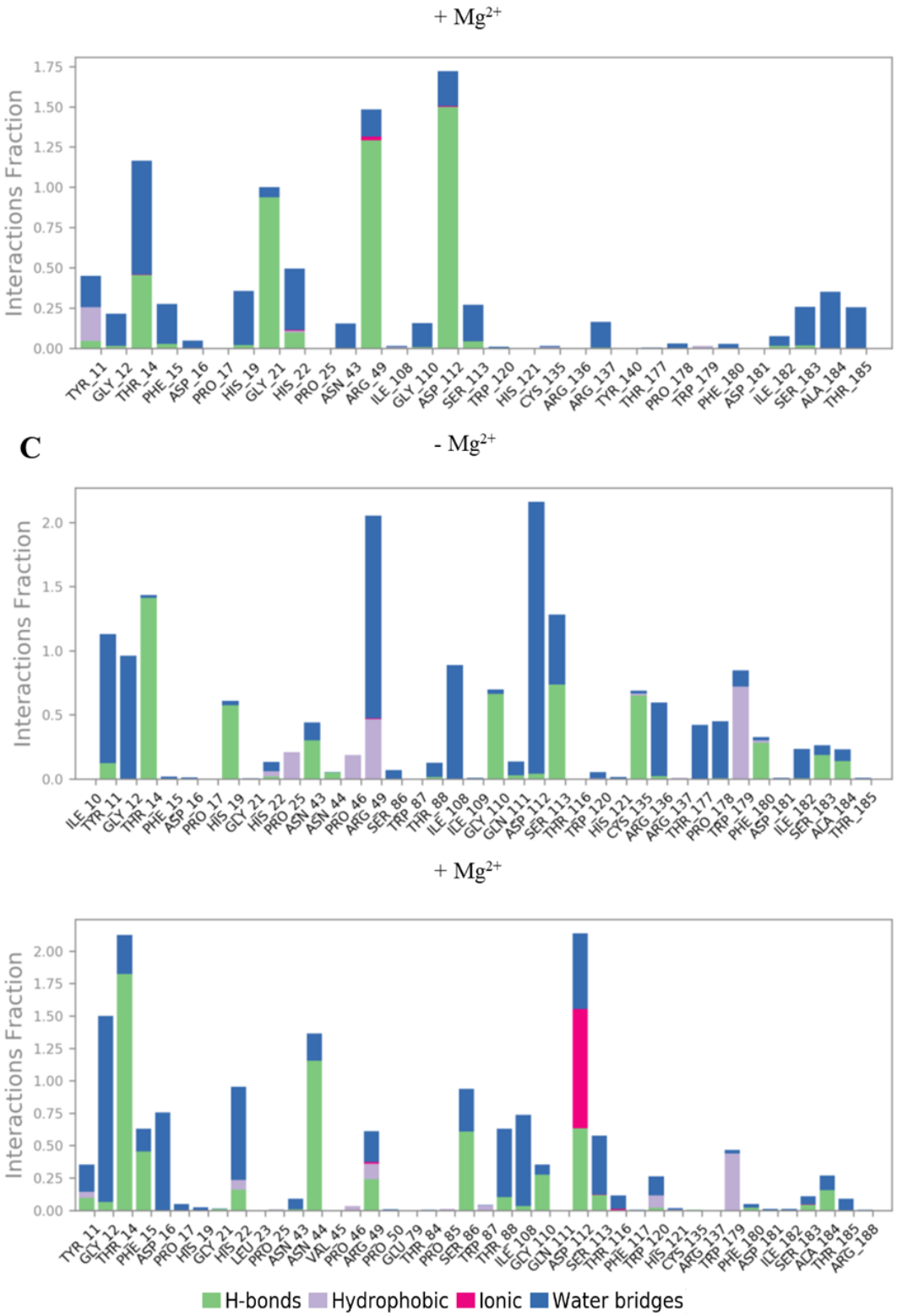

Figure 6.12. Stacked bar charts of side-chain interactions and the types of interaction between *Kp*NaMNAT and ligands.

(A) ATP, (B) NMN, and (C) NAD^+, in the absence ($-Mg^{2+}$) and presence ($+Mg^{2+}$) of magnesium ion over a 100 ns simulation period. The image was captured via the ligand interaction algorithm implemented in Maestro v12.2.

Lastly, based on Trajectory Clustering, the results obtained (Figure 6.13) showed that the ligands are stabilised through a combination of salt bridges, hydrogen bonds, polar contact, hydrophobic interaction, water bridge interactions between the ligand and the amino acid side chains in addition to water molecules within 4 Å of the ligand. ATP in the absence of Mg^{2+} was stabilised by a π- π∗ between Tyr11 and the adenine ring, as well as 22 hydrogen bond interaction with water molecules and amino acid residues. Whereas in the presence of Mg^{2+}, the amount of hydrogen bond contacts decreased to 7, in addition to 2 π-cation interactions between Arg49 and the adenine rings. NMN in the absence of Mg^{2+} was stabilised by a π-cation interaction between Hie22 and the pyridine ring, coupled with 15 hydrogen bond contacts with water molecules and amino acid side chains. The amount of hydrogen bond contacts in the presence of Mg^{2+} also decreased to three, making contact with only one water molecule, Asp112, and Gly21. A salt bridge contact between Arg49 and the phosphate group was also observed. Conversely, NAD in the absence of Mg^{2+} was stabilised by a π-cation interaction between Arg49 and the adenine ring, in addition to 10 hydrogen bond contacts with water molecules and amino acid side chains. However, in the presence of Mg^{2+}, this hydrogen bond contacts doubled to 20 hydrogen bonds, coupled with a salt bridge contact with Asp112. Overall, the amount of Hydrogen bonds and water bridge contacts made by ATP and NMN decreases with the presence of Mg^{2+}, whereas NAD^{+} showed an increase in both hydrogen bonds and water bridge contacts in the presence of Mg^{2+} during the 100 ns MD simulation.

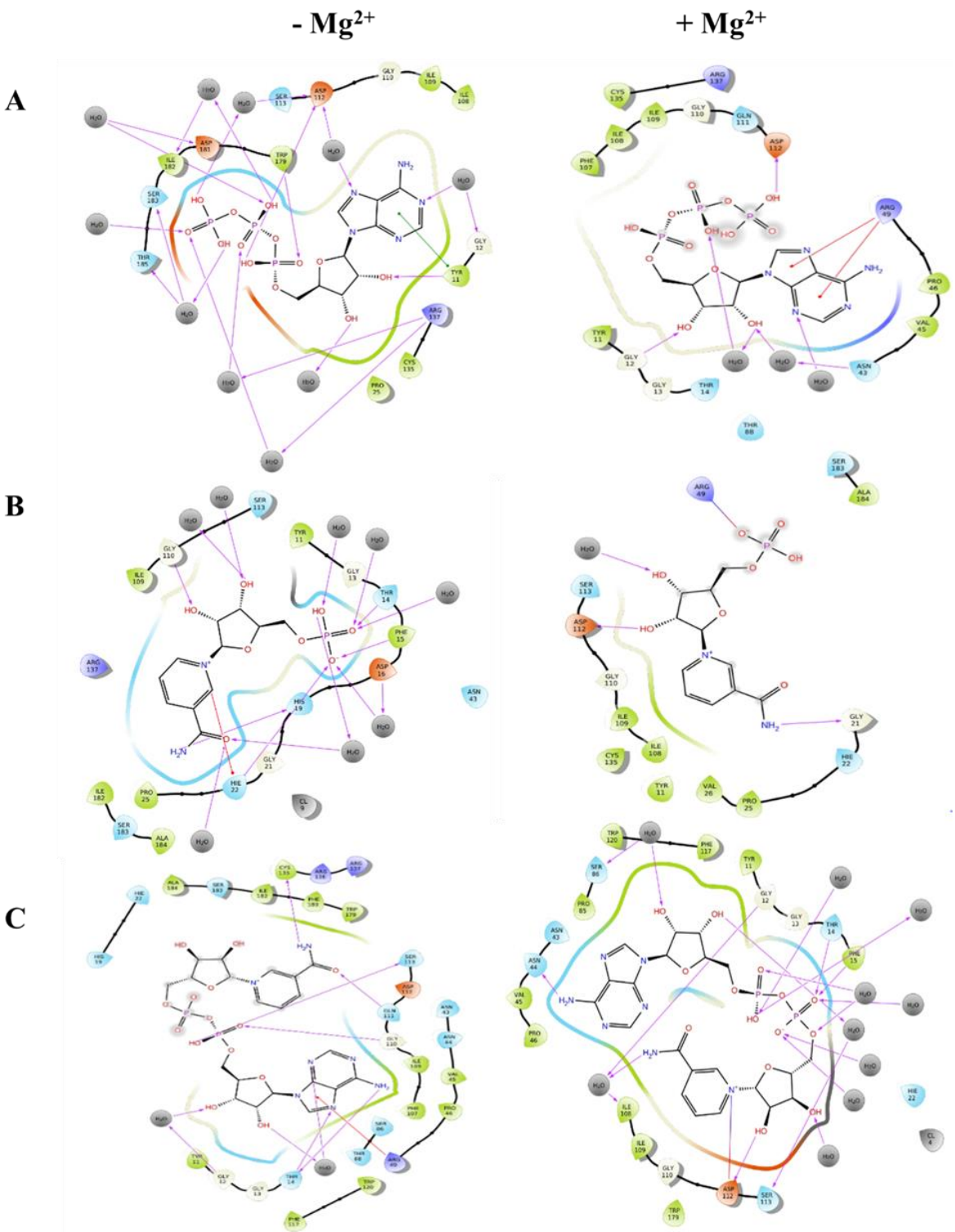

Figure 6.13. 2D interaction plot showing clusters of trajectory frames based on the RMSD of most dormant screenshots of *Kp*NaMNAT complex.

(A) *Kp*NaMNAT:ATP complex, **(B)** *Kp*NaMNAT:NMN complex, and **(C)** *Kp*NaMNAT:NAD^+ complex in the absence and presence of Mg^{2+}. The side chain residues are no more than 4 Å from the ligand and are indicated as: blue is polar, green is non-polar, orange is negatively charged, and violet is positively charged. The hydrogen bond is represented as purple lines, salt bridge interactions as blue-red lines, green lines represent π-π∗ interaction, while grey shades indicate exposure to solvent. The images were captured using Maestro 2D interaction diagram.

6.5 Discussion

In the past, molecular modelling has proven to be a helpful tool in describing and complementing experimental studies. Hence, computational modelling was employed in this study. A 3D model of *Kp*NaMNAT structure was generated using *Ec*NaMNAT (1k4k.4) as a template (Zhang *et al.*, 2002). The modelled structure was validated, and the reliability of the structure access via Ramachandra plot statistics revealed 94% of the side chains in the most favoured regions. As derived from the analysis of 118 structures of *R*-factor no more than 20.0 and resolution of not less than 2.0 Å, a quality model is expected to have more than 90% residues in the most favoured regions (Ramachandran *et al.*, 1963). In addition to the Ramachandra plot, analysis of the sequence homology via T-Coffee indicates a high level of the similarity of amino acids between the modelled structure and *Ec*NaMNAT (1k4k.4) sequence (Figure 6.2). As seen from the structural alignment, the sequence of the two amino acids showed a high level of conservation (Figure 6.3). This was further supported by the RMSD of 0.082 Å obtained from the sequence alignment between the amino acid residues of the modelled structure and *Ec*NaMNAT (1k4k.4), which is a very low deviation in structure. Taking together these findings, the quality of the modelled 3D structure used in this study can be validated and ascertained as being reliable to be used to make rational inferences.

Based on the induced-fit docking as shown in the three-dimensional interaction plot of the top poses corresponding to the protein-ligand complexes (shown in Figure 5.5), it is apparent that the three ligands (ATP, NMN and NAD^+) bind at the same active site because no other site in the *Kp*NaMNAT protein attracted the ligands. Although NAD^+ binds in such a way that it appears to extend into a neighbouring cleft, which possibly explains the reason for the much lower fluorescence intensity of ANS in the presence of NAD^+ as observed in Figure 5.2 since more ANS might be displaced.

It is evident that the interaction of the side chain residues with the phosphate group of the ligands as observed between ATP and residues Arg137 and Asp112, NMN with residues Thr14, Phe15 and Hie22 and NAD^+ with residues Thr14, and Phe15, made the binding of anionic molecules such as ANS and mant-ATP less favourable. Thus, resulting in the displacement of the fluorescent dyes and the concomitant decrease in their fluorescence (Figure 5.5 and 5.7).

The stabilisation of the ligands in the interior of the *Kp*NaMNAT receptor was analysed by utilising a 100 ns simulation time. This showed that all the four simulated complexes were

properly equilibrated, thus suggesting that the extrapolations made from this MD simulation data can be reliable.

Generally, the binding of ligands to proteins induces conformational changes that may consequently affect the functions of the proteins. Evaluation of the impact of ligand binding on the structural dynamics of *Kp*NaMNAT protein was determined by measuring the Cα RMSD, the sidechain RMSF and the Rg of the systems. As derived from the Cα RMSD of the simulated systems, the binding of the ligands decreases the stability of the protein with ATP exhibiting the highest RMSD value in the presence of Mg^{2+}. The deviation in the RMSD value between *Kp*NaMNAT-apo and the *Kp*NaMNAT-ligand complexes both in the absence and presence of Mg^{2+} is between 1-3 Å, thus signifying that the ligand binding does not necessarily induce conformational change on the global structure of *Kp*NaMNAT protein. This further buttresses the no shift observed in the emission wavelength of ANS as well as in the thermal stability assay of the protein upon ligand binding.

Furthermore, since the binding of a ligand to protein may either decrease or increase the movement of the molecular structure, the flexibility of the protein structure was evaluated. Interestingly, the *Kp*NaMNAT-ATP complex in the presence of Mg^{2+} is the only system that demonstrated a major side chain perturbation when compared to the apo form, while the other systems only show a comparable side-chain fluctuation with *Kp*NaMNAT-apo. This side-chain fluctuation is mainly influenced by the presence of Mg^{2+}, suggesting the importance of the metal in ATP catalysis. From the RMSD and RMSF of the ligand with respect to the protein receptor, it is apparent that ATP is the most dynamic of all the three ligands, and its motion increases with the presence of Mg^{2+}. Moreover, considering that there was some form of molecular vibrations in the atoms of ATP (Figure 6.10), it is expected that ATP should show some form of dynamism in other for it to react.

Also, considering the Rg of the four simulated systems, it is evident that the presence of Mg^{2+} impacts the dynamism of ATP within the *Kp*NaMNAT receptor as observed from the massive structural deviation in the compactness of the protein when in complex with ATP and Mg^{2+}. This lends credence to the information given by the RMSF. In the absence of Mg^{2+}, all the ligands behave almost the same way. This shows that ATP responds to Mg^{2+} more than the other ligands and the protein response in the presence of Mg^{2+}, which possibly explains why the protein requires metals for activity. Therefore, we can safely postulate from the RMSD, RMSF, and Rg indices that Mg^{2+} has a major effect on ATP, and its presence is required by ATP for both binding and catalytic functioning.

Based on the 2D interaction plots obtained from the clusters of Trajectory frame, all the three ligands maintained hydrogen bonds and formed water bridges with the side chains. The binding of ATP, NMN, and NAD^+ to *Kp*NaMNAT modifies the dynamics of water molecules within the protein receptor. This is evident from the variation of water molecules in the absence and presence of Mg^{2+}. More water molecules were attracted by NAD^+ in the presence of Mg^{2+}; however, ATP and NMN showed a reduction in water molecules; thus, affirming alteration in the polarity of the micro-environment of the protein receptor relative to the apo-structure. This correlates well with the redshift in the maximum emission wavelength of mant-ATP obtained upon the ligand binding.

Water molecules play a significant role in ligand recognition, stabilisation of a protein-ligand complex as well as conformational dynamics (Ladbury, 1996; Maurer and Oostenbrink, 2019). The occupancy of water molecules in protein ligand interface can facilitate the binding of ligand by contributing favourably to free energy (Connelly *et al.*, 1994; Ladbury, 1996). Nevertheless, because of the extreme entropic cost involved in locking highly dynamic water molecules, an interface with lesser or no water molecules between the ligand and the protein may yield a higher binding affinity than a ligand-binding interface occupied by water molecules (Ringe, 1995). This explains the kind of binding that possibly exists for *Kp*NaMNAT-NAD^+ complex, in readiness for the release of NAD^+ from the binding site. This also correlates with the increase in the SASA observed for NAD^+ protein complex in the presence of Mg^{2+} as against the other two ligand complexes, as well as previous studies reporting the binding of NAD^+ in *sa*NaMNAT, *bs*NaMNAT, and *mt*NaMNAT (Saridakis *et al.*, 2001; Olland *et al.*, 2002; Han *et al.*, 2006) to be buried in a solvent accessible cleft in readiness for its release. Consequently, confirming the role of Mg^{2+} as an effective cofactor in catalytic turnover and its efficiency in product release (Knape *et al.*, 2015).

Chapter 7

CONCLUSION

Given the vital role of NAD^+ in bacterial survival and the indispensability of NaMNAT enzyme in the biosynthesis of NAD^+, NaMNAT comes as an attractive target to explore for the development of antibacterial agents. Though NaMNAT activity is widely conserved, the enzymes exhibit different structural and catalytic properties that reflect their species and specificity. In this study, we successfully overexpressed and purified recombinant NaMNAT from *K. pneumoniae* and *E. faecium* for the first time and showed that though both enzymes are from bacteria, they exhibit different structures and catalytic properties. From the functional study conducted, we were able to establish that NaMNAT from gram-negative *K. pneumoniae* and NaMNAT from gram-positive *E. faecium* utilise NMN at different rate, they have preferences for various divalent metal ions and exhibit a differential requirement for Mg^{2+}. *Kp*NaMNAT exhibits a higher catalytic rate at utilising NMN as a substrate to form NAD^+ with broad pH optima between 6.5 and 9.0 and a preference for Mg^{2+}. *Ef*NaMNAT, on the other hand, demonstrated a significantly reduced activity using NMN substrate with a narrow pH optimum at 8.0 that was not easily reproducible. Its preferred divalent metal ion was Zn^{2+}, which showed a reaction rate 13 times higher than Mg^{2+} of the same concentration.

Furthermore, we deduced from the structural analysis that both proteins are predominately α-helical though, *Ef*NaMNAT contains more proportions of α-helices and β-strands than *Kp*NaMNAT. At the same time, *Kp*NaMNAT possesses loops that are absent in *Ef*NaMNAT. Overall, *Kp*NaMNAT exists in solution mainly as a monomer and *Ef*NaMNAT as a homodimer. Analysis of the protein's conformation, stability, and interaction with ligands revealed that *Kp*NaMNAT and *Ef*NaMNAT do not bind their substrates with the same hydrophobicity. *Kp*NaMNAT exhibits a more hydrophobic binding than *Ef*NaMNAT; however, the binding of ligands to this pocket did not induce a conformational change in *Kp*NaMNAT compared to *Ef*NaMNAT. Also, we found *Ef*NaMNAT to be more stable than *Kp*NaMNAT, and this stability is enhanced upon ligand binding. However, ligand binding did not impact the stability of *Kp*NaMNAT; nonetheless, Zn^{2+} and Cu^{2+} alter the conformation of *Kp*NaMNAT. Thus, confirming that not all metals that substitute Mg^{2+} in substrate binding and phosphoryl transfer are efficient at substrate turnover.

The integration of computational study into this research further provides an understanding of the overall behaviour and dynamics of the proteins at the atomic level. From

the induced-fit ligand docking, we could infer that all three ligands, ATP, NMN, and NAD^+, bind at the same site on *Kp*NaMNAT, and are stabilised by H-bonds, water-bridges, electrostatic, and van der Waals interactions. We hypothesise that if the protein dynamics is not affected by the presence of Mg^{2+}, then the protein will evolve in a similar pattern with or without Mg^{2+}; also, the bound ligands will have a similar evolution in the absence or presence of Mg^{2+}. From the 100 ns simulation performed, we could conclude that the binding of the ligands does not severely perturb the global structure of *Kp*NaMNAT. Also, Mg^{2+} affects the dynamics of ATP compared to NMN and NAD^+, and the presence of ATP and Mg^{2+} alters the overall gyration of the protein, making it more dynamic and less compact. It is expected that NAD^+ may not alter the dynamics of the protein much, given that it is a product, but for an effective collision that will result in the transfer of adenyl group to NMN, the protein must be dynamic enough to allow the reaction to occur.

The successful overexpression and the availability of highly purified recombinant *Kp*NaMNAT and *Ef*NaMNAT provide a good starting point for accessing excellent knowledge of the enzymes and developing novel applications of the enzymes. Moreover, the differences observed in the biophysical structures of *Kp*NaMNAT and *Ef*NaMNAT all provide insight into the distinctive features and possibly the evolutionary answer of the different roles of NaMNAT from Gram-negative *K. pneumoniae* and Gram-positive *E. faecium,* as well as a basis for structure-function comparison between the two classes of bacteria. Also, this presents the possibility of designing inhibitors that are highly specific to a selected NaMNAT target, thus preventing the displacement of the microflora of the host while treating nosocomial infection. Furthermore, the understanding provided by the computational studies of *Kp*NaMNAT-substrate binding site, its stabilisation, the dynamics of the protein when bound and unbound to ligands, the dynamics of the ligands with respect to the receptor site, and the impact of Mg^{2+} on the dynamics of the substrates as well as on the dynamics of the protein, are essential information required to successfully design molecular compounds that can selectively inhibit the activity of NaMNAT enzyme in *K. pneumoniae.*

Overall, the data and insight provided by this research form the structural foundation of understanding the biological role of *Kp*NaMNAT and *Ef*NaMNAT. This information would be useful in the novel application of these enzymes in molecular biology and biophysics, bioinformatics and biochemistry. It would serve as a molecular basis for further evaluation in the design of structure-based inhibitors with therapeutic potential. Besides, this is just a starting point to unravelling these novel proteins. Further investigations encompassing the crystallisation of the proteins and the subsequent structure determination is required, especially

for *Ef*NaMNAT, given that a 3D model structure of the protein could not be acquired. In a situation where obtaining perfect crystals become difficult, isotopic labelling of the protein as a prelude to solving the 3D structure using NMR spectroscopy can be conducted and used to provide information on residues involved in the interaction of various ligands as revealed by *in silico* studies. Also, considering that NaMNAT is a dual substrate enzyme utilising both NMN and NaMN, and this study was centred using the NMN substrate, further investigation using the NaMN substrate is proposed, which can be compared with the results obtained with NMN substrate. Investigations involving the kinetics and direct binding studies of the enzyme and substrates would also be required in order to provide better insight into the kind of binding mechanism demonstrated by the two proteins. Other computational approaches such as drug binding studies, MM/GBSA free binding energy calculations, principal component analysis (PCA), and per-residue energy decomposition calculations can be explored in future studies, as this information would be beneficial in rational drug discovery, design, and development.

References

Enzymology of Nad+ Synthesis. Advances in Enzymology and Related Areas of Molecular Biology**:** 135-182.

Achilonu, I., et al. (2020). "Targeting the SARS-CoV-2 main protease using FDA-approved Isavuconazonium, a P2-P3 α-ketoamide derivative and Pentagastrin: An in-silico drug discovery approach." Journal of molecular graphics & modelling **101**: 107730-107730.

Allegranzi, B., et al. (2011). "Burden of endemic health-care-associated infection in developing countries: systematic review and meta-analysis." The Lancet **377**(9761): 228-241.

Balducci, E., et al. (1995). "Assay Methods for Nicotinamide Mononucleotide Adenylyltransferase of Wide Applicability." Analytical Biochemistry **228**(1): 64-68.

Bathke, J., et al. (2016). "Structural and Functional Characterization of Plasmodium falciparum Nicotinic Acid Mononucleotide Adenylyltransferase." Journal of Molecular Biology **428**(24, Part B): 4946-4961.

Begley, T. P., et al. (2001). The biosynthesis of nicotinamide adenine dinucleotides in bacteria. Vitamins & Hormones, Academic Press. **61:** 103-119.

Bennett, C. J., et al. (1995). "Differences in urinary tract infections in male and female spinal cord injury patients on intermittent catheterization." Spinal Cord **33**(2): 69-72.

Berendsen, H. J. C., et al. (1987). "The missing term in effective pair potentials." The Journal of Physical Chemistry **91**(24): 6269-6271.

Berger, F., et al. (2004). "The new life of a centenarian: signalling functions of NAD(P)." Trends in Biochemical Sciences **29**(3): 111-118.

Bieganowski, P. and C. Brenner (2004). "Discoveries of Nicotinamide Riboside as a Nutrient and Conserved NRK Genes Establish a Preiss-Handler Independent Route to NAD⁺ in Fungi and Humans." Cell **117**(4): 495-502.

Boucher, H. W., et al. (2009). "Bad Bugs, No Drugs: No ESKAPE! An Update from the Infectious Diseases Society of America." Clinical Infectious Diseases **48**(1): 1-12.

Bras, N., et al. (2015). Computational Biochemistry.

Brekasis, D. and M. S. B. Paget (2003). "A novel sensor of NADH/NAD⁺ redox poise in Streptomyces coelicolor A3(2)." The EMBO Journal **22**(18): 4856.

Chambers, H. F. (2005). "Community-Associated MRSA — Resistance and Virulence Converge." New England Journal of Medicine **352**(14): 1485-1487.

Chauhan, J. S., et al. (2009). "Identification of ATP binding residues of a protein from its primary sequence." BMC Bioinformatics **10**(1): 434.

Chung, S. Y. and S. Subbiah (1996). "A structural explanation for the twilight zone of protein sequence homology." Structure **4**(10): 1123-1127.

Coffin, S. E. and T. E. Zaoutis (2011). CHAPTER 35 - HealthCare–Associated Infections in the Nursery. Infectious Diseases of the Fetus and Newborn (Seventh Edition). J. S. Remington, J. O. Klein, C. B. Wilson, V. Nizet and Y. A. Maldonado. Philadelphia, W.B. Saunders**:** 1126-1143.

Cohen, S. N., et al. (1972). "Nonchromosomal antibiotic resistance in bacteria: genetic transformation of Escherichia coli by R-factor DNA." Proceedings of the National Academy of Sciences of the United States of America **69**(8): 2110-2114.

Connelly, P. R., et al. (1994). "Enthalpy of hydrogen bond formation in a protein-ligand binding reaction." Proceedings of the National Academy of Sciences of the United States of America **91**(5): 1964-1968.

Contreras-Rodríguez, L. E., et al. (2018). "Structural insights into Plasmodium falciparum nicotinamide mononucleotide adenylyltransferase: oligomeric assembly." Memórias do Instituto Oswaldo Cruz **113**.

Contreras, L. E., et al. (2015). "Identification and functional evaluation of Leishmania braziliensis Nicotinamide Mononucleotide Adenylyltransferase." Protein Expression and Purification **115**: 26-33.

Cornell, W. D., et al. (1995). "A Second Generation Force Field for the Simulation of Proteins, Nucleic Acids, and Organic Molecules." Journal of the American Chemical Society **117**(19): 5179-5197.

D'Angelo, I., et al. (2000). "Structure of nicotinamide mononucleotide adenylyltransferase: a key enzyme in NAD+ biosynthesis." Structure **8**(9): 993-1004.

Daniel, D. S., et al. (2015). "Public Health Risks of Multiple-Drug-Resistant Enterococcus spp. in Southeast Asia." Applied and environmental microbiology **81**(18): 6090-6097.

Dave, J., et al. (2005). "Nosocomial infections." Continuing Education in Anaesthesia Critical Care & Pain **5**(1): 14-17.

De Angelis, G., et al. (2018). "Incidence and antimicrobial resistance trends in bloodstream infections caused by ESKAPE and Escherichia coli at a large teaching hospital in Rome, a 9-year analysis (2007–2015)." European Journal of Clinical Microbiology & Infectious Diseases **37**(9): 1627-1636.

Deshpande, L. M., et al. (2007). "Antimicrobial resistance and molecular epidemiology of vancomycin-resistant enterococci from North America and Europe: a report from the SENTRY antimicrobial surveillance program." Diagnostic Microbiology and Infectious Disease **58**(2): 163-170.

Di Stefano, M., et al. (2010). "Unique expression pattern of human nicotinamide mononucleotide adenylyltransferase isozymes in red blood cells." Blood Cells, Molecules, and Diseases **45**(1): 33-39.

Dolan, K. M., et al. (2000). "Functional Comparison of the NAD Binding Cleft of ADP-Ribosylating Toxins." Biochemistry **39**(28): 8266-8275.

Duan, Y., et al. (2003). "A point-charge force field for molecular mechanics simulations of proteins based on condensed-phase quantum mechanical calculations." Journal of Computational Chemistry **24**(16): 1999-2012.

Edwardson, S. and C. Cairns (2019). "Nosocomial infections in the ICU." Anaesthesia & Intensive Care Medicine **20**(1): 14-18.

Elizabeth, M., et al. (2019). Nosocomial Infections in Sub-Saharan Africa**:** 90-102.

Elward, A. M., et al. (2001). "Nosocomial Primary Bloodstream Infections in Intensive Care Unit Patients in a Nonteaching Community Medical Center: A 21-Month Prospective Study." Clinical Infectious Diseases **33**(8): 1329-1335.

Emanuelli, M., et al. (2003). "Identification and characterization of a second NMN adenylyltransferase gene in Saccharomyces cerevisiae." Protein Expression and Purification **27**(2): 357-364.

Emanuelli, M., et al. (1999). "Identification and characterization of YLR328W, the Saccharomyces cerevisiae structural gene encoding NMN adenylyltransferase. Expression and characterization of the recombinant enzyme." FEBS Letters **455**(1-2): 13-17.

Emanuelli, M., et al. (2001). "Molecular cloning, chromosomal localization, tissue mRNA levels, bacterial expression, and enzymatic properties of human NMN adenylyltransferase." J Biol Chem **276**(1): 406-412.

Emanuelli, M., et al. (1992). "NAD biosynthesis in human placenta: Purification and characterization of homogeneous NMN adenylyltransferase." Archives of Biochemistry and Biophysics **298**(1): 29-34.

Gao, W., et al. (2018). "Evolution of virulence in Enterococcus faecium, a hospital-adapted opportunistic pathogen." Current Opinion in Microbiology **41**: 76-82.

Gasymov, O. K. and B. J. Glasgow (2007). "ANS fluorescence: potential to augment the identification of the external binding sites of proteins." Biochimica et biophysica acta **1774**(3): 403-411.

Gazzaniga, F., et al. (2009). "Microbial NAD metabolism: lessons from comparative genomics." Microbiology and molecular biology reviews : MMBR **73**(3): 529-541.

Gerdes, S. Y., et al. (2002). "From Genetic Footprinting to Antimicrobial Drug Targets: Examples in Cofactor Biosynthetic Pathways." Journal of bacteriology **184**(16): 4555.

Greenfield, N. J. (2006). "Using circular dichroism spectra to estimate protein secondary structure." Nature protocols **1**(6): 2876-2890.

Gromiha, M. M. (2010). Chapter 6 - Protein Stability. Protein Bioinformatics. M. M. Gromiha. Singapore, Academic Press**:** 209-245.

Guvench, O. and A. D. MacKerell (2008). Comparison of Protein Force Fields for Molecular Dynamics Simulations. Molecular Modeling of Proteins. A. Kukol. Totowa, NJ, Humana Press**:** 63-88.

Han, S., et al. (2006). "Crystal Structure of Nicotinic Acid Mononucleotide Adenylyltransferase from Staphyloccocus aureus: Structural Basis for NaAD Interaction in Functional Dimer." Journal of Molecular Biology **360**(4): 814-825.

Hidron, A. I., et al. (2008). "Antimicrobial-Resistant Pathogens Associated With Healthcare-Associated Infections: Annual Summary of Data Reported to the National Healthcare Safety Network at the Centers for Disease Control and Prevention, 2006–2007." Infection Control & Hospital Epidemiology **29**(11): 996-1011.

Hughes, K. T., et al. (1983). "An indispensable gene for NAD biosynthesis in Salmonella typhimurium." Journal of bacteriology **155**(1): 213-221.

Hung, C.-L. and C.-C. Chen (2014). "Computational Approaches for Drug Discovery." Drug Development Research **75**(6): 412-418.

Idiong, G., et al. (2011). "Investigating the effect of a single glycine to alanine substitution on interactions of antimicrobial peptide latarcin 2a with a lipid membrane." European Biophysics Journal **40**(9): 1087.

Imai, S.-i., et al. (2000). "Transcriptional silencing and longevity protein Sir2 is an NAD-dependent histone deacetylase." Nature **403**(6771): 795-800.

Izard, T. and A. Geerlof (1999). "The crystal structure of a novel bacterial adenylyltransferase reveals half of sites reactivity." The EMBO Journal **18**(8): 2021-2030.

Jabbari Shiadeh, S. M., et al. (2019). "Global prevalence of antibiotic resistance in blood-isolated Enterococcus faecalis and Enterococcus faecium: a systematic review and meta-analysis." Infection and drug resistance **12**: 2713-2725.

Jayaram, H., et al. (2011). "NMNAT expression and its relation to NAD metabolism." Current Medicinal Chemistry **18**: 1962-1972.

Jeremy M Berg, J. L. T., and Lubert Stryer (2002). DNA Polymerases Require a Template and a Primer. Biochemistry. New York, W H Freeman.

Jorgensen, W. L., et al. (1983). "Comparison of simple potential functions for simulating liquid water." The Journal of Chemical Physics **79**(2): 926-935.

Jorgensen, W. L., et al. (1996). "Development and Testing of the OPLS All-Atom Force Field on Conformational Energetics and Properties of Organic Liquids." Journal of the American Chemical Society **118**(45): 11225-11236.

Karplus, M. and J. A. McCammon (2002). "Molecular dynamics simulations of biomolecules." Nat Struct Biol **9**(9): 646-652.

Katoh, A. and T. Hashimoto (2004). Molecular biology of pyridine nucleotide and nicotine biosynthesis.

Knape, M. J., et al. (2015). "Divalent Metal Ions Mg2+ and Ca2+ Have Distinct Effects on Protein Kinase A Activity and Regulation." ACS Chemical Biology **10**(10): 2303-2315.

Knape, M. J., et al. (2017). "Divalent metal ions control activity and inhibition of protein kinases." Metallomics **9**(11): 1576-1584.

Kollman, P. A. (1996). "Advances and Continuing Challenges in Achieving Realistic and Predictive Simulations of the Properties of Organic and Biological Molecules." Accounts of Chemical Research **29**(10): 461-469.

Kopp, J. and T. Schwede (2004). "Automated protein structure homology modeling: a progress report." Pharmacogenomics **5**(4): 405-416.

Kumarasamy, K. K., et al. (2010). "Emergence of a new antibiotic resistance mechanism in India, Pakistan, and the UK: a molecular, biological, and epidemiological study." The Lancet Infectious Diseases **10**(9): 597-602.

Kurnasov, O., et al. (2003). "NAD Biosynthesis: Identification of the Tryptophan to Quinolinate Pathway in Bacteria." Chemistry & biology **10**(12): 1195-1204.

Kurnasov, O. V., et al. (2002). "Ribosylnicotinamide Kinase Domain of NadR Protein: Identification and Implications in NAD Biosynthesis." Journal of bacteriology **184**(24): 6906.

Ladbury, J. E. (1996). "Just add water! The effect of water on the specificity of protein-ligand binding sites and its potential application to drug design." Chemistry & biology **3**(12): 973-980.

Laemmli, U. K. (1970). "Cleavage of Structural Proteins during the Assembly of the Head of Bacteriophage T4." Nature **227**(5259): 680-685.

Lau, C., et al. (2009). "The NMN/NaMN adenylyltransferase (NMNAT) protein family." Frontiers in bioscience : a journal and virtual library **14**: 410-431.

Lau, C., et al. (2009). "The NMN/NaMN adenylyltransferase (NMNAT) protein family." Front Biosci **14**: 410-431.

Leavis, H. L., et al. (2006). "High-Level Ciprofloxacin Resistance from Point Mutations in gyrA and parC Confined to Global Hospital-Adapted Clonal Lineage CC17 of <em>Enterococcus faecium</em&gt." Journal of Clinical Microbiology **44**(3): 1059.

Leavis, H. L., et al. (2003). "Epidemic and nonepidemic multidrug-resistant Enterococcus faecium." Emerging infectious diseases **9**(9): 1108-1115.

Lee, H. C. (1997). "Mechanisms of calcium signaling by cyclic ADP-ribose and NAADP." Physiological Reviews **77**(4): 1133-1164.

Lewis, J. S., et al. (2007). "First Report of the Emergence of CTX-M-Type Extended-Spectrum β-Lactamases (ESBLs) as the Predominant ESBL Isolated in a U.S. Health Care System." Antimicrobial Agents and Chemotherapy **51**(11): 4015.

Liu, G., et al. (1982). "Nucleoside salvage pathway for NAD biosynthesis in Salmonella typhimurium." Journal of bacteriology **152**(3): 1111.

Lobanov, M. Y., et al. (2008). "Radius of gyration as an indicator of protein structure compactness." Molecular Biology **42**(4): 623-628.

Lockhart, S. R., et al. (2007). "Antimicrobial Resistance among Gram-Negative Bacilli Causing Infections in Intensive Care Unit Patients in the United States between 1993 and 2004." Journal of Clinical Microbiology **45**(10): 3352.

Lowe, G. and G. Tansley (1983). "The Stereochemical Course of Nucleotidyl Transfer Catalysed by NAD Pyrophosphorylase." European Journal of Biochemistry **132**(1): 117-120.

Lowman, W. (2016). "Active surveillance of hospital-acquired infections in South Africa: Implementation, impact and challenges." South African Medical Journal; Vol 106, No 5 (2016).

Lu, S., et al. (2008). "Structure of nicotinic acid mononucleotide adenylyltransferase from Bacillus anthracis." Acta crystallographica. Section F, Structural biology and crystallization communications **64**(Pt 10): 893-898.

Lye, W. C., et al. (1992). "Urinary tract infections in patients with diabetes mellitus." Journal of Infection **24**(2): 169-174.

MacKerell, A. D., et al. (1998). "All-Atom Empirical Potential for Molecular Modeling and Dynamics Studies of Proteins." The Journal of Physical Chemistry B **102**(18): 3586-3616.

Magni, G., et al. (1999). "Enzymology of NAD+ synthesis." Adv Enzymol Relat Areas Mol Biol **73**: 135-182.

Mahoney, M. W. and W. L. Jorgensen (2000). "A five-site model for liquid water and the reproduction of the density anomaly by rigid, nonpolarizable potential functions." The Journal of Chemical Physics **112**(20): 8910-8922.

Mandal, S. M., et al. (2014). "Challenges and future prospects of antibiotic therapy: from peptides to phages utilization." Frontiers in pharmacology **5**: 105-105.

Maurer, M. and C. Oostenbrink (2019). "Water in protein hydration and ligand recognition." Journal of Molecular Recognition **32**(12): e2810.

McConkey, B., et al. (2002). "The performance of current methods in ligand-protein docking." Current Science **83**.

Mehl, R. A., et al. (2000). "Identification of the Escherichia coliNicotinic Acid Mononucleotide Adenylyltransferase Gene." Journal of bacteriology **182**(15): 4372.

Mei, G., et al. (2005). "The importance of being dimeric." The FEBS Journal **272**(1): 16-27.

Moland, E. S., et al. (2006). "Prevalence of Newer β-Lactamases in Gram-Negative Clinical Isolates Collected in the United States from 2001 to 2002." Journal of Clinical Microbiology **44**(9): 3318.

Morris, G. M. and M. Lim-Wilby (2008). Molecular Docking. Molecular Modeling of Proteins. A. Kukol. Totowa, NJ, Humana Press**:** 365-382.

Murphy, J. R. (2011). "Mechanism of diphtheria toxin catalytic domain delivery to the eukaryotic cell cytosol and the cellular factors that directly participate in the process." Toxins **3**(3): 294-308.

Nair, A., et al. (2018). "Prevalence of healthcare-associated infection at a tertiary hospital in the Northern Cape Province, South Africa." South African Family Practice **60**(5): 162-167.

Neet, K. E. and D. E. Timm (1994). "Conformational stability of dimeric proteins: quantitative studies by equilibrium denaturation." Protein science : a publication of the Protein Society **3**(12): 2167-2174.

Niesen, F. H., et al. (2007). "The use of differential scanning fluorimetry to detect ligand interactions that promote protein stability." Nature protocols **2**(9): 2212-2221.

Olland, A. M., et al. (2002). "Identification, characterization, and crystal structure of Bacillus subtilis nicotinic acid mononucleotide adenylyltransferase." The Journal of biological chemistry **277**(5): 3698-3707.

Oostenbrink, C., et al. (2004). "A biomolecular force field based on the free enthalpy of hydration and solvation: The GROMOS force-field parameter sets 53A5 and 53A6." Journal of Computational Chemistry **25**(13): 1656-1676.

Oprea, S. F., et al. (2004). "Molecular and clinical epidemiology of vancomycin-resistant Enterococcus faecalis." Journal of Antimicrobial Chemotherapy **53**(4): 626-630.

Osterman, A. L. and T. P. Begley (2007). A subsystems-based approach to the identification of drug targets in bacterial pathogens. Systems Biological Approaches in Infectious Diseases. H. I. Boshoff and C. E. Barry. Basel, Birkhäuser Basel**:** 131-170.

Pendleton, J. N., et al. (2013). "Clinical relevance of the ESKAPE pathogens." Expert review of anti-infective therapy **11**(3): 297-308.

Penzkofer, A., et al. (2007). "Protein aggregation studied by forward light scattering and light transmission analysis." Chemical Physics **342**(1): 55-63.

Phillips, J. C., et al. (2005). "Scalable molecular dynamics with NAMD." Journal of Computational Chemistry **26**(16): 1781-1802.

Phillips, M. A., et al. (2018). Has Molecular Docking Ever Brought us a Medicine.

Podschun, R. and U. Ullmann (1998). "Klebsiella spp. as Nosocomial Pathogens: Epidemiology, Taxonomy, Typing Methods, and Pathogenicity Factors." Clinical Microbiology Reviews **11**(4): 589.

Pollegioni, L., et al. (2003). "Contribution of the dimeric state to the thermal stability of the flavoprotein D-amino acid oxidase." Protein science : a publication of the Protein Society **12**(5): 1018-1029.

Pooe, K., et al. (2021). "An empirical and theoretical description of Schistosoma japonicum glutathione transferase inhibition by bromosulfophthalein and indanyloxyacetic acid 94." Journal of Molecular Structure **1223**: 128892.

Porath, J. (1992). "Immobilized metal ion affinity chromatography." Protein Expression and Purification **3**(4): 263-281.

Pounds, A. J. (2004). "Computational Chemistry Using the PC, 3rd Edition (Donald W. Rogers)." Journal of Chemical Education **81**(10): 1423.

Provencher, S. W. and J. Gloeckner (1981). "Estimation of globular protein secondary structure from circular dichroism." Biochemistry **20**(1): 33-37.

Raffaelli, N., et al. (1999). "Synechocystis sp. slr0787 protein is a novel bifunctional enzyme endowed with both nicotinamide mononucleotide adenylyltransferase and 'Nudix' hydrolase activities." FEBS Letters **444**(2-3): 222-226.

Raffaelli, N., et al. (1999). "The Escherichia coli NadR Regulator Is Endowed with Nicotinamide Mononucleotide Adenylyltransferase Activity." Journal of bacteriology **181**(17): 5509.

Raffaelli, N., et al. (1997). "Characterization of nicotinamide mononucleotide adenylyltransferase from thermophilic archaea." Journal of bacteriology **179**(24): 7718.

Raffaelli, N., et al. (2002). "Identification of a novel human nicotinamide mononucleotide adenylyltransferase." Biochemical and Biophysical Research Communications **297**(4): 835-840.

Ramachandran, G. N., et al. (1963). "Stereochemistry of polypeptide chain configurations." Journal of Molecular Biology **7**(1): 95-99.

Rice, L. B. (2008). "Federal Funding for the Study of Antimicrobial Resistance in Nosocomial Pathogens: No ESKAPE." The Journal of Infectious Diseases **197**(8): 1079-1081.

Rice, L. B. (2010). "Progress and Challenges in Implementing the Research on ESKAPE Pathogens." Infection Control & Hospital Epidemiology **31**(S1): S7-S10.

Ringe, D. (1995). "What makes a binding site a binding site?" Current Opinion in Structural Biology **5**(6): 825-829.

Riordan, J. F. (1977). "The role of metals in enzyme activity." Ann Clin Lab Sci **7**(2): 119-129.

Robert C. Moellering, Jr. (1992). "Emergence of Enterococcus as a Significant Pathogen." Clinical Infectious Diseases **14**(6): 1173-1176.

Rodionova, I. A., et al. (2014). "Metabolic and Bactericidal Effects of Targeted Suppression of NadD and NadE Enzymes in Mycobacteria." mBio **5**(1): e00747-00713.

Rothe, C., et al. (2013). "Healthcare-associated infections in sub-Saharan Africa." Journal of Hospital Infection **85**(4): 257-267.

Sachin Patodia, A. B. a. D. C. (2014). "Molecular Dynamics Simulation of Proteins: A Brief Overview." Journal of Physical Chemistry & Biophysics **Volume 4**(Issue 6): 4.

Santajit, S. and N. Indrawattana (2016). "Mechanisms of Antimicrobial Resistance in ESKAPE Pathogens." BioMed research international **2016**: 2475067-2475067.

Saridakis, V., et al. (2001). "Insights into ligand binding and catalysis of a central step in NAD+ synthesis: structures of Methanobacterium thermoautotrophicum NMN adenylyltransferase complexes." J Biol Chem **276**(10): 7225-7232.

Sauve, A. A. (2008). "NAD⁺ and Vitamin B₃: From Metabolism to Therapies." Journal of Pharmacology and Experimental Therapeutics **324**(3): 883.

Schweiger, M., et al. (2001). "Characterization of recombinant human nicotinamide mononucleotide adenylyl transferase (NMNAT), a nuclear enzyme essential for NAD synthesis." FEBS Letters **492**(1-2): 95-100.

Silverstein, T. P. (2016). "The Alcohol Dehydrogenase Kinetics Laboratory: Enhanced Data Analysis and Student-Designed Mini-Projects." Journal of Chemical Education **93**(5): 963-970.

Sorci, L., et al. (2010). "Genomics-driven reconstruction of Acinetobacter NAD metabolism: Insights for antibacterial target selection." The Journal of biological chemistry **285**: 39490-39499.

Sorci, L., et al. (2013). "Quinolinate Salvage and Insights for Targeting NAD Biosynthesis in Group A Streptococci." Journal of bacteriology **195**(4): 726.

Sorci, L., et al. (2007). "Initial-Rate Kinetics of Human NMN-Adenylyltransferases: Substrate and Metal Ion Specificity, Inhibition by Products and Multisubstrate Analogues, and Isozyme Contributions to NAD + Biosynthesis †." Biochemistry **46**: 4912-4922.

Sorci, L., et al. (2009). "Targeting NAD biosynthesis in bacterial pathogens: Structure-based development of inhibitors of nicotinate mononucleotide adenylyltransferase NadD." Chemistry & biology **16**(8): 849-861.

Sreerama, N. and R. W. Woody (2000). "Estimation of Protein Secondary Structure from Circular Dichroism Spectra: Comparison of CONTIN, SELCON, and CDSSTR Methods with an Expanded Reference Set." Analytical Biochemistry **287**(2): 252-260.

Stank, A., et al. (2016). "Protein Binding Pocket Dynamics." Accounts of Chemical Research **49**(5): 809-815.

System, A. r. f. t. N. (2004). "National Nosocomial Infections Surveillance (NNIS) System Report, data summary from January 1992 through June 2004, issued October 2004." American Journal of Infection Control **32**(8): 470-485.

Treitman, A. N., et al. (2005). "Emerging Incidence of Enterococcus faecium among Hospital Isolates (1993 to 2002)." Journal of Clinical Microbiology **43**(1): 462.

Tzouvelekis, L. S., et al. (2012). "Carbapenemases in Klebsiella pneumoniae and Other Enterobacteriaceae: an Evolving Crisis of Global Dimensions." Clinical Microbiology Reviews **25**(4): 682.

Vallee, B. L. (1955). Zinc and Metalloenzymes. Advances in Protein Chemistry. M. L. Anson, K. Bailey and J. T. Edsall, Academic Press. **10:** 317-384.

Vasoo, S., et al. (2015). "Emerging issues in gram-negative bacterial resistance: an update for the practicing clinician." Mayo Clin Proc **90**(3): 395-403.

Veitch, D. P., et al. (1998). "The role of histidine residues in the HXGH site of CTP:phosphocholine cytidylyltransferase in CTP binding and catalysis." Eur J Biochem **255**(1): 227-234.

Werner, E., et al. (2002). "Crystal structure of human nicotinamide mononucleotide adenylyltransferase in complex with NMN." FEBS Letters **516**(1): 239-244.

Wilkinson, A., et al. (2001). "Bacterial DNA ligases." Molecular microbiology **40**(6): 1241-1248.

Yoon, H.-J., et al. (2005). "Crystal Structure of Nicotinic Acid Mononucleotide Adenylyltransferase from Pseudomonas aeruginosa in its Apo and Substrate-complexed Forms Reveals a Fully Open Conformation." Journal of Molecular Biology **351**(2): 258-265.

Zhang, H., et al. (2002). "Crystal Structures of E. coli Nicotinate Mononucleotide Adenylyltransferase and Its Complex with Deamido-NAD." Structure **10**(1): 69-79.

Zhang, X., et al. (2003). "Structural characterization of a human cytosolic NMN/NaMN adenylyltransferase and implication in human NAD biosynthesis." J Biol Chem **278**(15): 13503-13511.

Zhou, T., et al. (2002). "Structure of Human Nicotinamide/Nicotinic Acid Mononucleotide Adenylyltransferase: BASIS FOR THE DUAL SUBSTRATE SPECIFICITY AND

ACTIVATION OF THE ONCOLYTIC AGENT TIAZOFURIN." Journal of Biological Chemistry **277**(15): 13148-13154.

Ziegler, M. (2000). "New functions of a long-known molecule." European Journal of Biochemistry **267**(6): 1550-1564.

Appendices

APPENDIX A

Reagent and Buffer Preparation

LB-agar [1.5% (w/v) Agar, 1% (w/v) Tryptone, 0.5% (w/v) NaCl, and 0.5% (w/v) Yeast Extracts].

3.0 g agar, 2.0 g tryptone, 1.0 g NaCl and 1.0 g yeast extract were dissolved in 200 mL of dH_2O with continuous stirring. The media was autoclaved, and appropriate antibiotics were added once the agar started cooling.

2xYeast-Tryptone (2xYT) [1.6% (w/v) Tryptone, 1% (w/v) Yeast Extract and 0.5% (w/v) NaCl].

Per 100 mL preparation, 1.6 g tryptone, 1.0 g yeast extract, and 0.5 g NaCl were completely dissolved in dH_2O with continuous stirring. The media was autoclaved and allowed to cool to room temperature.

SOC Medium [2% (w/v) Tryptone, 0.5% (w/v) Yeast Extract, 10 mM NaCl, 2.5 mM $MgCl_2$, 10 mM $MgSO_4$ and 20 mM Glucose].

0.5 g tryptone, 0.25 g yeast extract, and 0.03 g NaCl were dissolved in 25 mL of dH_2O and autoclaved. The media was cooled to approximately 55 °C, after which 125 µL $MgCl_2.6H_2O$, 500 µL $MgSO_4$, and 1 mL glucose were added. The volume was made up to 50 mL with autoclaved dH_2O, and aliquoted into sterile Eppendorf tubes and stored at −20 °C.

Antibiotics

Stock solutions of kanamycin (30 mg/mL^{-1}) and ampicillin (100 mg/mL^{-1}) were prepared in ddH_2O, while chloramphenicol (35 mg/mL^{-1}) was dissolved in 100% (v/v) methanol. Solutions were filtered using a 0.22 µm syringe filter into sterile Eppendorf tubes and stored at −20 °C.

Phosphate Buffered Saline (PBS) [137 mM NaCl, 2.7 mM KCl, 8 mM Na_2HPO_4, and 2 mM KH_2PO_4, pH 7.2].

8.0 g NaCl, 0.2 g KCl, 1.15 g Na_2HPO_4, and 0.2 g KH_2PO_4 were dissolved in 800 mL of dH_2O. pH was adjusted to 7.2 and volume made up to 1 L with dH_2O. Buffer was stored at room temperature.

Resuspension Buffer [PBS, 25 mM Imidazole, 0.01% (w/v) NaN_3, pH 7.2].

0.85 g imidazole and 0.1 g NaN_3 were dissolved in 450 mL PBS buffer, pH was adjusted to 7.2 while topping up the volume to 500 mL with PBS solution. Buffer was stored at room temperature.

Equilibration Buffer [PBS, 25 mM Imidazole, 0.01% (w/v) NaN_3, pH 7.2].

2.55 g imidazole and 0.15 g NaN_3 were dissolved in 1.4 L PBS buffer, pH was adjusted to 7.2 while topping up the volume to 1.5 L with PBS solution. Buffer was stored at room temperature.

Wash Buffer [0.1% (v/v) Tween-20 and Equilibration Buffer, pH 7.2].

0.5 mL tween-20 was made up to 500 mL with equilibration buffer and stored at room temperature.

Elution Buffer [PBS, 350 mM Imidazole, 0.01% (w/v) NaN_3, pH 7.2].

4.77 g imidazole and 0.02 g NaN_3 were dissolved in 150 mL PBS buffer, pH was adjusted to 7.2 while topping up the volume to 200 mL with PBS solution. Buffer was stored at room temperature.

Bradford Dye Reagent [0.06% (w/v) Coomassie Brilliant Blue G-250 in 2% (v/v) perchloric acid]. 0.3 g Coomassie Brilliant Blue G-250 was dissolved in 500 mL of perchloric acid in dH_2O. The solution was stirred for an hour at room temperature, then filtered with Whatman No.1 filter paper into a brown bottle and stored at room temperature.

Dialysis Buffer 1 [10 mM NaH_2PO_4, 1 mM EDTA, 0.01% NaN_3, pH 7.2].

1.20 g NaH_2PO_4, 0.29 g EDTA, and 0.10 g NaN_3 were dissolved in 900 mL of ddH_2O, pH was adjusted to 7.2, and volume made up to 1 L with ddH_2O. Buffer was stored at room temperature.

Monomer solution [30% (w/v) acrylamide, and 2.7% (w/v) bis-acrylamide].

73.0 g acrylamide and 2.0 g bis-acrylamide were dissolved in dH_2O, and the volume was made up to 250 mL. The solution was filtered using Whatman No. 1 filter paper and stored in an amber bottle at 4 °C.

Reducing Sample Buffer [25.0% (v/v) Tris-HCl, 4% (w/v) SDS, 20% (v/v) glycerol, 10% (v/v) β -mercaptoethanol, pH 6.8].

2.5 mL Tris-HCl (0.5 M), 4 mL 10% SDS, 2 mL glycerol, and 1 mL β-mercaptoethanol were mixed thoroughly, and volume was made up to 10 mL with dH_2O. 35 µg of bromophenol blue was added as a tracking dye and stored at room temperature.

Tank/ Electrophoretic buffer [250 mM Tris-HCl, 1.92 M glycine, 0.1% (w/v) SDS, pH 8.3].

15.0 g Tris-HCl and 72.0 g glycine were resuspended in 5 L of dH_2O and stirred. Before use, 1.0 g SDS was added to 900 mL of the buffer. pH adjusted to 8.3 and volume made up to 1 L.

Coomassie Stain Solution [0.1% (w/v) Coomassie dye in 1:5:4 (v/v/v) acetic acid-methanol-water solution].

0.1 g Coomassie dye was dissolved in 1:5:4 (v/v/v) acetic acid-methanol-water solution and store at room temperature.

Destain Solution [10% (v/v) Glacial Acetic Acid, 40% (v/v) Methanol, 50% (v/v) distilled water].

50 mL of glacial acetic acid, 200 mL methanol, and 250 mL dH_2O were mixed and stored at room temperature.

Preparation of competent *E. coli* T7 cells

To 200 mL of autoclaved LB-agar, 35 µg/mL^{-1} of chloramphenicol was added, agar was poured into plates and allowed to solidify. An *E. coli* T7 glycerol stock solution was then spread across plates and incubated for 16-24 h at 37 °C. A single colony was selected afterward and inoculated into 50 mL of 2xYT media overnight at 37 °C in a rotating incubator at 250 × *g*. The overnight culture was diluted with freshly prepared media in the ratio of 1/20 and grown to an optical density of about 0.6 (OD_{600} nm ≈ 0.6) at 37 °C with shaking at 250 rpm. The culture was centrifuged at 5 000 rpm for 10 min at 4 °C. Pelleted cells were resuspended in 10 mL of $MgCl_2$ (100 mM) and incubated on ice for 30 min, followed by centrifugation at 5 000 rpm for 10 min at 4 °C. Afterward, cells were resuspended in 10 mL of $CaCl_2$ (100 mM), incubate on ice for 4 h, and centrifuged at 3 000 × *g* for 10 min at 4 °C. Cells were finally resuspended in 1 mL $CaCl_2$ and 1 mL glycerol (80% (v/v)). 100 µL of the suspension was aliquoted into cold sterile Eppendorf tubes using cold sterile pipette tips. The cells were quickly frozen in liquid nitrogen and stored at −80 °C.

Gel Preparation and set-up

SDS gel was set up using 12.5% (w/v) separating gel and 4% (w/v) stacking gel prepared according to the protocol in Table 3.1. TEMED and ammonium persulfate were only added just before pouring the solution into the gel casting unit. The gel-casting unit (Bio-Rad mini-PROTEAN® vertical electrophoresis apparatus) and the glass plates (81.5 mm × 101.5 mm and 72.5 mm × 101.5 mm) were assembled, and the gel was set up by pouring separating gel solution first into the glass plate casting unit to a height of about 6cm from the base and covered with a little water, to prevent oxidative inhibition of polymerisation of the acrylamide. Upon polymerisation, the water cover was removed, and the glass plate topped up to the brim with the stacking gel, followed by immediate insertion of a 1.5 mm gel comb into the stacking gel and allowed to polymerise. Afterward, the glass plate was removed from the casting unit and then transferred into the electrophoresis tank. The gel comb was removed, and samples loaded (5 µL of standard Molecular weight marker and 10 µL protein sample) into the gel wells.

Dialysis Buffer-2 [25 mM Tris-HCl, 0.01% NaN_3]

3.03 g Tris-HCl and 0.10 g NaN_3 were dissolved in 900 mL of ddH_2O. pH was adjusted to 7.2 and volume made up to 1 L with ddH_2O.

ANS (8-anilino-1-naphthalenesulfonic acid)

50 mg of ANS was dissolved in 1 mL ddH_2O and vortexed for ~1 h in the dark. This was followed by centrifugation at 13,000 × *g* for 5 min. The supernatant was collected, and the concentration was determined at 350 nm via a UV-Vis *Spectrophotometer (Jasco V-630)* using molar extinction coefficients 5000 M^{-1} cm^{-1}. All ANS preparation procedures were carried out in foil to limit light absorption.

M-ATP (2′/3′-O-(N-Methyl-anthraniloyl)-adenosine-5′-triphosphate)

1 mM stock solution concentration of mant-ATP was prepared by diluting 150 units (150 µL) of 10 mM aqueous mant-ATP solution with 1500 µL ddH_2O. The solution was stored at −20 °C, away from light. Stock preparation was done in the dark.

SYPRO Orange Dye.

50x SYPRO Orange stock concentration was prepared from 5000x concentration by diluting 10 µL of 5000x concentration into 1 mL of ddH_2O.

SE-HPLC Buffer [750 mM NaCl, 10 mM NaH_2PO_4, pH 7.0, 0.01% (w/v) NaN_3].

21.92g NaCl, 0.59 g NaH_2PO_4, and 0.05 g (NaN_3) were dissolved in 450 mL of ddH_2O. pH was adjusted to 7.5 and volume made up to 500 mL with ddH_2O. The prepared buffer was subjected to degassing to prevent introduction of air bubbles and subsequent interference with normal column functioning.

Gel Filtration Standards

The lyophilised mixture containing approximately 18 mg of protein (5.0 mg thyroglobulin, 5.0 mg g-globulin, 5.0 mg ovalbumin, 2.5 mg myoglobin, and 0.5 mg Vitamin B12) per vial of molecular weight markers, was reconstituted with 0.5 mL of deionised water. The vial was swirled gently to mix thoroughly and thereafter it was left on ice for about 2–3 min, followed by another round of mixing. The hydrated mixture was aliquoted and stored at −20°C. Prior to usage, the standards are always centrifuged to remove any larger particles such as aggregated protein.

APPENDIX B

Supplementary Data

```
A_baumannii_SDF.        ----------------------MYTFDYLVFIGRFQPFHLAHMQTIEIALQQSRYVILA 37
A_baumannii_AYE.        ----------------------MYTFDYLVFIGRFQPFHLAHMQTIEIALQQSRYVILA 37
Acinetobacter_Spp.      ----------------------MMNRRIGVLGGSFDPFTLAHERLGEIFLQEIGLDEVR 37
P_putida.               --------MASCAARGPAELSKAQAVRRIGILGGTFDPVHIGHLRSALEVAEFMGLDELR 52
P_aeruginosa.           ----------------------MGKRIGLFGGTFDPVHIGHMRSAVEMAEQFALDELR 36
P_mendocina.            --------------------MNGIGARRIGLLGGTFNPVHNGHLRAALEVAEFMALDELR 40
K_michiganensis.        ----------------------MSDSSLLALYGGTFDPIHYGHLKSVEALARLVKLKSVT 38
K_pneumoniae.           ----------------------MVDMTQLQAIYGGTFDPVHYGHLKPVEILANQIGLSKVI 39
K_oxytoca.              ----------------------MVDMTQLLAMYGGTFDPVHYGHLKPVEILANQIGLNQVT 39
Enterobacter_sp_1.      ----------------------MHSLQALYGGTFDPVHYGHLKPVEILANLIGLQRVT 36
Enterobacter_cloacae.   ----------------------MKTLQALYGGTFDPVHYGHLKPVEVLANLIGLQRVI 36
Enterobacter_sp_2.      ----------------------MVDMNQLQALFGGTFDPVHYGHLKPVEALANQIGLSRVI 39
E_coli.                 ----------------------MKSLQALFGGTFDPVHYGHLKPVETLANLIGLTRVT 36
M_Tuberculosis.         ------------------------------MGGTFDPIHYGHLVAASEVADLFDLDEVV 29
S_condiment.            ----------------------MTQSVVLYGGQFNPVHTAHAVVASEVYHTLKPDRFL 36
S_aureus.               ---------------------MKKIVLYGGQFNPIHTAHMIVASEVFHELQPDEFY 35
S_saprophyticus.        ---------------------MAKSIVLYGGQFNPIHIAHMVVASEVNAFIKPDVFY 36
B_anthracis             ---------------------MRKIGIIGGTFDPPHYGHLLIANEVYHALNLEEVW 35
E_faecalis.             -MGEKRQARQGADVLLQEEPLRFQTRKQVGLLGGNFNPVHLAHLVMADQVQNQLGLDKVY 59
E_faecium.              MMNTQAKTFVRSQLFPEEMPQFLEKKKQVGILGGTFNPVHLAHLVMAEQAGRNLGLDRVF 60
E_saccharolyticus.      ---MQGETFSRVQTFTEMESIRTSPRKQVGILGGTFNPVHIAHLITADQVGKALGLETVA 57
                                                          * *:*   .*          .
```

Figure S1. Multiple sequence alignment of NaMNAT from different bacterial species showing the variation in the conserved "T/HXGH" signature motif sequence. Variation is observed in the glycine residue as it is replaced with alanine. Sequence alignment was generated via Clustal Omega multiple sequence alignment tool.

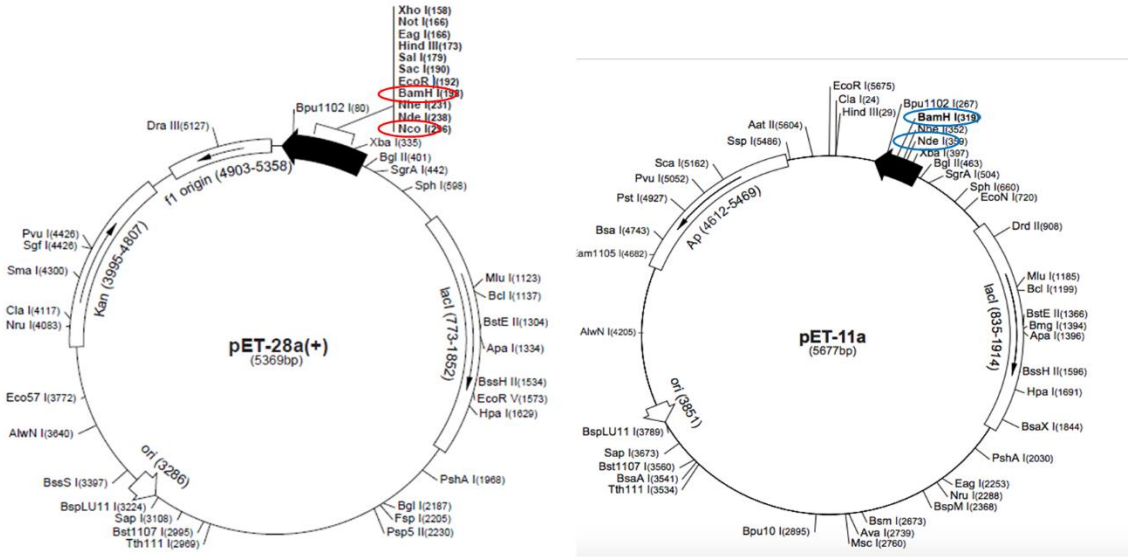

Figure S2. pET-28a and pET-11a vector construct. Sites at which the target gene sequence where inserted into the vector is indicated in circle.

Calculations of *Kp*NaMNAT and *Ef*NaMNAT Concentration determined in conjuncture with Beer Lambert's Law

$A = \varepsilon lc$ …… (Eqn. 1)

$c = A/\varepsilon l$ …… (Eqn. 2)

Where A = absorbance (arbitrary unit)

ε = molar extinction coefficient at 280 nm (*Ef*NaMNAT = 30370 $M^{-1}cm^{-1}$ and *Kp*NaMNAT = 37930 $M^{-1}cm^{-1}$)

c = concentration in Molar

l = path length in cm

$$Conc\ (M) = \frac{Slope}{Molar\ extinction\ coeficient \times 1\ cm\ path\ length}$$ …….. (Eqn. 3)

$$Conc\ (mg/mL) = \frac{Slope \times Molecular\ mass}{Molar\ extinction\ coeficient}$$ …… (Eqn. 4)

$$Conc.of\ EfNaMNAT\ (mg/mL) = \frac{7.612\ \times 25799.45}{30370} = 6.47\ mg/mL$$

$$Conc.of\ KpNaMNAT\ (mg/mL) = \frac{10.46 \times 26831.52}{37930} = 7.40\ mg/mL$$

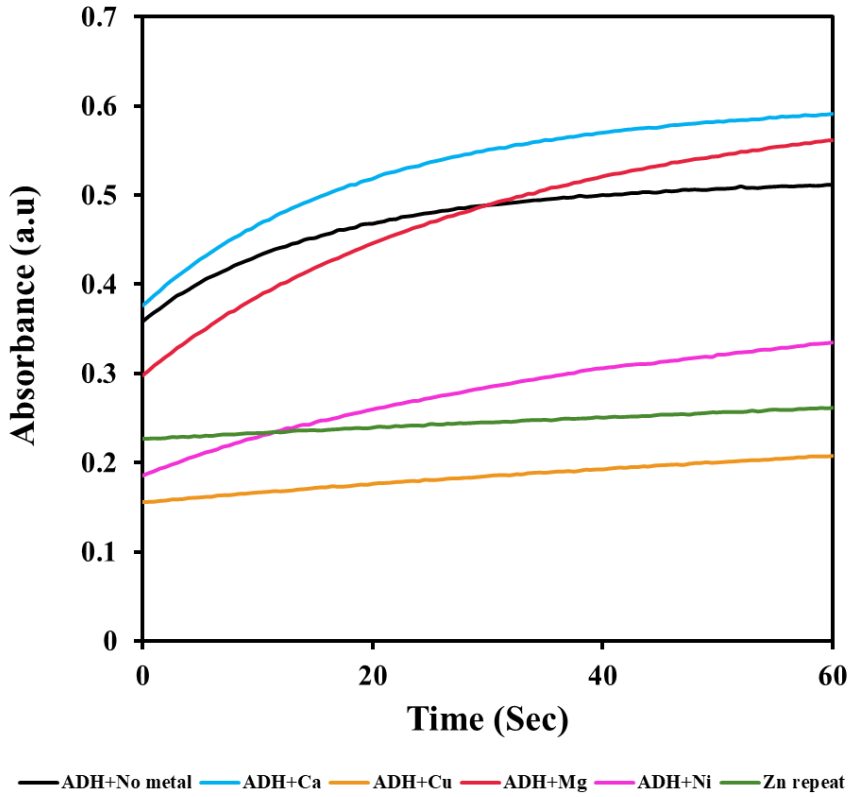

Figure S3. ADH activity in the absence of divalent metal cation and in the presence of Mg^{2+}, Ni^{2+}, Ca^{2+}, Cu^{2+}, and Zn^{2+} at pH 9.0.

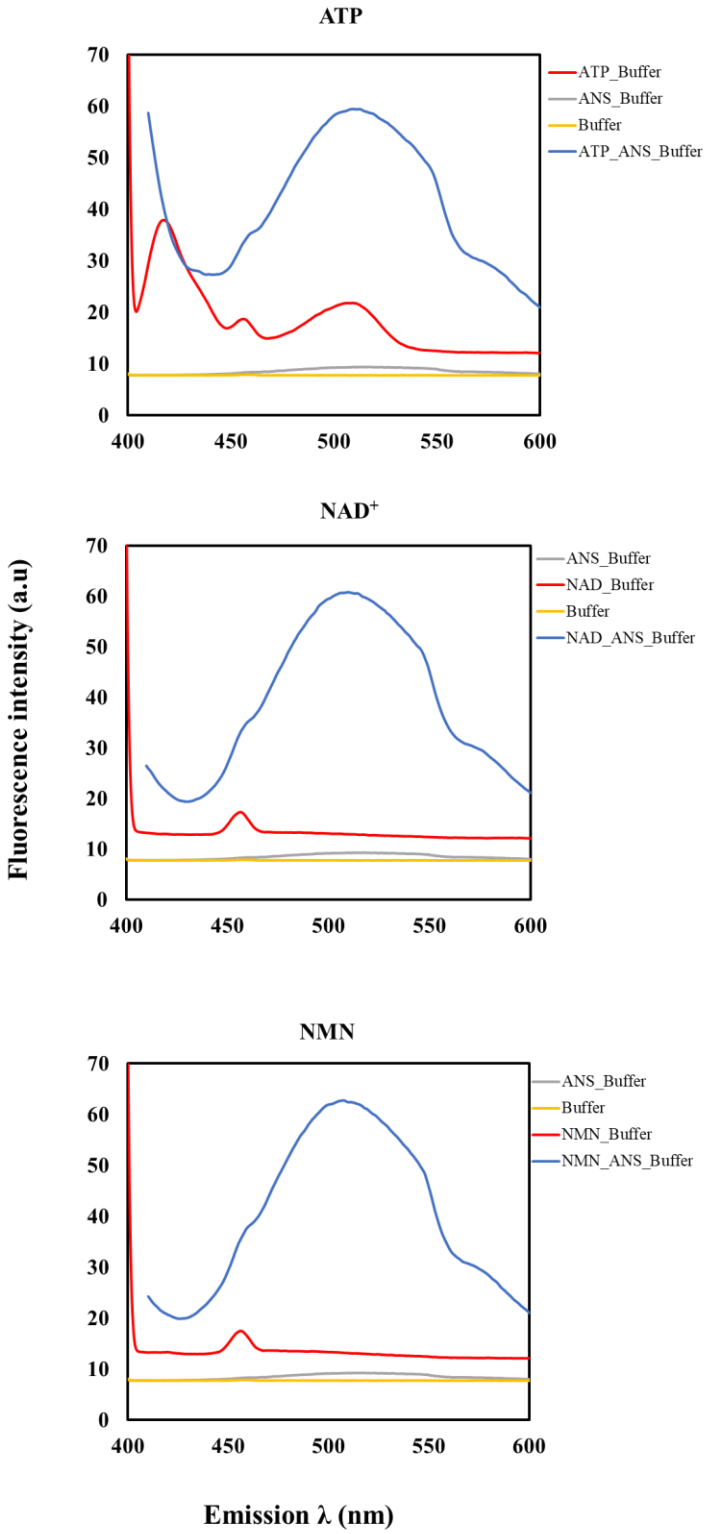

Figure S4. The fluorescence spectra showing the absorbance of the ligands (ATP, NMN and NAD^{+}) in the presence and absence of ANS.

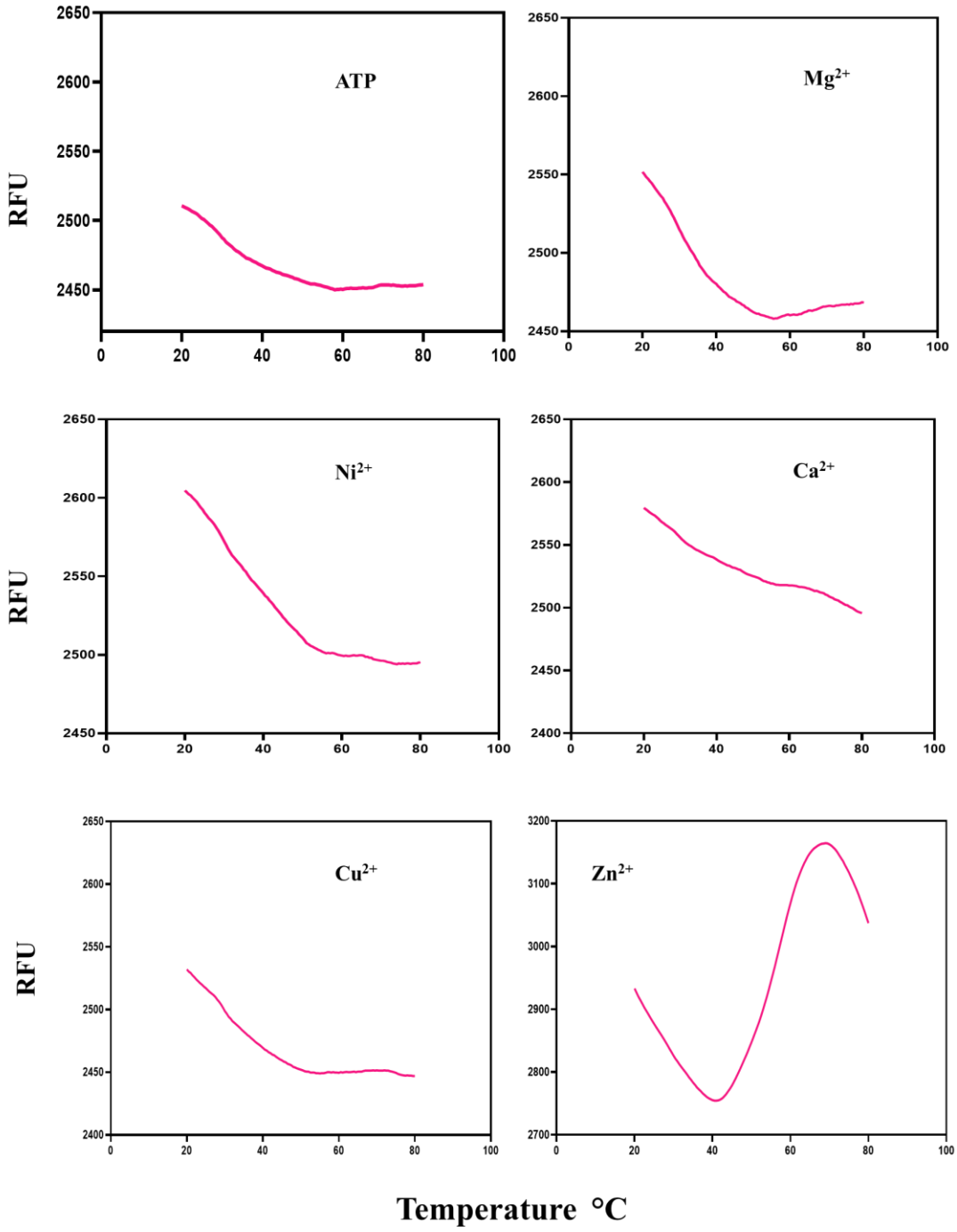

Figure S5. Melting curve for ATP and the various divalent cations in buffer.

Figure S6. Model template alignment of *Ef*NaMNAT (Model_01 : A and B) and *Bacillus anthracis* (*Ba*NaMNAT) (2qtn.1.A) as derived from Swissmodel.expasy.org. The model template obtained for *Ef*NaMNAT is short of 22 amino acids from the N-terminal, hence unreliable and may not provide a good interpretation of the protein. The highly conserved T/HXGH sequence motif is indicated in the red box. For *Ef*NaMNAT the glycine amino acid residue is replaced with alanine.

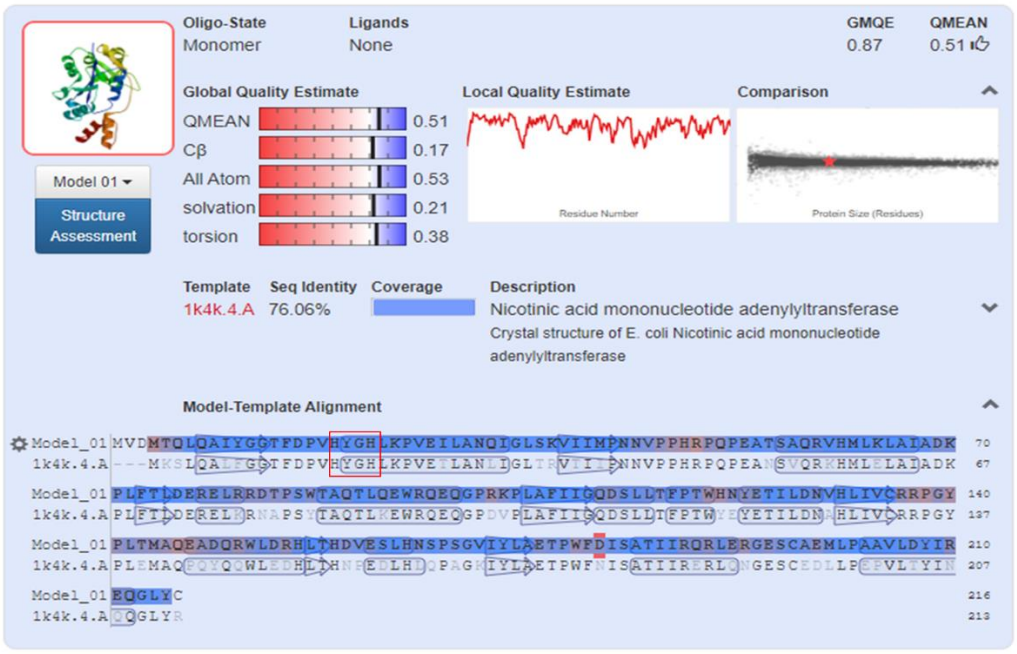

Figure S7. Structural assessment of predicted *Kp*NaMNAT model in comparison to the crystal structure of *Ec*NaMNAT as derived by Swissmodel.expasy.org. This figure shows the shared sequence identity, the GMQE (Global Model Quality Estimation), the QMEAN (Qualitative Model Energy Analysis) as well as the template alignment between both structures. The highly conserved sequence motif is indicated in the red box. *Kp*NaMNAT sequence is represented as Model_01 while *Ec*NaMNAT sequence is represented as 1k4k4.A.